NASA/CR—2015–218208

ECLSS Sustaining Metal Materials Compatibility Final Report, Electrochemical and Crevice Corrosion Test Results

R.E. Lee
Jacobs ESSSA Group, Huntsville, Alabama

Prepared for Marshall Space Flight Center
under Contract NNM12AA41C

April 2015

The NASA STI Program…in Profile

Since its founding, NASA has been dedicated to the advancement of aeronautics and space science. The NASA Scientific and Technical Information (STI) Program Office plays a key part in helping NASA maintain this important role.

The NASA STI Program Office is operated by Langley Research Center, the lead center for NASA's scientific and technical information. The NASA STI Program Office provides access to the NASA STI Database, the largest collection of aeronautical and space science STI in the world. The Program Office is also NASA's institutional mechanism for disseminating the results of its research and development activities. These results are published by NASA in the NASA STI Report Series, which includes the following report types:

- TECHNICAL PUBLICATION. Reports of completed research or a major significant phase of research that present the results of NASA programs and include extensive data or theoretical analysis. Includes compilations of significant scientific and technical data and information deemed to be of continuing reference value. NASA's counterpart of peer-reviewed formal professional papers but has less stringent limitations on manuscript length and extent of graphic presentations.

- TECHNICAL MEMORANDUM. Scientific and technical findings that are preliminary or of specialized interest, e.g., quick release reports, working papers, and bibliographies that contain minimal annotation. Does not contain extensive analysis.

- CONTRACTOR REPORT. Scientific and technical findings by NASA-sponsored contractors and grantees.

- CONFERENCE PUBLICATION. Collected papers from scientific and technical conferences, symposia, seminars, or other meetings sponsored or cosponsored by NASA.

- SPECIAL PUBLICATION. Scientific, technical, or historical information from NASA programs, projects, and mission, often concerned with subjects having substantial public interest.

- TECHNICAL TRANSLATION. English-language translations of foreign scientific and technical material pertinent to NASA's mission.

Specialized services that complement the STI Program Office's diverse offerings include creating custom thesauri, building customized databases, organizing and publishing research results…even providing videos.

For more information about the NASA STI Program Office, see the following:

- Access the NASA STI program home page at <http://www.sti.nasa.gov>

- E-mail your question via the Internet to <help@sti.nasa.gov>

- Phone the NASA STI Help Desk at 757–864–9658

- Write to:
  NASA STI Information Desk
  Mail Stop 148
  NASA Langley Research Center
  Hampton, VA 23681–2199, USA

NASA/CR—2015–218208

ECLSS Sustaining Metal Materials Compatibility Final Report, Electrochemical and Crevice Corrosion Test Results

R.E. Lee
Jacobs ESSSA Group, Huntsville, Alabama

Prepared for Marshall Space Flight Center
under Contract NNM12AA41C
and sponsored by
Jacobs ESSSA Group
managed at Marshall Space Flight Center

National Aeronautics and
Space Administration

Marshall Space Flight Center • Huntsville, Alabama 35812

April 2015

TRADEMARKS

Trade names and trademarks are used in this report for identification only. This usage does not constitute an official endorsement, either expressed or implied, by the National Aeronautics and Space Administration.

Available from:

NASA STI Information Desk
Mail Stop 148
NASA Langley Research Center
Hampton, VA 23681–2199, USA
757–864–9658

This report is also available in electronic form at
<http://www.sti.nasa.gov>

EXECUTIVE SUMMARY

Electrochemical test results are presented for six noble metals evaluated in two acidic test solutions which are representative of waste liquids processed in the Environmental Control and Life Support System (ECLSS) aboard the International Space Station (ISS). The two test solutions consisted of fresh waste liquid which had been modified with a proposed or alternate pretreatment formulation and its associated brine concentrate. The six test metals included three titanium grades, (Commercially Pure, 6Al-4V alloy and 6Al-4V Low Interstitial alloy), two nickel-chromium alloys (Inconel® 625 and Hastelloy® C276), and one high tier stainless steel (Cronidur® 30).

Samples of each metal candidate were subjected to potentiodynamic polarization testing which included open circuit potential, linear/Tafel and cyclic polarization as well as galvanic coupling pairs in which each metal was individually evaluated in the presence of another metal under open circuit conditions. Cyclic polarization is considered to be an accelerated and aggressive test procedure. For susceptible metals, the procedure is intended to promote electrical and sometimes sturctural breakdown of the passive oxide followed by pitting corrosion. However, oxide failure and pitting are not necessarily characteristic of noble metals under study.

In a concurrent test series, samples were evaluated for local and general corrosion effects utilizing angled wedge and parallel plate assemblies which were stored in the two solutions for 6 month and 12 month periods and then closely examined for signs of corrosion. These configurations were intended to reveal possible tendencies for pitting corrosion, crevicing, general corrosion or any unusual anomalies. Overall, the primary objectives of this task were to access the compatibility properties between the six metals after extended exposure and to explore latent pitting weaknesses that might exist. These six metals are already well known to be highly corrosion-resistant materials as they rank at the top of most galvanic series. Results from this study have demonstrated the superior nobility and performance of these metals under moderately aggressive conditions as well as their compatibility with each other in a mixed system of either solution.

It should be noted that during cyclic polarization test runs in brine solution, some of the Cronidur samples showed signs of pitting into the base metal. However, the tendency for pitting was not corroborated by the storage sample results which exhibited no damage. Pitting was most pronounced on Cronidur samples evaluated in brine solution and special samples subjected to extreme or abnormal testing conditions. Also under extreme test conditions, some of the Inconel and Hastelloy samples underwent general etching into the base metal. This phenomena is believed to be due to accelerated phase separation of the nickel oxide fraction in the composite passive layer as a result of the combined forces from cathodic stripping, anodic passivation under reverse bias conditions and specific factors associated with the semiconductive nature of these high nickel oxides. None of the Titanium metals indicated any signs of pitting, crevicing or general corrosion in either solution, even under extreme test conditions. Compared to the other metals, the three Titanium candidates appeared to be superior in all respects in both solutions.

Finally, several unique estimation tools and deterministic techniques are introduced to facilitate the characterization of general and pitting corrosion events, anomalous processes, electrochemical factors, pitting susceptibilities, metal penetration rates and passivation protection mechanisms associated with the six metals in the two test solutions. Special methods were empirically developed and applied for estimating equivalent reaction weights, composite oxide growth factors, long term pitting rates and penetration depths under worst case conditions, as well as relative susceptibilities for pitting initiation, pitting sustainment and general corrosion. A possible mechanism for the anomalous etching of high nickel alloys under extreme test conditions is outlined.

TABLE OF CONTENTS

LIST OF FIGURES

LIST OF FIGURES (Continued)

LIST OF FIGURES (Continued)

LIST OF TABLES

CONTRACTOR REPORT

ECLSS SUSTAINING METAL MATERIALS COMPATIBILITY FINAL REPORT, ELECTROCHEMICAL AND CREVICE CORROSION TEST RESULTS

1.0 Introduction

1.1 Project Background

One of the functions of the Environmental Control and Life Support System (ECLSS) aboard the International Space Station (ISS) is to provide potable water for the crew by subjecting human waste liquids through an elaborate recovery process. The water extraction process begins when raw liquids are 'pretreated' with a special acidified stabilizer formula, which ultimately leads to the recovery of about 70% of the water. Concentrated brine is also generated during the process and must eventually be discarded. Recently, current on-orbit pre-treat solution is suspected of leading to the formation of calcium precipitates which clog the processing filters and are responsible for reduced water recovery efficiency. It has been indicated that these precipitates are produced as a result of side reactions associated with the sulfuric acid component in the existing pre-treat formula. To address this issue, an alternative pretreat formulation has been proposed. The proposed (or alternate) pretreat stabilizer is expected to raise the overall liquid processing efficiency to 85% while the sulfuric acid component is replaced with phosphoric acid. It has been reported that the alternate pretreat formula contains about 1 ppm CrO_4^{2-} and 20 ppm $H_2PO_4^{1-}$, while the brine test solution contains about 5 ppm CrO_4^{2-} and 130 ppm $H_2PO_4^{1-}$. Test quantities of the freshly pretreated solution and its associated brine concentrate were generated at MSFC.

1.2 Material Properties

The purpose of this compatibility study is to evaluate possible corrosive effects associated with the alternate pretreat and brine solutions when they are in prolonged contact with the six metals under study here. These six metals are currently employed for components in the ECLSS urine processing assembly (UPA) and are immersed in the pretreated liquid and its associated brine on a continuous basis. Characteristics of the six metals are given in Table 1 as provided by the respective vendors.

Table 1: Compositions of the six metals and alloys under investigation for the current study.

Inconel 625		Hastelloy C276		Titanium, CP		Titanium 6Al-4V		Titanium 6Al-4V LI		Cronidur 30	
	Raw Wt%		Raw Wt%		Raw Wt%		Raw Wt%		Raw Wt%		Raw Wt%
Ni	60.3%	Ni	58.9%	Ti	99.5%	Ti	88.4%	Ti	88.5%	Fe	81.8%
Cr	22.3%	Cr	16.1%	O	0.34%	Al	6.26%	Al	6.1%	Cr	15.3%
Mo	9.26%	Mo	15.3%	Fe	0.17%	V	3.95%	V	4.0%	Mo	0.97%
Fe	3.72%	Fe	5.59%			Mo	0.01%	N	0.0102%	Si	0.63%
Nb	3.50%	W	3.39%			N	0.01%	Cr	0.010%	N	0.38%
Co	0.14%							Mo	0.0010%		
Mn	0.13%										
Density 8.44 g/cc		Density 8.89 g/cc		Density 4.51 g/cc		Density 4.42 g/cc		Density 4.42 g/cc		Density 7.70 g/cc	

It is noteworthy to realize that all six metal candidates are located at the top of most published Galvanic Tables, including the Galvanic Series in Seawater published in MIL-STD-889. Such noble attributes were undoubtedly taken into consideration during the original materials selection process for ECLSS. All six candidates are well documented to be highly resistant to general and pitting corrosion without the requirement for additional surface protection measures because each of these metals spontaneously forms a tenacious, self-repairing, 1-5 nm thick passive oxide layer on its surface which remarkably protects the base metal from corrosive environments. These layers form and repair themselves so rapidly that a momentary breach in the oxide (abrasion, scratch or chemical attack), while the metal is in a corrosive environment, poses minimal risk to sustained surface corrosion events.

As a result of their corrosive, thermal and mechanical properties, materials in the Ni-Cr-based Inconel and Hastelloy families are frequently regarded as 'superalloys'. Also, because of their apparent similarity in composition and properties, Inconel 625 and Hastelloy C276 are sometimes indicated as members in the same general family, being identified simply as Alloy 625 and Alloy C276. On the other hand, as the historical evidence and the results of this study demonstrate, the surfaces of titanium and its alloys produce the most protective oxide layers of all. This is well recognized within the industry as titania deposition technologies are highly sought after for the development of superior corrosion protection approaches on other metals, even without the self-repairing capability that is normally present on passive Ti substrates. As a result of the high chromium content, Cronidur might could be envisioned as a 'super stainless steel' with properties that rival A286 and AM350 alloys. It is believed that the exceptional corrosion properties exhibited by Ni-Cr and Fe-Cr alloys is not only due to the highly protective nature of the Cr-rich oxide layers that form, but also on the formation of chromites within the outer oxide layers which appear to provide elevated levels of corrosion resistance. There is growing evidence that iron chromite ($FeCr_2O_4$) and particularly nickel chromite ($NiCr_2O_4$) impart some unusually astute corrosion inhibitive effects within the protective oxide layers of these types of alloys.

It is also interesting to note that the well-known nobilities of precious metals such as silver (Ag), gold (Au) and platinum (Pt) are a result of their high oxidation potentials since these metals do not readily oxidize or rely on passive oxide surface layers for corrosion protection. Indeed, all six metals in this study derive their superior corrosion protective properties exclusively from the surface passivation layer that forms during the first few seconds after the metal is exposed to ambient air or other corrosive (anodic) environments. In general, the net level of corrosion protection afforded by any passivating metal is wholly dependent on (a) the tenacity of the oxide layer and (b) how rapidly the oxide structure repairs itself when breached. That is, the mechanical properties of the oxide minimize the likelihood that a breaching event will expose the base metal while a rapid regeneration process ensures that, in the event of a breach, exposure of the base metal is kept to a minimum.

In unpassivated form, the corrosive activities of exposed titanium and its alloys are about the same as the aluminum alloys. However, in their passivated states, it is clear that substantial differences exist between the respective titania and alumina layers that passivate each of their surfaces. All of the passivated Titanium metals are near the top of the Galvanic Series as they are very cathodic and well protected, while passivated Aluminum alloys are closer to the bottom since they are highly anodic and much more susceptible. Titania layers are very strong and repair themselves rapidly while alumina layers are frail with moderate self-healing properties. In their natural passivated states, all six metals evaluated in this task are comparable in nobility and corrosive resistance to that of Gold and Silver. In essence, the work done in this study supports the orthodox conclusions that are already well established

regarding the corrosive nobilities of these six metals, but it goes a step further by substantiating these attributes in the particularly aggressive ECLSS solutions of interest.

1.3 Polarization Testing

Whenever the potential (voltage) and electric current (amperage) are measured and evaluated together, the potential is indicative of the metal's nobility with respect to the tendency, probability or susceptibility for corrosion to occur, while the current is directly proportional to the rates of corrosion, reduction and oxidation. For passivating metals, rates are typically converted into units that indicate how fast the metal thickness is recessing or etching as it is consumed to form passive metal oxide product on the surface and how fast the thickness of the oxide is growing in its place. Base metal recession and passivation are mutually inclusive processes since one cannot occur without the other. To help clarify the relationship between measured potential and current, consider, for example, that a high breakdown potential associated with a given metal infers high nobility and low susceptibility to corrosion, while a large pitting current implies a high pitting rate. A low corrosion potential implies high susceptibility to corrosion while a high repassivation current corresponds to a rapid passive oxide restoration process which is characteristic of a robust corrosion protection mechanism.

2.0 Experimental

2.1 Test Sample Preparation

2.1.1 Machining and Finishing of Test Samples

All test samples were machined from bulk metal stock into approximately 3’ X 3” X 1/2” plates. This size was deemed appropriate for all of the polarization, galvanic and crevice corrosion testing as mandated by the ECLSS project to satisfy the requirements for evaluating the performance and compatibility of each metal candidate of interest. All the metal samples were (a) thoroughly degreased rinsed and dried, (b) their surfaces were dry-sanded to maintain at least 400 grit and then they were (c) liberally rinsed with DI water, solvent rinsed and air dried in ambient atmosphere (68-72°F and 30-40% R.H.) to promote natural development of their native surface oxide layers prior to testing. Overall, several hundred test specimens were acquired, prepared and evaluated for this study.

2.1.2 Crevice Sample Assembly Configuration

Samples for evaluating possible crevice corrosion effects were assembled in two slightly different configurations loosely based on ASTM G78[1]. Sample descriptions are given in Tables 2 and 3 as provided by the ECLSS project test proposal[2].

Angled Crevice Sample Configuration
Sandwich-type assemblies consisted of two sample plates clamped together and separated by a small rectangular-shaped layer of filter paper near one side of the clamped assembly to create a tiny *angled crevice gap* between the two plates.

Parallel Crevice Sample Configuration
Sandwich-type assemblies consisted of two sample plates clamped together and separated by a larger square-shaped layer of filter paper centered in the assembly to create a tiny *parallel crevice gap* around the edges between the two plates.

Table 2: Parallel (sandwich) crevice corrosion test sample requirements.

Material	Number of 3”x3”x0.25” plate samples needed (surface finish same as hardware)	Remarks
Inconel 625	10	2 sandwiches (4 samples) for solution 1 2 sandwiches (4 samples) for solution 2 1 sandwich (2 samples) in DI water (control)
Hastelloy C276	10	2 sandwiches (4 samples) for solution 1 2 sandwiches (4 samples) for solution 2 1 sandwich (2 samples) in DI water (control)
Titanium Commercially Pure (Ti CP)	10	2 sandwiches (4 samples) for solution 1 2 sandwiches (4 samples) for solution 2 1 sandwich (2 samples) in DI water (control)
Ti 6Al-4V	10	2 sandwiches (4 samples) for solution 1 2 sandwiches (4 samples) for solution 2 1 sandwich (2 samples) in DI water (control)
extra low interstitial (ELI) Ti CP	10	2 sandwiches (4 samples) for solution 1 2 sandwiches (4 samples) for solution 2 1 sandwich (2 samples) in DI water (control)
ELI Ti 6Al-4V	10	2 sandwiches (4 samples) for solution 1 2 sandwiches (4 samples) for solution 2 1 sandwich (2 samples) in DI water (control)
Cronidur 30 (hardened, as for bearings)	10	2 sandwiches (4 samples) for solution 1 2 sandwiches (4 samples) for solution 2 1 sandwich (2 samples) in DI water (control)
Total # of sandwich corrosion samples	**70**	

Table 3: Angled (wedge) crevice corrosion test sample requirements.

Material	Number of 3”x3”x0.25” plate samples needed (surface finish same as hardware)	Remarks
Inconel 625	10	2 sandwiches (4 samples) for solution 1 2 sandwiches (4 samples) for solution 2 1 sandwich (2 samples) in DI water (control)
Hastelloy C276	10	2 sandwiches (4 samples) for solution 1 2 sandwiches (4 samples) for solution 2 1 sandwich (2 samples) in DI water (control)
Titanium Commercially Pure (Ti CP)	10	2 sandwiches (4 samples) for solution 1 2 sandwiches (4 samples) for solution 2 1 sandwich (2 samples) in DI water (control)
Ti 6Al-4V	10	2 sandwiches (4 samples) for solution 1 2 sandwiches (4 samples) for solution 2 1 sandwich (2 samples) in DI water (control)
extra low interstitial (ELI) Ti CP	10	2 sandwiches (4 samples) for solution 1 2 sandwiches (4 samples) for solution 2 1 sandwich (2 samples) in DI water (control)
ELI Ti 6Al-4V	10	2 sandwiches (4 samples) for solution 1 2 sandwiches (4 samples) for solution 2 1 sandwich (2 samples) in DI water (control)
Cronidur 30 (hardened, as for bearings)	10	2 sandwiches (4 samples) for solution 1 2 sandwiches (4 samples) for solution 2 1 sandwich (2 samples) in DI water (control)
Total # of wedge corrosion samples	**70**	

2.1.3 Sample Allocations for Polarization and Galvanic Testing

Test sample descriptions and requirements for polarization and galvanic coupling tests are given in Tables 4 and 5 as provided by the ECLSS project test proposal[2].

Table 4: Sample count requirements for polarization testing.

DC Methods	Open Circuit Potential (Corrosion Potential)	Linear Polarization	Tafel Polarization	Cyclic Polarization
Inconel 625	3/soln X 2 soln = 6 samples			6
Hastelloy C-276	6			6
Ti-CP	6			6
Ti-ELI	6			6
Cronidur 30	6			6
Total # Required	**60**			

Table 5: Sample count requirements for galvanic coupling pairs.

Galvanic Couple Potential & Current	IN625	C-276	Ti-CP	Ti-ELI	Cronidur 30
Inconel 625		6	6	6	6
Hastelloy C-276	6		6	6	6
Ti-CP	6	6		6	6
Ti-ELI	6	6	6		6
Cronidur 30	6	6	6	6	
Total # Required	**120**				

Tables 2-5 Notes:
1) Specimen size -- 2.5"(+/- 0.125") x 2.5"(+/- 0.125") x 0.5" (-0.375") -- roughly rectangular
2) 600 grit surface finish
3) 3 specimens per test sequence
4) 0.75 L solution per test specimen
5) Solutions -- Pretreat and Brine
6) Testing conducted at 100 °F

2.2 Procedures and Techniques

2.2.1 Crevice Corrosion Evaluations

Clamped test assemblies of each of the six metals were placed in storage in both the pretreat and brine solutions in two separate groups, one group to be evaluated after 6 months storage and another group to be evaluated after 12 months storage. After removal from the test solutions and thorough rinsing in DI water, each sample was subjected to visual and microscopic evaluation to check for signs of corrosion, surface growth, pitting, base metal degradation or any anomaly of relevance. While sample configurations, procedural steps and evaluations were loosely based on ASTM G78, the specific test approach utilized for this project was developed at the Materials and Processes Laboratories at Marshall Space Flight Center several years ago.

2.2.2 Polarization Equipment and Test Procedures

Electrochemical measurements were carried out utilizing four Princeton Applied Research (PAR) potentiostat/galvanostat workstations, Models 2273 and 273A running PAR's Powersuite software for data collection and analysis. Flat test cells were used throughout which included 1 cm^2 exposure holes on one end for polarization routines and 1 cm^2 exposure holes on both ends for galvanic coupling. Ag/AgCl reference electrodes were used throughout. Two of the experimental set-ups are shown in Figure 1.

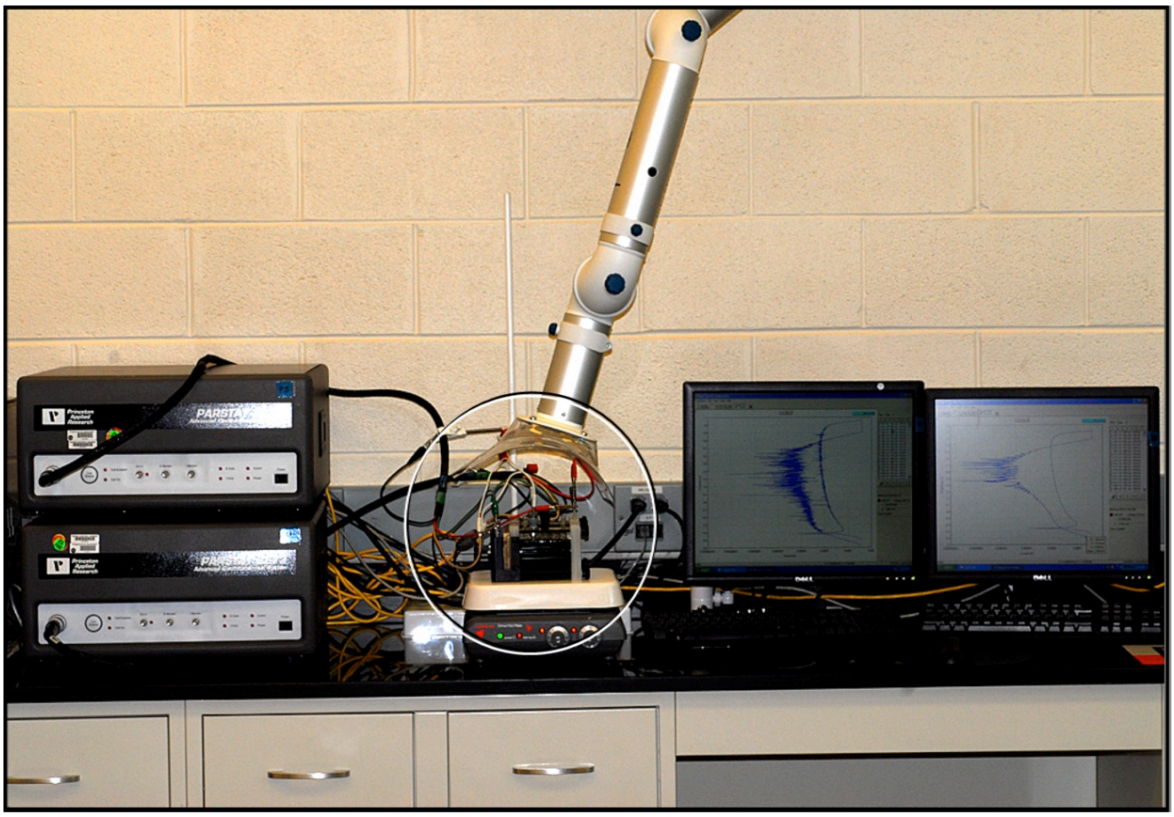

Figure 1: Photograph of two PAR workstations with two test cells (center) in operation.

The flat cell offers flexibility for a variety of DC electrochemical studies including Open Circuit, Linear, Tafel, Cyclic polarization and Galvanic Coupling measurements. For Galvanic Coupling tests, the cell is re-assembled using a second 1cm^2 sample area end-cap for the other metal so that both samples are connected across the test solution. The second metal is grounded and interacts with the first metal which is monitored for voltage and current changes.

For many researchers, their polarization test strategy includes cathodically conditioning the sample prior to or at the beginning of the test run by starting the scan at a very low potential relative to the pre-measured or perceived open circuit potential (OCP). Such treatments are intended to chemically reduce, dissolve and remove or strip the air-formed native oxide layer from the metal surface while it is immersed within the in the test solution of interest under cathodically protective conditions. This induces formation of a new passive layer on the test surface as the potential passes into the anodic portion of the scan well below the original OCP. The intent is to conduct the test on an uncontaminated, freshly formed passive layer within the specific electrolytic solution of interest. The new oxide layer is very similar to the air-formed coating . . . but it is not necessarily the same.

In contrast, one of the objectives of the current study was to evaluate the metals in their natural states after immersion into the subject test solutions as this approach better represents the actual field conditions that exist when the components are assembled, incorporated into the full-scale ECLSS system and submerged in pretreated and brine solutions. In any event, it is understood that the layers will adapt to the new environment over time (such effects are covered in Section 4). It is also realized that cathodic conditioning is not applied to the components prior to or during their normal operation environments, so such treatments were not considered to be relevant for this project. Alternatively, our test samples included final rinsing steps in solvent and DI water followed by 24 hours of ambient air drying under controlled conditions (68°-72°F, 30-40% R.H.) in order to facilitate growth of a robust natural passive layer on the surfaces prior to testing. However, a few complementary test samples were intentionally subjected to very cathodic and very anodic voltages during supplemental cyclic testing as part of the overall evaluation in order to better understand the effects of extreme polarization applications. These results are covered in Section 5.6.

2.2.3 Polarization Test Descriptions

Brief definitions of the test modules employed for this study are given below.

Open Circuit Potential (OCP) – Measures the steady state potential (voltage) E_{OC} as the test sample is exposed to the solution over time with no power applied. Can take sometimes more than 10 days to reach a stable steady state (constant oxidation rate) for the noble metals under study.

Linear Polarization – Measures the resulting current response when a very small voltage is applied (±10-20 mV) relative to OCP. This potential level is considered to be nondestructive. Provides the corrosion resistance R_{Cor} and the corrosion rate k_{Cor} in the preselected potential range.

Tafel Polarization – Measures current response across a larger potential range (±200-250 mV) relative to OCP. Spans the near cathodic and anodic regions close to E_{OC} providing the corrosion potential E_{Cor}, corrosion current I_{Cor}, the beta Tafel parameters and k_{Cor}. Some damage to the sample area may occur.

Cyclic Polarization – Applies a broad preselected potential cycle across the anodic passivation range and beyond the breakdown potential E_{Brk}. The scan is reversed at a preselected potential E_{Ver} and brought back down through the repassivation branch, all while the current is monitored. A hysteresis loop is often generated. Provides pitting corrosion and oxidation rates as well as advanced information regarding the relevant passivation protection mechanisms associated with these metals including oxide regeneration factors, repassivation rates, relative susceptibilities and protection capabilities. Additional supportive general corrosion information may also be obtained from cyclic polarization data.

Note: For clarity, it should be realized that the crystal structures comprising the passive oxides on these metals are not always damaged catastrophically at E_{Brk}, but rather their insulator properties undergo a rapid transformation as electrical resistance suddenly drops off and conduction greatly increases across the layer allowing external corrosive agents to interact directly with the metal surface, possibly leading to pit initiation. This is due to the rapid increase in the mobility of charge carriers near E_{Brk}. As the voltage is further increased, tunneling of the electrons may occur and then at some point beyond E_{Brk}, the oxide structures may physically fail and start dissolving in the test solution.

Galvanic Coupling – Measures the steady state potential (voltage) E_{OCG} and current I_g as two different metals interact (galvanically) across the test solution with no power applied. Can sometimes take more than 10 days to reach a stabilized steady state for the noble metals under study.

2.2.4 Polarization Test Sequence

Each metal candidate was subjected to the test sequence depicted in Figure 2 below. Depending on time allocations and schedule flexibility, a minimum of 4 and up 8 separate test sample areas were evaluated for each candidate metal in order to obtain respectable averages and to test the extremes.

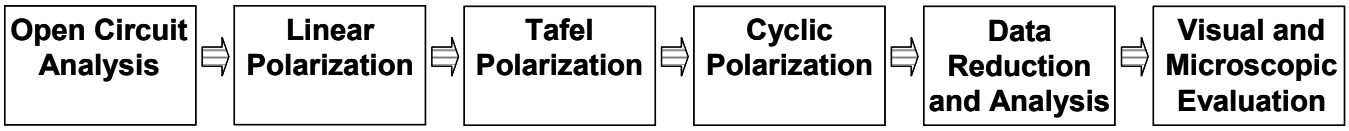

Figure 2: Incremental flow sequence for polarization testing.

2.2.5 Test Equipment and Software Limitations

It was observed that PAR's Powersuite software permits advanced evaluations and data correlations for Open Circuit Potential (OCP), Tafel analysis and Cyclic Polarization that the Gamry Instrument Software Suite and VersaStudio seem to omit. Some of these limitations included unbalanced current measurements during OCP runs, multiple linear fits on a single graph, data conversion and transfer, and Tafel-like analysis of the repassivation region. The ability to plot and manipulate voltage, current, charge and time on any axis in any test is a great asset and allows the user to decide which parameters are best suited for their situation rather than a one-size-fits-all analytical approach predetermined by the software designer. Indeed, these older capabilities were responsible for the quality and depth of analysis which were made possible during this study. It is hoped that future software platforms will emphasize functional tools like these rather than the over-automated, user-limited interfaces supplied in the recent versions.

3.0 Summary of Test Results

3.1 Crevice Corrosion Assessment

Assemblies of each of the six metals were placed in storage in both the pretreat and brine solutions for 6 months and 12 months. After each period, they were removed and visually inspected. Six month test results were presented at the Mid-Term Briefing and indicated no corrosion issues. Results of the twelve month samples were almost identical to the six month group with no anomalies apparent on any metal sample in either solution. Images of one side of the pretreat and brine crevice wedge and sandwich assemblies are given in Figures 3 and 4. Both faces in each assembly were essentially identical.

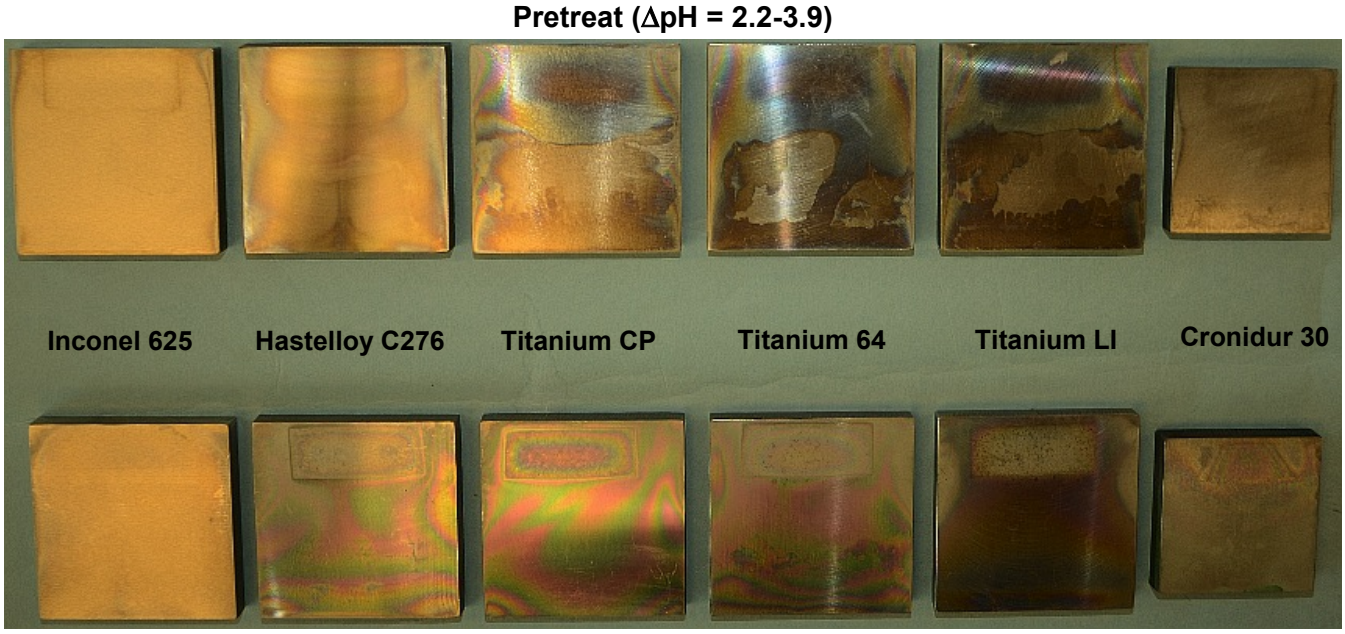

Figure 3: Image of the wedge configuration test samples after one year storage.

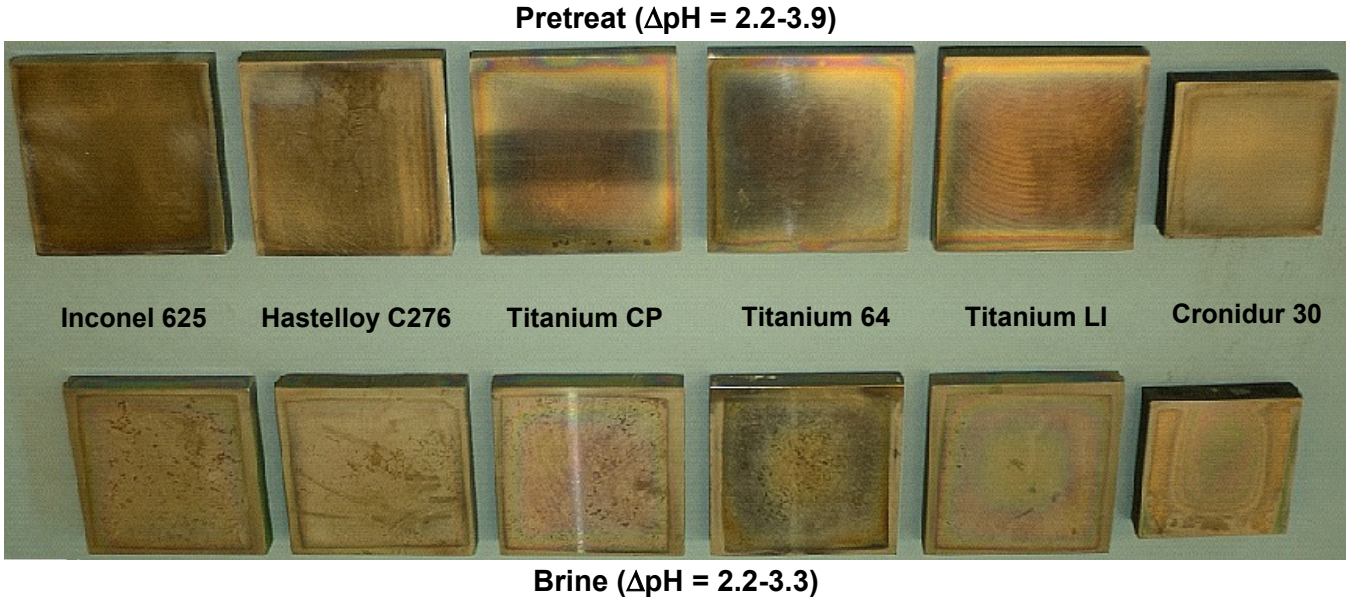

Figure 4: Image of the sandwich configuration test samples after one year storage.

In all cases, microscopic examination indicated no visible signs of pitting, etching, recession or surface growth on any of the six metals in either of the two test solutions. However, some of the samples developed translucent surface discolorations in the oxide layer after rinsing with pH 7 DI water. All indications are these patterns are purely optical in nature due to small lattice plane changes in the oxide layers as they adapt to ambient conditions. There was no evidence or indications suggesting that these visual irregularities had any effect on the corrosion protection properties of the metals. Photographic close-ups of some of these surface aberrations are given in Figure 5.

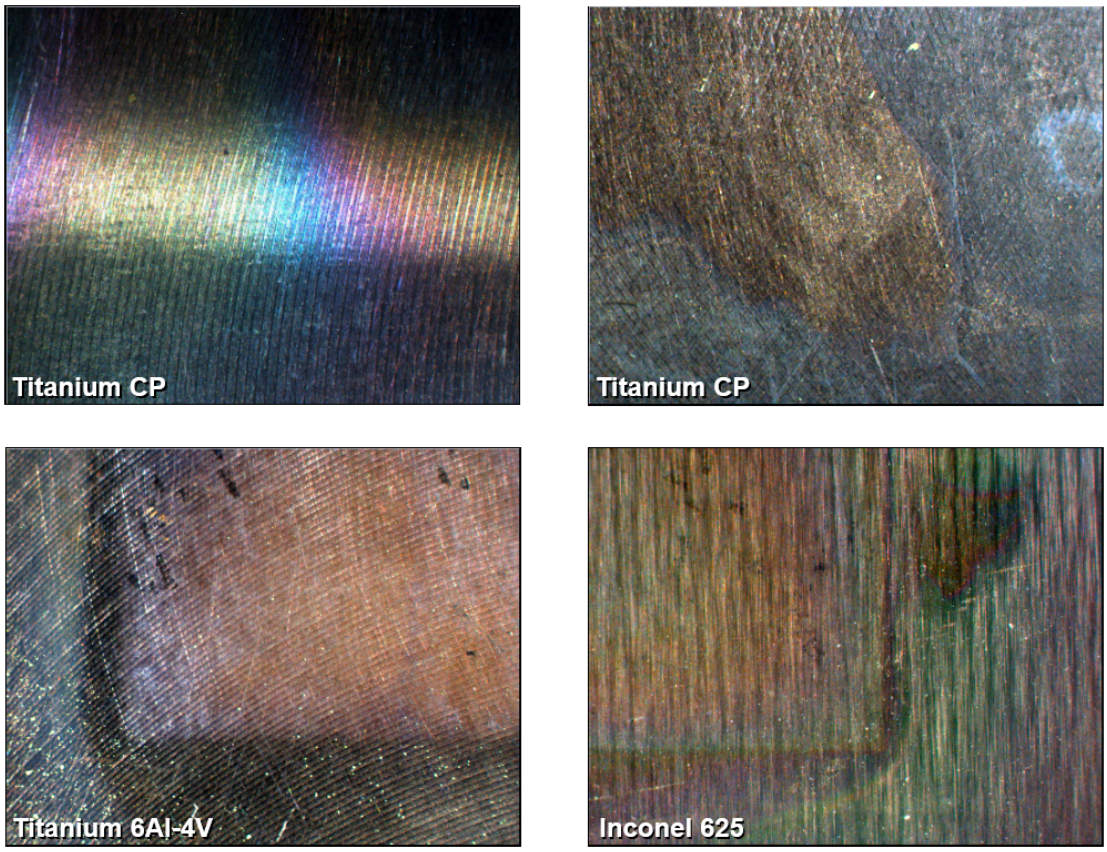

Figure 5: Close-up images of discolorations on the six month exposure crevice samples.

During the first 6 month period, the pH of the pretreat solution changed from about 2.2 to about 3.0 and that of the brine changed from about 2.2 to 2.8. After one year in storage, final pH values of the test solutions were about 3.9 and 3.3 respectively. There were no visible differences between the samples stored for 6 months and those stored for 1 year. Both groups exhibited the same degree of superficial coloration patterns. Not all of the exposed areas reflected such patterns but most of the titanium-based metals seemed to exhibit these effects to some degree or another. In conclusion, this test has shown that all of the candidates are protected from the effects of general, local and galvanic corrosion in both test solutions for at least one year under slightly heated, stagnant, nonaggressive exposure conditions. Based on these results, one could presume that all six metals are protected well beyond one year.

3.2 Potentiodynamic Polarization Testing

Several published works s and guidelines were utilized for enhancing the understanding of basic corrosion concepts, polarization principles, test methodologies, cell configurations, data analysis and data interpretation throughout the testing and evaluation phase of this effort[3, 4, 5, 6, 7]. It is noteworthy to add that some of the analysis and evaluations were supplemented with new, improved or original approaches which were developed specifically for this study and are introduced later in the report.

3.2.1 General Corrosion Effects

In contrast to localized forms of corrosion such as pitting, general corrosion involves larger areas or 'acreage' of the base metal which interacts via oxidation with the environment. A classic example is the rusting of iron alloys. Industrial use of the term 'Corrosion Rate' refers to the rate of etching or recession into the base metal as a result of corrosive oxidation reactions which consume the metal, leading to the formation of metal oxide and hydroxide precipitates on the surface. For corroding metals, such as the low alloy steels, these products are frail and unorganized as they will easily spall, erode or wash away relatively quickly. They provide no corrosion protection to the base metal. However, for strongly passivating metals, such as the ones under study here, the oxidation products rapidly evolve into structurally organized, semi-crystalline oxide layers which provide an astounding level of protection against degradative oxidation. In these cases, the very thin layer of metal volume removed during recession becomes occupied with protective oxide, preventing further exposure of the metal surface. With this understanding, the terms 'corrosion rate' and 'recession rate' may sometimes be used interchangeably.

Thus, the six noble metals under study here did not generally undergo destructive corrosion, but the base metal did recede inward while protective oxide growth filled the etched volume and preempted sustained corrosion reactions with the metal. In short, recession rates for these metals are due to growth of the protective oxide layer rather than corrosive degradation of the base metal. All six metals were very corrosion-resistant in both of the solutions evaluated, as they are expected to be in most other solutions throughout industry and nature (except hot concentrated mineral acids and fluoride solutions). In terms of their low recession rates, all six metals appear to be at least one order of magnitude higher than the 'Outstanding' rating for general corrosion which is the noblest rating recognized in the industry. The Inconel, Hastelloy and Cronidur samples exhibited nobilities very close that of Titanium in accordance with publish Galvanic Series in seawater as mentioned earlier. Indeed, the corrosion-resistance properties for all six metals were comparable to that of Silver. Titanium and its alloys appeared to exhibit slightly higher recession rates than the Inconel, Hastelloy and Cronidur samples, but the oxide layers that formed on the Titanium samples were rapid and more tenacious than those on the other metals. It is well known that unprotected Titanium is about as galvanically active as unprotected aluminum, but its protective oxide is also well established as one of the most corrosion-resistant oxide layers known. All three Titanium samples appeared to be more resistant to general corrosive effects than any of the other metals.

3.2.2 Pitting Corrosion Effects

Contamination sites within the oxide structure, surface traces of fluoride ions, localized physical breaches of the oxide layer or some other local force that weakens the oxide crystal lattice can lead to the initiation of corrosion pits into the base metal. The self-repairing, repassivation mechanisms for the six metals under study typically precludes sustained pit growth. Open circuit data plots for a couple of the Cronidur samples in the brine solution indicated possible signs of pitting activity, but these transients could have been generated by pit initiations into the oxide layers that never actually made it into the base metal. None of the other metals showed any such anomalies during open circuit testing.

Cyclic polarization is an accelerated test that generally imparts some degree of damage to the exposed area as it is subjected to increasing anodic voltages not normally seen in the field. Results from the cyclic test runs followed by visual and microscopic examination of the exposed areas revealed that most of the Cronidur samples exhibited signs of pitting and crevicing (along the O-ring) in both solutions with pitting/crevicing effects most pronounce in the brine samples. Cyclic polarization data analysis also reflected these observations. In addition, several of the Inconel and Hastelloy samples subjected to cathodic conditioning at the beginning of the test exhibited general recession into the base metal with the formation of a green nickel oxide/hydroxide precipitate on the surface after rinsing in DI water (pH ~7) when tested in the pretreat solution. None of the Titanium candidates indicated any signs of surface degradation but did show superficial discolorations in the oxide layer similar to that noted earlier on the crevice sandwich/wedge samples. Figures 6 and 7 provide representative images of the exposed 1cm^2 circular test areas for the six metals in pretreat and brine solutions respectively.

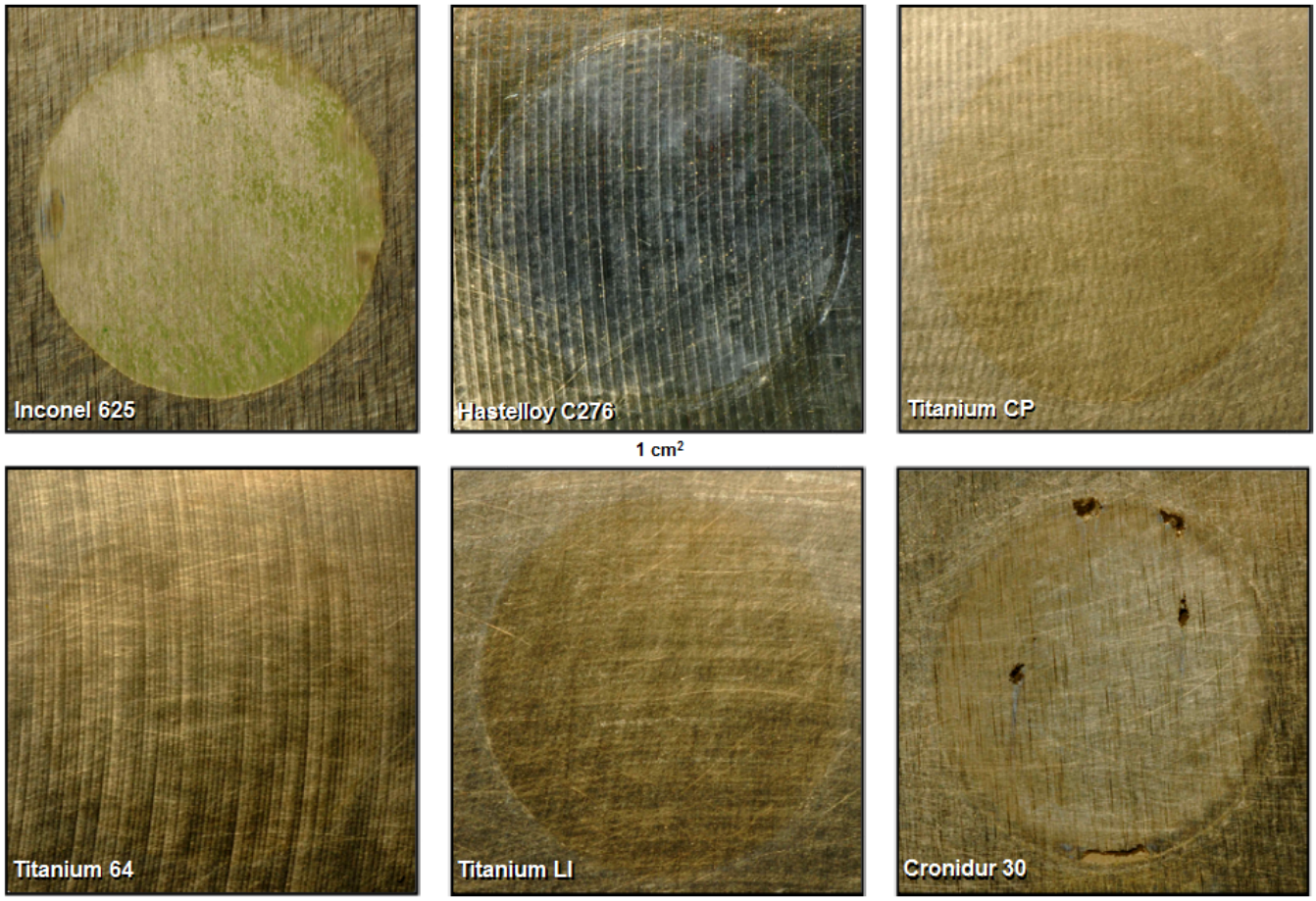

Figure 6: Photographs of some of the test areas for the six metals after cyclic polarization in pretreat solution.

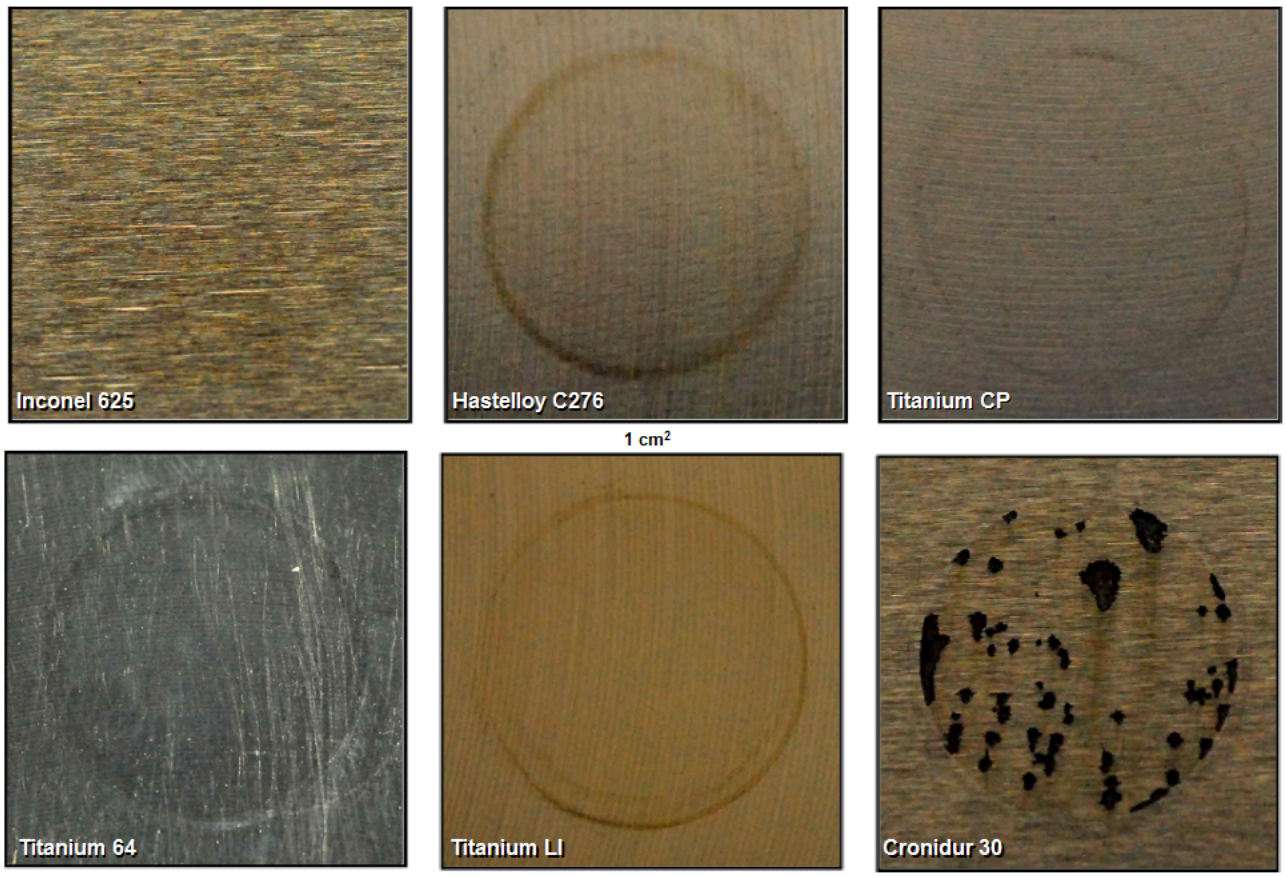

Figure 7: Photographs of some of the test areas for the six metals after cyclic polarization in brine solution.

3.2.3 Summary of Polarization Test Results

Open Circuit Potential (OCP), Linear and Tafel polarization test results are focused primarily on general corrosion effects while cyclic polarization provides information that pertains to pitting and localized corrosion events. In terms of general corrosion, relative nobility, low susceptibility and low recession rate, an overall average ranking or grouping of the six metals could be suggested: Titanium CP, Titanium LI, Titanium 64 > Cronidur 30, Inconel 625, Hastelloy C276.

With regard to general corrosion rate activity in situations reflective of steady state conditions, the pretreat solution sometimes appeared to be more active than the brine solution. During cyclic polarization and pitting analysis, the situation almost seems to be reversed since overall average pitting recession and repassivation rates in the brine solution were typically higher than those in the pretreat solution for all six metals. This is likely related to the concentrated levels of chloride ion in the brine solution. Analysis indicated that Cronidur 30 had a substantially higher susceptibility for pit initiation and sustained growth than any of the other metals. On the average, an overall ranking of the candidates could be suggested from high pitting susceptibility under polarized conditions: Cronidur 30 >> Hastelloy C276, Inconel 625 > Titanium 64, Titanium LI, Titanium CP.

Disregarding the superficial of surface discolorations shown earlier, all of the Titanium candidates appeared to be almost immune to the effects of general corrosion, pitting, crevicing, and aggressive conditions utilizing voltages that were extremely anodic and cathodically reductive. While likely irrelevant to most field situations, high nickel alloys such as Inconel and Hastelloy may exhibit negative side effects when very cathodic starting points are applied prior to anodic polarization resulting in abnormal base metal recession. This phenomena is covered in greater detail in Section 5.6. It should be noted that all of the preceding results pertain to individual samples isolated from other materials. They are not necessarily reflective of mixed systems subject to possible galvanic interactions.

Since the quantity of data collected and evaluated for this study is rather extensive, it cannot be presented here in its entirety. However, Table 6 contains averages of some of the more important parameters evaluated in this effort. More extensive data tables, analysis and detailed discussions pertaining to these results are presented in Section 4.0.

Table 6: Selected averages from Open Circuit, Linear, Tafel and Cyclic test evaluations.

	Open Circuit Data and Linear/Tafel Polarization							Cyclic Polarization		
	Open Circuit Potential	Steady State Time	Relative Corrosion Susceptibility	Steady State Metal Recession Rate		Steady State Oxide Growth Rate		Net Pitting Rate	Susceptibility for Pitting Initiation	Susceptibility for Pitting Sustainment
PreTreat	(mVAgCl)	(hours)	(%)	(Å/day)	(mil/year)	(Å/day)	(mil/year)	(mil/year)	(%)	(%)
Titanium CP	93.9	12	0.30%	116.7	0.168	303.9	0.437	0.00	0.62%	0.37%
Titanium 6-4 LI	80.8	12	0.34%	94.0	0.135	270.6	0.389	0.00	0.75%	0.38%
Titanium 6Al-4V	77.4	15	0.34%	100.7	0.145	290.4	0.417	0.00	0.79%	0.38%
Cronidur 30	39.0	33	4.53%	63.2	0.091	319.7	0.459	3.77	15.9%	11.34%
Inconel 625	23.4	21	2.92%	74.9	0.108	394.8	0.567	0.00	9.02%	1.58%
Hastelloy C-276	18.7	28	3.63%	67.8	0.097	345.2	0.496	0.00	10.4%	0.76%
Brine										
Titanium CP	104.3	13	0.30%	89.2	0.128	232.3	0.334	0.00	0.74%	0.40%
Titanium 6-4 LI	97.0	13	0.34%	78.5	0.113	226.0	0.325	0.00	0.84%	1.03%
Titanium 6Al-4V	95.2	14	0.34%	69.3	0.100	200.0	0.287	0.00	0.74%	0.70%
Cronidur 30	46.5	37	4.52%	40.0	0.058	202.6	0.291	10.9	19.8%	8.53%
Inconel 625	38.2	25	2.91%	41.1	0.059	216.3	0.311	0.00	8.94%	0.43%
Hastelloy C-276	32.3	26	3.61%	48.6	0.070	247.7	0.356	0.00	10.5%	0.58%

As indicated by the numbers, nobility rankings do not always correspond precisely with susceptibilities or estimated recession/oxidation rates pertaining to general and pitting corrosion, at least not in the solutions under evaluation. Due to the compositional complexity of the test mixtures and the highly alloyed metals evaluated, a number of unidentified electrochemical factors are likely involved which ultimately play a role in the observed averages.

As inferred by Open Circuit Potential values, apparent nobilities for the titanium-based metals appeared to be better than the other three metals. This is corroborated by estimates for Relative Corrosion Susceptibility which indicated that Titanium and its alloys are markedly superior to the other metals, but this difference is not as large is it may seem (special methods for estimating susceptibilities are covered in Section 5.4). While some of the numerical differences in Table 6 may appear substantial, compared to all the other materials in most Galvanic Series rankings, they are relatively small as these six metals are actually quite similar to each other in terms of nobility and corrosion resistance. Approximate time periods to reach 85-90% of the steady state plateau indicates that Titanium metals tend to stabilize a little quicker than the other metals. Maximum pitting rates (recession into the base metal) were all zero except for Cronidur. For this study, original estimation techniques were developed to better characterize compositional changes and growth parameters of the composite oxide phases that develop on each metal in the subject test solutions (see Section 5.2). Each alloy is considered to produce a unique composite metal oxide phase. Part of the intent was to ascertain that the attributes derived for each oxide phase were specific to each corresponding metal precursor and not just a general approach or crude procedure applied to all metals. Indeed, this concept extends the theory given in ASTM G102.

3.3 Galvanic Coupling Measurements and Summary

A minimum of three tests were conducted using each metal as the working electrode against each of the other metals in the series. In all, several hundred tests were conducted to fulfill the scheduled galvanic coupling test requirements. A reduced summary of those results is given in Table 7.

Table 7: Reduced summary of averages indicating overall compatibility factors for the six metals.

PreTreat	Total Increase in Potential Over OCP (mV_{AgCl})	Total Increase in Susceptibility Over OCP (%)	Total Increase in Recession Rate Over OCP (Å/day)	Total Change in Oxide Growth Rate Relative to OCP (Å/day)	Total Change in Steady State Time Relative to OCP (hours)
Titanium CP	-123.5	0.004%	0.87	-23.4	-6.04
Titanium LI	-81.8	------	------	-34.2	-6.87
Titanium 64	-55.3	0.006%	0.81	-20.3	-11.5
Cronidur 30	91.9	1.339%	11.2	45.7	-144
Hastelloy C276	126.6	1.127%	17.5	82.3	-101
Inconel 625	156.1	1.264%	17.6	88.8	-41.0
Brine					
Titanium LI	-120.6	------	------	-39.4	13.4
Titanium 64	-99.5	0.008%	1.51	-24.3	13.8
Titanium CP	-73.1	0.009%	2.85	-11.2	25.4
Cronidur 30	132.9	1.819%	10.6	52.4	-148
Hastelloy C276	153.3	1.357%	16.7	79.2	-61.6
Inconel 625	175.5	1.405%	17.3	91.4	-47.3

A more comprehensive analysis of the galvanic coupling results is given in Section 4.5 which includes the specific voltage displacement averages and rate changes associated with each couple test. In Table 7, simple sums or totals of these averages relative to the Open Circuit Potential (OCP) are provided in an attempt to portray the relative behavior of the critical parameters for each metal in a hypothetical mixed material environment from an overall compatibility perspective. As indicated, the total shift in galvanic couple potential for the titanium metals (the sum of the differentials of each metal interacting with each of the other metals across the solution) is negative for all three Titanium candidates. This reveals the highly cathodic and self-protective nature of Titanium and its alloys. When the counter metal is anodic to the test metal, the resulting potential of the test metal is forced below its OCP, implying that these metals are well protected in the six metal environment. In contrast, when a counter metal causes an in increase in the test metal potential above its normal OCP, the test metal becomes more vulnerable to galvanic effects although none of these metals showed any visible signs of corrosion or degradation whatsoever as the sample areas all exhibited about the same appearance before and after testing.

As noted earlier, relative to any formal Galvanic Series, each of the individual changes comprising the total OCP deviations shown in Table 7 are very small. The actual totals have no true significance as they were tabulated only to help illustrate the possible qualitative differences that might exist between the metals in a mixed system. Note that while Cronidur seems to be more susceptible to pitting-type corrosion effects than any of the other candidates, its resistance to general corrosion is impressive. From this work, it can be concluded that all six metals are compatible with each other in both test solutions. Overall, Table 7 could infer a vague but general galvanic group ranking for these metals in terms of apparent nobility in the subject test solutions: Titanium CP, Titanium LI, Titanium 64 > Cronidur 30, Hastelloy C276, Inconel 625. However, such a ranking has not been uniquely quantified here.

4.0 Technical Discussion of Results

4.1 Oxidation of Passive Metals in Air

Corrosion of a metal or alloy can be defined as the degradation or loss of the metal via electrochemical oxidation with the surrounding environment. In most cases, the environment is rich in oxygen which becomes the primary oxidizing agent in the process while one or more oxide compounds of the metal become the primary corrosion products that precipitate on the metal surface. In moist or wet neutral-to-basic environments, hydroxides of the metal will also form, so the product may be an oxide-hydroxide mixture. The bulk of the oxidation product is comprised of oxides which grow from the original metal interface boundary inward and outward while terminal hydroxyl groups directly interface the moist environment along the exposed boundaries and/or within pore channels of the oxide-hydroxide layer. For many iron-based alloys, the base metal recesses inward while the frail iron oxide products are loosely bound, easily washed away or are otherwise removed by environmental forces, leaving the bare metal surface exposed. In these cases, the oxide (or oxide-hydroxide) product provides no protection against corrosion and destructive oxidation of the base metal continues unabated.

Common published Galvanic Series consist of a series of metals whose open circuit potential has been individually determined by experiment in a specific environment (such as sea water) and then ranked to provide a table of the metals from low to high voltage. A variety of these is tables is available. Many are derived from MIL-STD-889 and MIL-HDBK-1003. The higher the measured potential of a metal or alloy, the more resistant to corrosion the metal is. Highly corrosion resistant metals are referred to as 'noble'. As the measured open circuit potential increases, the nobility increases so that all the metals near the top of the table are considered to be highly noble. Bare surfaces of silver, gold and platinum derived their resistance to corrosion purely as a result of their very high open circuit potential. However, all the other metals near the top of the Galvanic Series, many of which are comparable to and sometimes better than silver, derive their high nobility through a completely different mechanism. This is the case with the six metals under investigation. These six metals are resistant to corrosion in almost all known environments with the exception of hot, concentrated mineral acids or halide solutions. Such media may destroy the protective oxide layer faster than it can repair itself.

When freshly machined or etched and exposed to the air, almost all the metals near the upper (noble) region of the Galvanic Series undergo oxidation as they form a thin, continuous protective oxide layer which prevents degradative corrosion of the base metal. The base metal is oxidized by molecular oxygen which is reduced to oxygen ions. This extraordinary defense mechanism is spontaneous and deposits several Angstroms of metal oxide (a few crystal layers) almost instantly upon exposure. The growth profile is exponential as the rate is very high initially and then tapers off over time as a steady state is attained. Metal atoms are chemically oxidized (electron loss), $2M \longrightarrow 2M^{+2} + 4e^{-}$, while oxygen molecules are reduced (electron gain) as each splits into two oxygen ions, $O_2 + 4e^{-} \longrightarrow 2O^{-2}$. The net result is $2M + O_2 \longrightarrow 2MO$. During the oxidation-reduction (redox) reactions, two mutually inclusive dimensional processes are occurring, the base metal is receding or 'etching' inward as metal oxide fills the recessed volume and also progresses (grows) outward. The oxide phase is usually bulkier, lower in density and occupies more volume than the metal. This scenario describes the formation of the native (passive) oxide layer on a metal surface during natural passivation in air. These ideas are illustrated in Figure 8 using a simplified chromium (Cr) rich alloy as an example.

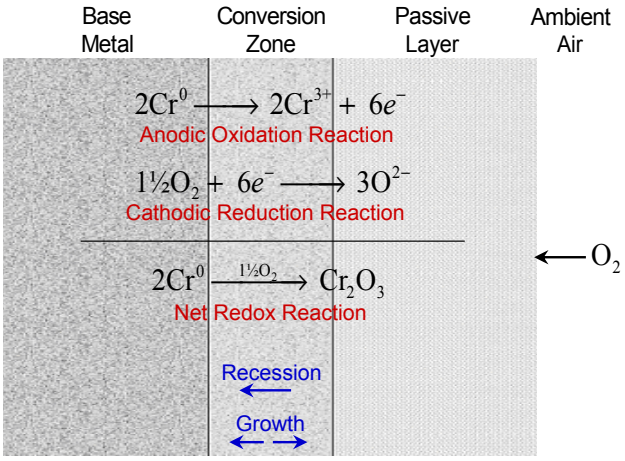

Figure 8: Illustration of a chromium alloy undergoing native oxide layer formation (passivation) in ambient air.

The passivation process takes off instantly and reaches a stable plateau (at steady state) when the oxide thickness attains a satisfactory level of protection. The gradient conversion zone is the region or layer along the metal-to-oxide interface in which the base metal gradually transitions into oxide. It is responsible for the strong adhesion of the oxide layer to the metal substrate and the extraordinary mitigation of mechanical and thermal property differentials between the metal and oxide which might otherwise separate or spall away. Compared to the oxide layer, this intermediary layer is quite thin and may increase in thickness slightly over time as oxide growth commences. The conversion zone corresponds roughly to the region where electrons are consumed or depleted, that is, the depletion zone.

Initially, equilibrium reaction rates for anodic oxidation of the metal and cathodic reduction of molecular oxygen are shifted in the forward direction, leading to recession of the base metal and growth of the passive oxide layer. All reactions are under activation control but become increasingly diffusion-controlled as oxygen molecules must migrate through the growing oxide thickness. Eventually the process levels off as oxidation ceases and all the rates approach zero at a steady state. If some event or condition in the environment induces damage to the oxide, reaction equilibriums are again shifted to the right as the metal's self-repair mechanism quickly kicks into gear generating oxide on an 'as needed' basis. When sufficient oxide replenishment and thickness repair are complete, the system again approaches a steady state. In short, the passive layer acts a stout barrier against further oxidation of the base metal and rapidly repairs itself whenever breached. However, not all metal oxide layers are equal. The layers that form on titanium and its alloys are measurably superior to those on alloys rich in chromium and/or nickel. In general, the final oxide layer at steady state might be in the order of ~ 1 to 3 nm in thickness with a corresponding recession/penetration depth into the base metal of ~ 0.3 to 1 nm.

Note: Except where noted or apparent, theories, concepts, mechanisms and illustrations in Sections 4 through 5 are the perception and handiwork of the author. No guarantees are given regarding their accuracy or correctness in other application.

Stoichiometric redox reaction rates are not exactly the same as the volumetric rates of base metal recession and oxide thickness growth since the latter rates are dependent on the respective densities of the base metal and the oxide layer, as well as the number of electrons transferred from the metal to the oxide during the process. In salt water environments, the final thickness of the layer may be a little greater as the demand for protection is increased. In acidic solutions, oxide layer thicknesses may be thinner as oxide growth must compete with acidic dissolution/hydrolysis. In basic solutions, oxide-hydroxide layer thicknesses are expected to be much greater. At steady state, passive layer thickness varies linearly with pH. Also, if a potential is applied and the system allowed to reach a new steady state, the layer thickness is expected to be linearly related to the applied voltage. Generally, the surface oxide on a passive metal will adapt as it proceeds to protect the base metal from the particular environments it is placed in.

Passive layers that grow naturally on chromium alloys which also contain substantial fractions of nickel or iron, such as Inconel, Hastelloy and Cronidur, will tend to generate appreciable quantities of their respective chromites within the composite oxide phase. Several chromite stoichiometries are possible. For example, the oxide layers on Inconel and Hastelloy are expected to contain considerable levels and possibly different stoichiometries of nickel chromite such as $NiCr_2O_4$ and $Ni_2Cr_2O_5$ while the oxide phase the forms on Cronidur is probably high in iron chromites such as $Fe_2Cr_2O_6$. There are others. The presence of these alloy oxides is believe to enhance oxidation protection properties above and beyond that provided by straight Cr_2O_3, as trivalent chromium Cr^{3+} (chromite ion) is converted to hexavalent chromium Cr^{6+} (chromate ion) when additional oxygen comes into the system. For nickel alloys, example reactions might follow pathways similar to . . .

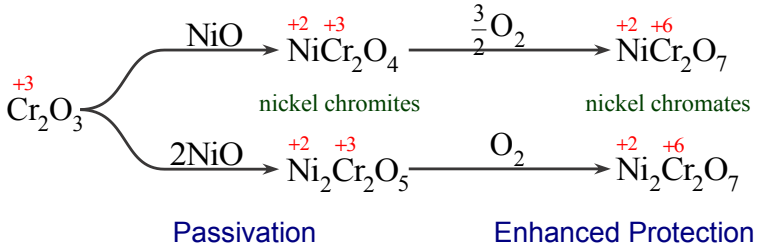

For stainless steels containing high levels of nickel, formation of nickel-iron chromites is likely ($NiFe_2Cr_2O_7$). With Cronidur, which contains chromium but no nickel, the generation of iron chromite and chromated via the oxidation of Cr^{3+} to Cr^{6+} could be represented by . . .

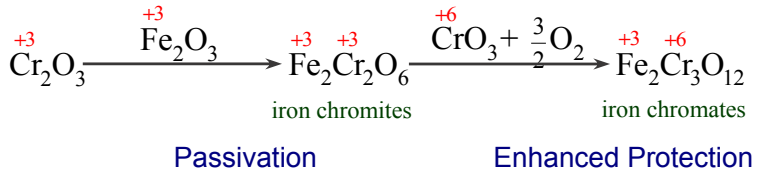

These types of alloy compounds are expected to develop in most acidic media as well, including the two solutions under study. In addition to improved corrosion resistance, the chromite-chromate conversion process that occurs in high nickel alloys such as 625 and C276 could conceivably play a role in certain changes taking place during electrochemical polarization which are associated with increased metal oxide phase separations and the oxide's inherent semiconducive properties.

4.2 Open Circuit Potential

4.2.1 The Electrical Double Layer (EDL)

In general, when an air-passivated metal is immersed in an electrolyte (a solution of ions), the oxide layer changes and adapts to the new environment. In addition to ions, aqueous solutions usually contain an abundance of available oxygen. The reactions and electrochemical processes that occur in a liquid electrolyte can be quite different than those associated with ambient oxygen-induced exposure. If the ions are non-aggressive to the oxide, negative ions (anions) will tend to be adsorbed into the outer lattice planes of the oxide, leaving the local solution directly adjacent to the oxide surface rich with positive ions (cations). Thus, at the oxide-solution boundary interface, anions (or electrons) in the oxide phase attract cations in the solution phase to form a parallel 'double layer' of charges along the interface. For the solutions under study, the cations are primarily hydrogen ions. The negative charges in the solid oxide phase accumulate and organize themselves along the oxide boundary while cations in the solution are mobile and less organized as they randomly diffuse out into the bulk solution.

This arrangement comprises the electrochemical or 'electrical double layer' (EDL) which is predominant in almost all colloids, dispersions, particle systems and porous networks throughout nature and industry, including emulsions, milk, blood, paints, plastics, ceramics, cements, fibers, composites, and . . . electrode surfaces. The EDL begins to form immediately upon exposure to the electrolytic and changes or adapts as the types and concentrations of solvated ions near the interface vary over time. Overall, the system is neutral as the quantity of negative charges in the EDL is balanced by the positive charges near the solution interface. If the solution is acidic, as with the subject pretreated and brine solutions, anodic effects are much greater as hydrogen ions will begin to dissolve the oxide layer. Initial formation of the EDL results in a relatively high electrical capacitance being generated as the layers of parallel ions and counter ions are initially very close to one another (recall that capacitance is inversely related to the distance between opposite charge planes). These ideas are illustrated in Figure 9 using a Cr-rich alloy as an example which depicts some of the initial events occurring during the first second or two after the air-passivated surface comes in contact with the solution.

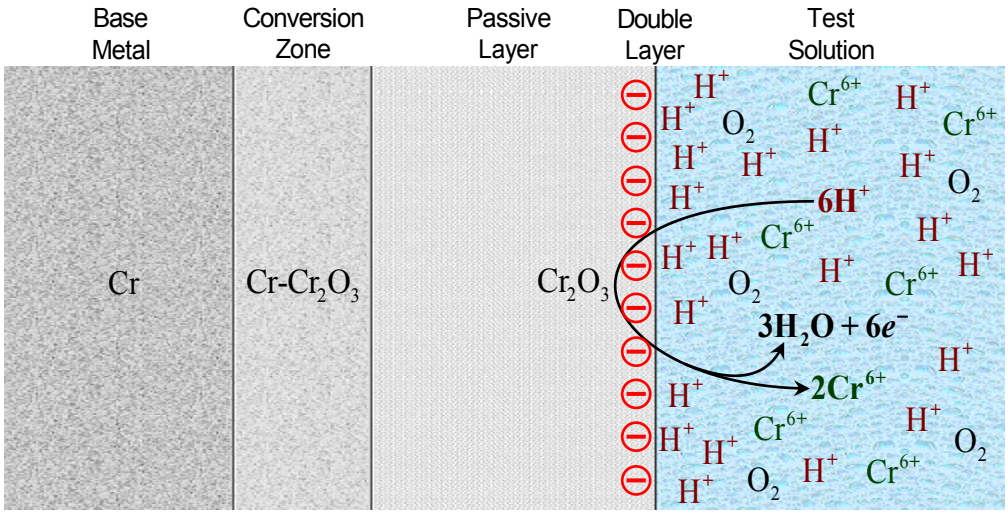

Figure 9: Illustration of a chromium alloy seconds after immersion in an acidic electrolyte.

An electrolyte is considered to be an 'anodic' medium if it forces a naturally passivated metal to undergo further oxidation reactions to protect itself. A medium is considered to be 'cathodic' if the oxide layer is chemically reduced and begins to dissolve or strip away since its protective properties are no longer needed. Reduction of local metal ions or plating may also occur in a cathodic environment. Both the pretreat and brine test solutions are considered to be highly anodic liquid mediums with pH levels in the 2-3 range. Unprotected alloy iron substrates would be attacked relentlessly and corrode away in short duration while the mediocre oxide layer on aluminum alloys would likely exhibit poor survivability over longer time periods. However, almost all the metals near the top of the galvanic series, particularly the ones under study here, have already been demonstrated to possess exceptional resistance to attack in these solutions as their mechanisms of oxide regeneration along with the highly tenacious nature of their oxides are exemplary. After the essential EDL is established, hydrolytic chemical attack of the oxide commences, resulting in dissolution of the oxide which in turn compels the base metal to generate more oxide to protect itself. The final oxide layer formed on metal surfaces in some aggressive environments can be several times thicker than the original air-formed oxide layers.

Now it is understood that the bulk of the film thickness which develops during the first few minutes and hours of exposure in the subject test solutions is comprised of two different layers, forming a 'bilayer' coating comprised of a primary barrier, which provides the principal corrosion protection and a precipitated porous layer on top of the barrier layer which is saturated with the solution. The primary barrier is adjacent to the metal surface (extending away from the conversion zone) and is believed to be composed of a mixture of base metal oxides with an amorphous to semi-crystalline structure. The barrier layer is very similar to the air-formed oxide layer. The porous layer develops due to dissolution and precipitation of the barrier layer. Its macrostructure is gelatinous with pore channels extending from the solution interface to the primary barrier oxide sub-layer. The pore channels fill with solution and become hydrated while internal EDL surfaces form all along the pore walls. The net result is a dispersion and bulk separation of the charges in the outer layer directly interfacing the solution with an accompanying reduction in capacitance. The porous layer may be thicker than the barrier layer and attains a lower bulk density. These ideas are illustrated in Figure 10 using a Cr-rich alloy as an example.

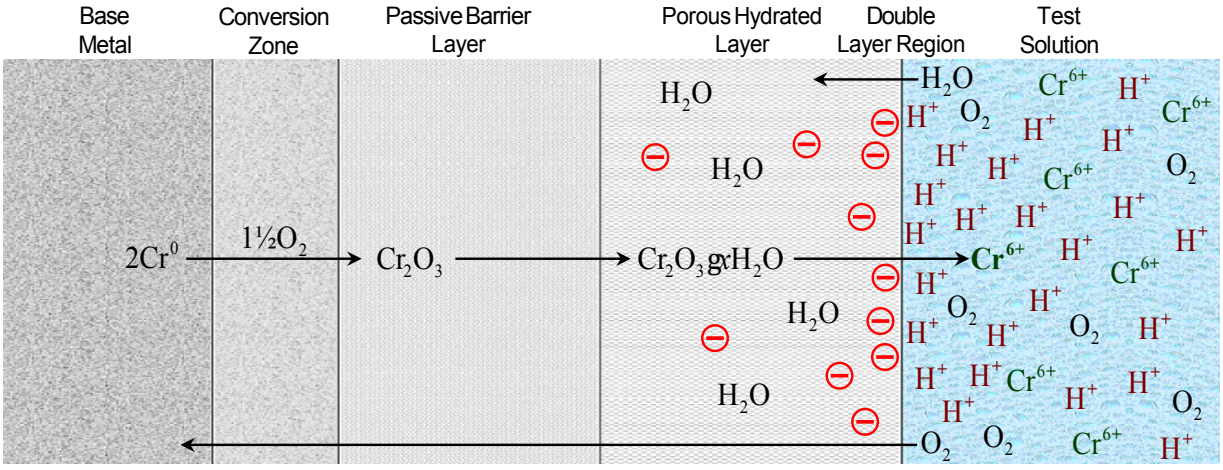

Figure 10: Illustration of a chromium alloy minutes after immersion in an acidic electrolyte.

In this state, the bulk distribution of ions creates a more generalized EDL structure within the porous phase that is spread out over space with a capacitance that starts out high but approaches a low constant value when a steady state is eventually attained. While a small space charge capacitance is associated with the barrier layer, the greatest contribution to the total capacitance comes from the EDL field. When the EDL initially forms, the accumulation of parallel charges also produces a small intrinsic voltage (an overvoltage) as the original air-formed open circuit potential (OCP) is forced to a new OCP controlled by the test medium. These changes are often reflected on the OCP plot. When first exposed, parallel charges q rapidly assemble along the oxide-solution interface and then the porous layer begins to develop via hydrate precipitation of the oxide. Initially, growth rates for both the barrier oxide and porous layers are maximum. During the following minutes or hours, these rates may slightly decrease but then rapidly diminish prior to the steady state plateau (~ 85-90% of the steady state value). For the majority of OCP scans collected throughout this study, the intrinsic potential appeared to increase during the ramp up to the steady state. Thus, as the passive layer adapts to the test solution, the differential capacitance C of the EDL/porous layer decreases over time t while its thickness L_p increases as positive and negative charges become widely scattered across the thickness of the layer. That is . . .

$$\frac{dL_p}{dt} \propto \frac{1}{C}$$

Meanwhile, the potential difference η (the intrinsic overpotential) between the barrier layer and the porous layer/solution phase increases during the up-ramp according to . . .

$$\frac{d\eta}{dt} = \frac{1}{C}\frac{dq}{dt}$$

This could imply that the increase in potential $d\eta/dt$ or equivalently, the slope of the potential trace during the ramp toward steady state parallels the precipitation process possibly reflecting the increase in porous layer thickness. In many OCP runs, an associated current change was also detected at the beginning of the scan (usually a decreasing slope) which appeared to track opposite to the voltage ramp. This rapid current change dI/dt during the first few minutes of exposure may infer a slight current imbalance associated with the intrinsic overpotential, possibly reflecting the increase in barrier layer thickness in compliance with the Butler-Volmer relation (covered later). As with most passive oxides, the primary barrier layer is basically an electrical insulator or semiconductor while the permeable porous layer is highly conductive to ion transport. Thus, the intrinsic current deceases as the barrier layer grows in thickness while the intrinsic overpotential increases as the porous layer increases in thickness. It can be recognized that accessibility of reactants and products to and from the barrier layer across the porous layer are controlled primarily by Darcy-type diffusional forces through the pore channels while access through the barrier layer to the metal surface becomes increasingly Fickian diffusion-inhibited. Figure 11 shows the OCP scan results for one of the Inconel samples in pretreat along with the associated analysis as an example of the approach taken to evaluate these data and concepts.

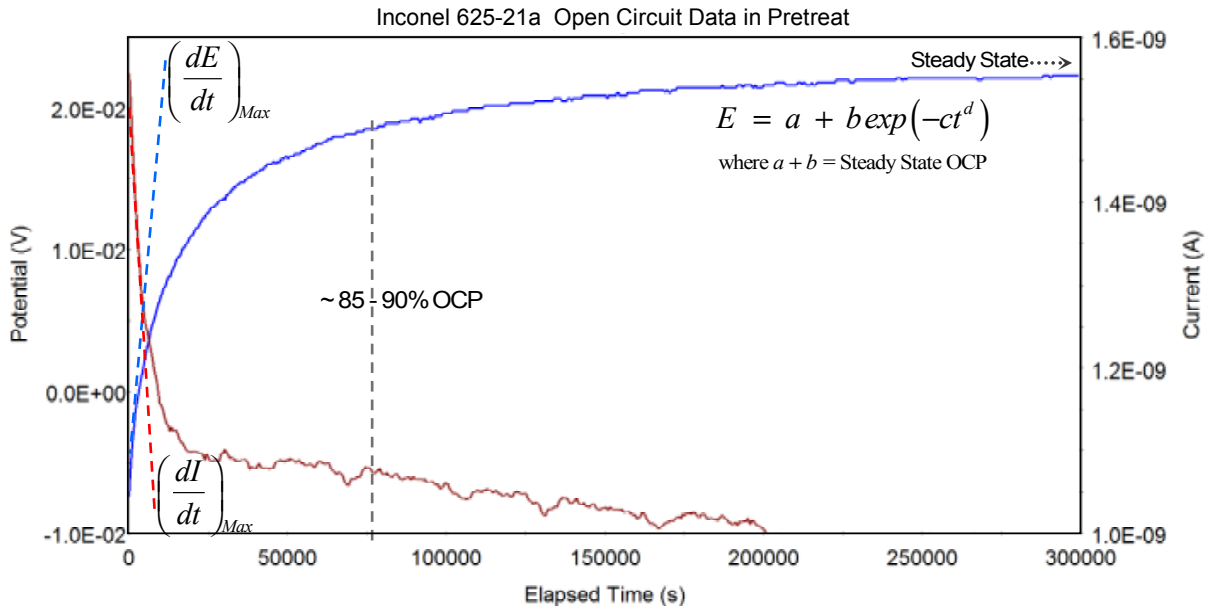

Figure 11: Data plot and analysis of one of the Inconel OCP test runs.

4.2.2 The Open Circuit Steady State

After the EDL structure has been established, the air-formed passive layer also begins to dissolve while a porous oxide-hydroxide layer precipitates on the outer surface of the barrier oxide sublayer. As oxygen diffuses into the barrier layer, the base metal continues to oxidize very slowly, forming new barrier oxide in the conversion zone as older oxide near the solution interface continues dissolving and/or transforming into the oxide-hydroxide phase. The maximum rate changes occur shortly after exposure is initiated and the majority of all the events leading up to the steady state plateau take place during the first 85-90% of exposure time. When a steady state plateau is eventually attained, the rates of anodic metal oxidation k_1, and cathodic reduction of oxygen (and/or hydrogen) k_2, become constant, equal and opposite to each other ($k_1 = k_2$ = constant) with equilibriums that are shifted slightly in the forward direction. Similarly, the rates of base metal (M) recession k_{Met}, and metal oxide (MO) growth k_{Ox}, become constant, opposite, mutually associated and relegated to the oxide dissolution rate k_{Dis} such that $k_{Ox} = k_{Dis}$ = constant). The rate of oxide dissolution drives the sequence of reactions occurring during open circuit conditions as it ejects metal cations M^{2+} into solution. These concepts are illustrated in Figure 12.

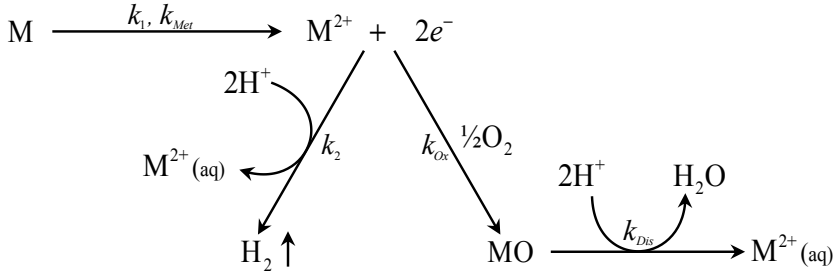

Figure 12: Sequence of reactions occurring during open circuit exposure in acidic solution.

Theoretically, k_{Dis} would be a true constant at steady state, however, due to compositional variations and thermal fluxuations in the solution, the rate of oxide dissolution may vary slightly from one region to another along the surface. During the ramp up (or down) toward the steady state, k_1, k_2, k_{Met} and k_{Ox} are not constant as these rates start out high initially and decrease over time as the reactions rapidly play 'catch-up' to k_{Dis}. The final open circuit potential at steady state may be referred to as the Open Circuit Potential (E_{OC}), the Steady State Potential or the Corrosion Potential (E_{Cor}). The capability for these types of metals to replenish lost oxide far exceeds the forces of dissolution in most anodic solutions, including the two solutions under study here. When the system becomes stable at the steady state, only a very small amount of base metal recession and oxide regeneration are actually occurring in order to compensate for the small level of dissolution that is taking place.

Not all of the OCP plots in this study were as straightforward or visually uniform as the data depicted in Figure 11. Most of the runs required many days and sometime weeks to reach a steady state condition and scheduling did not permit such time commitments due to the number of tests mandated. Many plots were laden with peaks and valleys making them difficult to evaluate. Intensive curve-fitting trials were conducted on most of the plots in order to ascertain the real OCP as best as possible. Most of the OCP plots throughout this study could be fitted to modified exponentials or Weibull functions containing parameters that identify the theoretical steady state value at infinite exposure time. Additionally, some of the runs exhibited other phenomena and events that needed to be better understood. Figures 13 and 14 show a couple of these OCP runs, and Table 8 provides the summary of averages developed for this study covering the OCP phase of the testing.

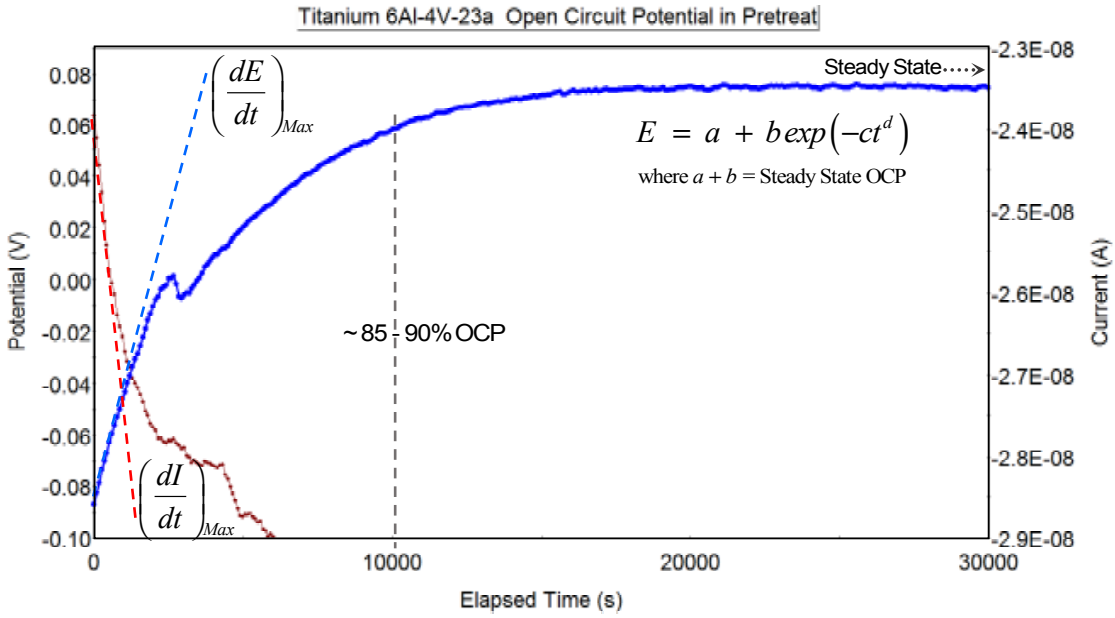

Figure 13: Data plot of one of the Titanium 64 OCP test runs in Pretreat solution.

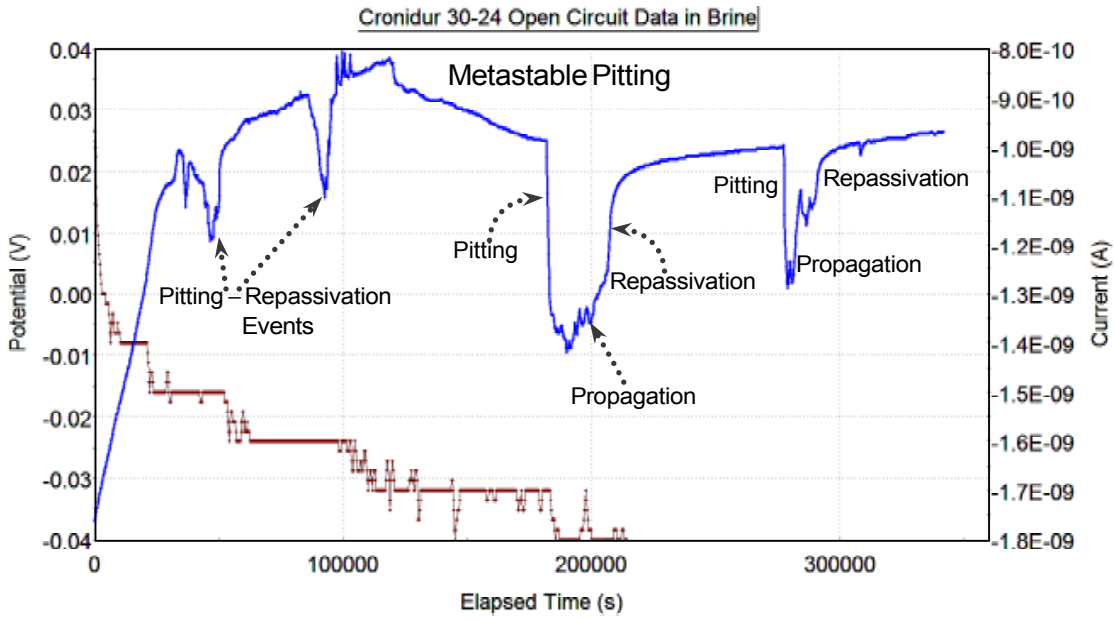

Figure 14: Data plot of one of the Cronidur OCP test runs in Brine solution.

Metastable pitting appeared to be pronounced with a couple of the Cronidur samples in brine as illustrated in Figure 14. However, most of the Cronidur OCP runs did not reflect this type of behavior during OCP testing. As indicated earlier, these transients are suspected to be minor initiation events occurring within the oxide layer. However, pitting into the base metal during accelerated cyclic polarization testing was one of the key artifacts demonstrated for the Cronidur samples, particularly in the brine media. Cyclic polarization test results are covered in Section 4.4.

Table 8: Reduced summary of open circuit data averages for both test solutions.

Apparent Relative Nobility Relative Corrosion Susceptibility			Relative Growth Rate Indicators of Bilayer Oxide-Hydroxide Coatng			Stabilization Period Time To Reach Steady State	
PreTreat	Steady State Potential (mV_{AgCl})	Relative Oxidation Susceptibility	PreTreat	*dE /dt* Porous Layer (μV/sec)	*dI /dt* Barrier Layer (pÅ/sec)	PreTreat	~90% of Steady State (hours)
Titanium CP	93.9	0.30%	Titanium CP	47.9	-2.18	Titanium CP	11.8
Titanium 6-4 LI	80.8	0.34%	Titanium 6-4 LI	29.4	-1.49	Titanium 6-4 LI	12.3
Titanium 6Al-4V	77.4	0.34%	Titanium 6Al-4V	35.6	-1.36	Titanium 6Al-4V	14.6
Cronidur 30	39.0	4.53%	Cronidur 30	14.2	-0.89	Inconel 625	20.6
Inconel 625	23.4	2.92%	Inconel 625	22.6	-0.67	Hastelloy C-276	27.6
Hastelloy C-276	18.7	3.63%	Hastelloy C-276	25.6	-0.57	Cronidur 30	33.4
Brine			**Brine**			**Brine**	
Titanium CP	104.3	0.30%	Titanium CP	21.5	-1.17	Titanium CP	12.6
Titanium 6-4 LI	97.0	0.34%	Titanium 6Al-4V	14.1	-0.97	Titanium 6-4 LI	13.1
Titanium 6Al-4V	95.2	0.34%	Titanium 6-4 LI	13.3	-0.82	Titanium 6Al-4V	13.9
Cronidur 30	46.5	4.52%	Inconel 625	9.63	-0.34	Inconel 625	25.0
Inconel 625	38.2	2.91%	Hastelloy C-276	10.9	-0.22	Hastelloy C-276	25.9
Hastelloy C-276	32.3	3.61%	Cronidur 30	7.78	-0.11	Cronidur 30	37.4

As indicated in Table 8, the titanium candidates appear to exhibit the greatest nobility in both solutions. Additionally, their barrier layers seem to grow faster than the other metals (higher negative slopes), and their steady state stabilization periods were the shortest. The Inconel, Hastelloy and Cronidur metals are similar in many respects, while the three Titanium alloys are closely matched to each other. In terms of relative susceptibilities, the results suggest that the Titanium metals are substantially superior to the other three metals. Both general or pitting corrosion are possible during open circuit exposure. However, it should be emphasized that none of the metals evaluated here showed any signs of corrosion, pitting or surface degradation as a result of open circuit exposure. Nevertheless, the higher susceptibility averages indicated for Cronidur may pertain to propensities associated with pitting while the values acquired for Inconel and Hastelloy could be dominated by general corrosion probabilities. This would be in agreement with visual observations and the test results obtained during cyclic polarization. It is important to realize that all the data generated in this study pertains only to the specific test solutions which were evaluated. The results could be substantially different than those obtained in other test media such as seawater or alkaline solutions. Finally, it should be noted here that the Gamry Instruments and Software Suites do not appear to provide the capability to evaluate early *dI*/*dt* slopes as possible current traces are not monitored or available during OCP test runs.

4.3 Linear and Tafel Polarization

There are two primary methods for determining the rates of general corrosion, metal recession and passive oxide growth: Linear and Tafel polarization. These two techniques will be covered in the following subsections and then a table of the final data averages and results will be presented.

4.3.1 Test Configuration and Parameter Definition

For the situations of interest here, anodes refer to positively charged sites on the electrode (the test metal) which attract anions, while cathodes refer to negatively charged sites which attract cations. Oxidation reactions occur at the anode sites as electrons are extracted into the solution causing the sites to become positive, while reduction reactions take place at cathode sites leading to negatively charged sites. Anodes invite oxidation processes such as anodizing, passivation and rust, while cathodes invite reduction reactions which promote metal deposition and cathodic dissolution of the oxide layer. Thus, during electrochemical reactions, electrons flow from anodic sites to cathodic sites while electric current flows from cathodic sites to anodic sites. Once the EDL forms, anodic surfaces become negative due to the accumulation of departing electrons at the solution interface while the local interfacing solution becomes more positive as a result of dissolved metal ions.

On a larger scale, a common three-electrode test configuration was employed for this study in which electrons are supplied by the potentiostat to a counter electrode (comprised of platinum). The counter electrode polarizes the working electrode (the test sample), causing oxidation at that electrode which loses electrons to the solution. This results in an overvoltage between the working electrode and a selected reference electrode placed in close proximity to the working electrode surface. A simplified diagram of the current-voltage measurement configuration used in this work is provided in Figure 15.

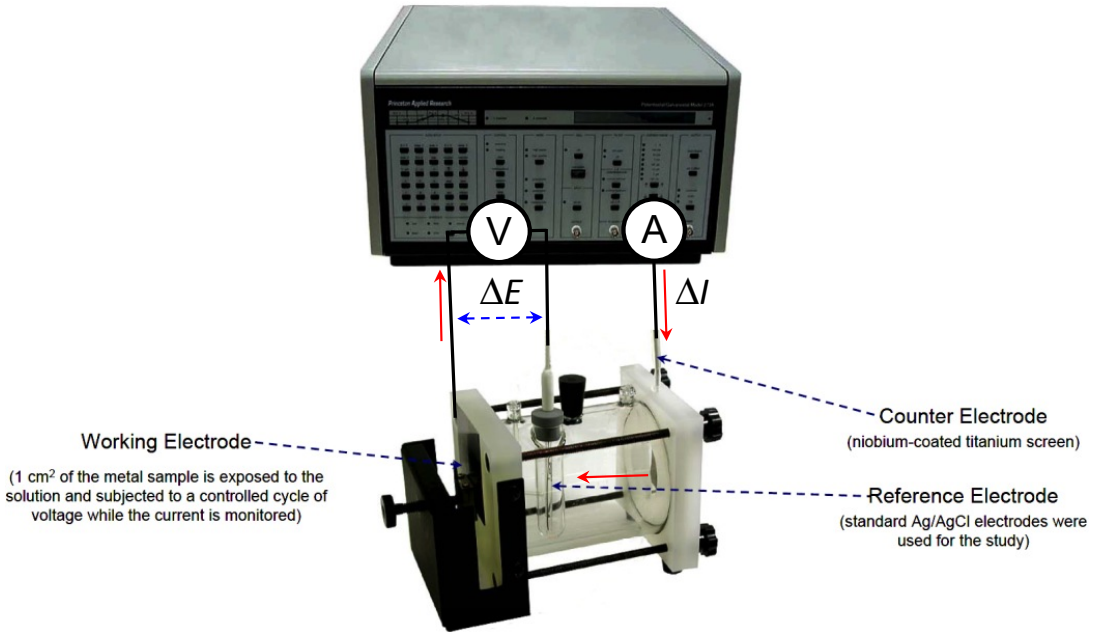

Figure 15: Simple diagram of the PAR potentiostat – and flat cell connections used in this project.

There is no absolute reference for potential, so the quantitative meaning of the measured voltage is dependent on the specific reference electrode that is used to make the measurement. The most common reference electrodes for electrochemical testing include the standard hydrogen electrode (SHE), the standard calomel electrode (SCE) and the silver/silver chloride electrode (Ag/AgCl) with the latter being used throughout these studies. In most electrolytic test cells, the resistance of the test solution skews the measurements. In order to minimize the ohmic drop due to solution resistivity, a special Luggin capillary tube was utilized which connected the reference electrode chamber to within a couple of milliliters of the sample surface. This configuration was standard as provided with the PAR Flat Cell apparatus. Also, the exposed sample test area in the flat cell configuration utilized throughout this work was exactly $1cm^2$. With this understanding, the terms current and current density are sometimes used interchangeably.

Within the test cell and throughout every DC polarization test cycle, the current is always directed from the counter electrode to the working electrode (the sample) while electrons are always flowing out of the working electrode. If a small voltage E is applied that is below the OCP (or E_{OC}), the sample becomes cathodically charged with an excess of electrons and a corresponding cathodic current I_c. This overpotential can be represented as $\eta = E - E_{OC}$. As the applied voltage is increased up toward E_{OC} (which is also recognized as E_{Cor}), the sample becomes less cathodic and the outflow of excess electrons diminishes. This is not chemical oxidation since the departing electrons are provided by a pool of excess conduction electrons, not valence electrons. At E_{Cor}, the net electron flow becomes zero as the anodic and cathodic currents are exactly equal. When the voltage continues above E_{Cor}, valence electrons begin leaving the sample which changes polarity and starts to anodically oxidize as it is driven by the anodic current I_a. In either case, the sample becomes polarized when its potential is forced away from its equilibrium value at OCP and the net current I_{net} becomes a mixture of I_c and I_a.

4.3.2 The Polarization Curve

At the equilibrium steady state defined by E_{Cor}, the net current is zero since $I_c = -I_a$. This is often referred to as the exchange current I_e, (equivalent to I_{Cor}) which is a measure of the rate of electron transfer from metal to either oxygen molecules, hydrogen ions or other electrophiles within the test solution. The exchange or corrosion current is proportional to the oxidation/corrosion rate at the steady state where equilibriums exist between oxidation of metal atoms at anodic sites, for example . . .

$$2Cr^0 \rightleftharpoons 2Cr^{3+} + 6e^- \quad \text{and} \quad 2Fe^0 \rightleftharpoons 2Fe^{3+} + 6e^-$$

and reduction of molecular oxygen and/or hydrogen ions at cathodic sites,

$$\tfrac{3}{2}O_2 + 6e^- \rightleftharpoons 3O^{-2} \quad \text{and} \quad 6H^+ + 6e^- \rightleftharpoons 3H_2$$

Since the forward oxidation and reduction rates cancel each other at E_{Cor}, it becomes impossible to directly determine I_e or I_{Cor} as well as the desired recession, corrosion and oxide growth rates. Beyond about 50mV on either side of E_{Cor}, the process becomes dominated by either the anodic or cathodic reactions. These concepts are illustrated in Figure 16 showing a linear polarization data plot (in blue) for one of the Cronidur samples which was conducted from –15V to +15V (vs. Ag/AgCl) relative to the OCP in brine solution (E_{OC}=E_{Cor}). As will be demonstrated shortly, linear polarization techniques permit the determination of I_{Cor} and hence the desired oxidation/recession rates.

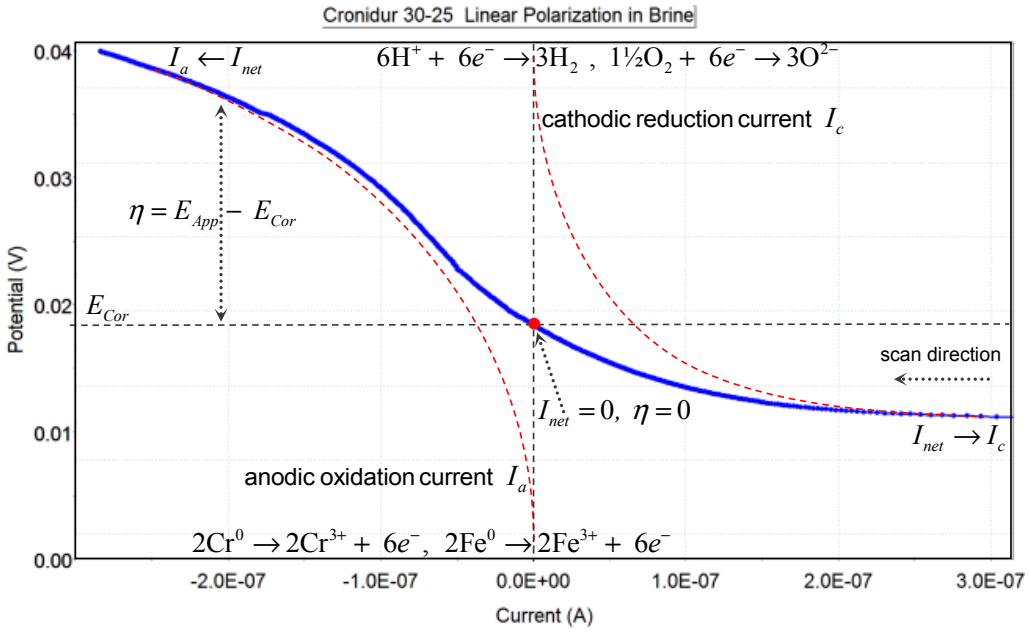

Figure 16: Current versus potential plot for one of the Cronidur samples showing anodic and cathodic branches.

Molecular congestion caused by the concentration of reactants and products along the metal-solution or oxide-solution interface may limit the current (and the transfer of electrons) since entities entering and leaving the reaction sites must diffuse through a thickened layer of solutes, reactants and products in a mass-transfer process across the adjacent solution. This is often referred to as concentration polarization and the redox reactions are said to be diffusion-controlled. This should not be confused with the type of diffusion that occurs within the barrier and porous layers where other factors contribute to or affect the ion transfer process. The interfacial solution region of heavy concentration is referred to as the Nernst diffusion layer which can vary in thickness, composition, diffusivity and current-limiting attenuation anywhere along the polarization curve, or it may not be significant at all if the reactions are activation-controlled. Activation polarization is predominant when the redox reactions are not impeded by diffusional phenomena but proceed strictly in a charge-transfer process. In many cases, the actual process may be a mixture of activation and concentration polarization.

The symmetry of the anodic and cathodic segments relative to the point E_{Cor}, $I_{net} = 0$ in Figure 16 may imply a small degree of diffusion-controlled reactions in the anodic region (where the passive layer is re-forming). A symmetry coefficient of 0.5 for both branches indicates an ideal activation-controlled situation which gives a perfect *sinh* curve form. The flat cell configuration in heated solution was pursued in this study in accordance with conditions utilized in previous studies. A rotating test sample would have facilitated a more uniform Nernst layer thickness with improved results. The apparent symmetry effects noted in Figure 16 may be more reflective of diffusional influences associated with the transport of species across the porous and barrier layers rather than concentration-limited transport within the adjacent solution. While the restricted transport of species through the fixed barrier and porous layers would likely be a combination of Darcy flow and Fickian diffusion, transport through the mobile Nernst layer would be exclusively Fickian in nature in accordance with Fick's first law. However, widespread diffusional attenuations in this work appeared to be minimal in many cases.

4.3.3 The Butler-Volmer Equation

Examination of all the linear, Tafel and cyclic plots generated for this study indicated that the majority of redox reactions occurring in both branches for all six metals was heavily influenced by activation-dominated processes. Figure 16 actually gives a plot of the well-known Butler-Volmer (BV) equation[5] which is applicable to activation-controlled redox reactions occurring on the same electrode. The BV equation expresses the measured current density I_{net} in terms of the exchange current density I_e ($\equiv I_{Cor}$), the overpotential $\eta = E_{App} - E_{OC}$ (or $E - E_{Cor}$), the number of electrons transferred during the redox reactions n, the cathodic and anodic symmetry coefficients s and $1 - s$ respectively, the absolute temperature T (which is 37°C = 310K for our study), the gas constant R = 8.314 Jmol^{-1}K^{-1}) and the Faraday constant F = 96,485 C-Vmol^{-1} . . .

$$I_{net} = I_c + I_a = I_c - |I_a|$$

$$I_{net} = I_e \exp\left(\frac{-snF}{RT}\eta_c\right) - I_e \exp\left(\frac{(1-s)nF}{RT}\eta_a\right) \quad (1)$$

Note: The negative sign for the anodic current is due to physics sign conventions. For single metal polarization, the current is always flowing from the counter electrode to the test metal regardless of whether it is in the cathodic or the anodic region. For rate estimates, current is treated as a positive number. However, in two metal galvanic coupling configurations, the current can flow in either direction depending on which metal is the cathode and which is the anode. As will be shown later, the direction of current flow in these situations has special significance.

The left term in Eq(1) defines the cathodic current while the right term defines the anodic current. Together, they make up the entire polarization curve. To be precise, this expression would contain terms for each reaction occurring in the process but is shown in this incremental form for simplicity as it may apply to either redox reaction set indicated in Figure 16. If the overpotential η is greater than about ±50mV in either direction, one term dominates while the other becomes insignificant. Thus, the currents in the cathodic and anodic branches for large overpotentials are described respectfully by . . .

$$I_c = I_e \exp\left(\frac{-snF}{RT}\eta_c\right) \qquad \text{and} \qquad I_a = I_e \exp\left(\frac{(1-s)nF}{RT}\eta_a\right) \quad (2)$$

These expressions can be rearranged to give the well-known Tafel parameters for each branch. For the cathodic current . . .

$$ln(I_c) = ln(I_e) - \frac{snF}{RT}\eta_c$$

$$2.303\log_{10}(I_c) = 2.303\log_{10}(I_e) - \frac{snF}{RT}\eta_c$$

$$\log_{10}\left(\frac{I_c}{I_e}\right) = -\frac{snF}{RT}\eta_c$$

from which . . .

$$\eta_c = \beta_c \log_{10}\left(\frac{I_c}{I_e}\right) \quad (3)$$

where the cathodic Tafel constant in volts is defined . . .

$$\beta_c \;=\; -\frac{2.303RT}{snF} \;=\; -\frac{0.0262}{sn}$$

Using Figure 15 as a rough guideline, if we let $n = 3$ and $s = \sim 0.75$, (where $s_c + s_a = 1$), the value of $|\beta c|$ comes out to 116 mV/decade compared to a value of 142 mV obtained for this sample during the experimental Tafel test run. Likewise, the anodic current becomes . . .

$$ln\left(|I_a|\right) \;=\; ln\left(I_e\right) \;+\; \frac{(1-s)nF}{RT}\eta_a$$

which leads to . . .

$$\eta_a \;=\; \beta_a \log_{10}\left(\frac{|I_a|}{I_0}\right) \tag{4}$$

where the anodic Tafel constant is defined . . .

$$\beta_a \;=\; \frac{2.303RT}{(1-s)nF} \;=\; \frac{0.0262}{(1-s)n} \;=\; 349 \text{ mV/decade}$$

This compares to a value of 416 mV obtained for this sample during the actual Tafel test run. Admittedly, there was a wide variation in the Tafel constant values determined throughout this work.

Now the Tafel expressions Eq(3) and Eq(4) are the so-called high-field approximations and can be written in slope-intercept form for future use . . .

$$\eta_c \;=\; a_c \;+\; \beta_c \log_{10}\left(I_c\right) \qquad \text{where } a_c = -\beta_c \log_{10}\left(I_e\right)$$

and

$$\eta_a \;=\; a_a \;+\; \beta_a \log_{10}\left(|I_a|\right) \qquad \text{where } a_a = \beta_a \log_{10}\left(I_e\right)$$

By definition, βc and βa are the activation-controlled cathodic and anodic Tafel slopes or 'beta' values respectively and will become important parameters during Tafel analysis. Note that βc represents a negative (cathodic) slope while βa is a positive (anodic) slope.

Now, the BV equation can be written in a more concise form . . .

$$I \;=\; I_{Cor}\left[exp\left(\frac{2.303\eta}{\beta_a}\right) \;-\; exp\left(\frac{2.303\eta}{\beta_c}\right)\right] \tag{5}$$

where $\eta = E - E_{Cor}$ can be the overvoltage in either direction.

4.3.4 Faraday's Law and Oxidation Rates

At the steady state, oxidation and reduction rates are equal and the current associated with either reaction (the exchange current or so-called corrosion current $I_e = I_{Cor}$) is a direct measure of the rates for these reactions. With strongly passivating metals such as the ones under evaluation here, I_e can be translated into the rates for base metal depth recession or penetration depth and oxide thickness growth. While chemical reaction rates measure the mass quantity of products generated, recession and growth rates are volumetric in dimension. They share the same number of transferred electrons but different geometrical densities which results in unique weight and volumetric changes associated with recession into the base metal and oxide growth which occupies the recessed metal volume and protrudes outward beyond the original metal line. Unfortunately, I_e cannot be measured directly and must be surmised by one of the linear methods covered in the next subsection. Once the exchange current is ascertained, a modification of Faraday's famous law can be used to estimate the rates associated with weight and volume changes during the oxidation process. The premise can be stated that for a given reaction, the current I is directly proportional to the sample weight gained or lost over time W_Δ/t, as well as the number of electrons n transferred during the reaction, and is inversely related to the molecular weight M_W of the electroactive species involved, where F is Faraday's constant . . .

$$\frac{I M_W}{n W_\Delta / t} = F$$

Recognizing that M_w/n is the equivalent weight W_{Eq} of the reacting species and utilizing its density ρ, weight changes and volume changes can be written respectfully in terms of the associated current, the equivalent weight and the density . . .

$$\frac{W_\Delta}{t} = I_{Cor}\frac{W_{Eq}}{F} \qquad \text{and} \qquad \frac{V_\Delta}{t} = I_{Cor}\frac{W_{Eq}}{F\rho}$$

The second expression is of importance in our study as it will permit the determination of the corresponding metal recession and oxide growth rates k_{Met}, k_{Ox} (both volumetric rates). By ascertaining the measured current, the equivalent weight of the base metal and composite oxide (which may be comprised of many components), and the mass density of the composite oxide, the rates for base metal recession and passive oxide growth become respectively . . .

$$k_{Met} = I_{Cor}\frac{W_{Eq,Met}}{F\rho_{Met}} \bullet c \qquad \text{and} \qquad k_{Ox} = I_{Cor}\frac{W_{Eq,Ox}}{F\rho_{Ox}} \bullet c \tag{6}$$

where c is a conversion factor incorporated to express the rates in the desired units.

For this study, weight constituents are given in grams and densities in g/cm^3 while the rates reported throughout this work are often given in Angstroms per day (Å/day) and mils per year (mil/year) whose c values are respectfully, 8.9588 X 10^7 Eq-sec-Å/C-cm-day and 1.2874 X 10^5 Eq-sec-mil/C-cm-year. Even though the number of electrons transferred from the metal must exactly equal the number of electrons transferred to the oxide, their equivalent weights (and volumes) are not equal. Special methods were formulated for estimating the equivalent weights associated with the six metals in this study along with their corresponding composite oxides and are covered in section 5.2.

4.3.5 Estimation of Currents and Rates

Before leaving Figure 16, one last concept should be explored centering on the point E_{Cor} at $I = 0$ (the red marker). Below E_{Cor}, the sample acts as a cathode, above E_{Cor}, the sample becomes an anode as it changes polarity. A technique developed by Stern and Geary (SG)[8],[9] many years ago provides a simple approach for estimating of the exchange current (density) and hence, the rates for corrosion, metal recession and oxide growth. They introduced the term of 'polarization resistance' R_{Pol} (or R_{Cor}) in analogy to Ohm's law or more precisely, they demonstrated that an inverse relationship exists between I_{Cor} and R_{Cor} when very small overpotentials are applied relative to E_{Cor} (scan ranges such as –20mV to +20 mV or smaller are typical) and that the slope of the polarization curve in this region $dE/dI = R_{Pol}$ describes a straight line as it passes through $I_{Cor} = 0$ (for cases with minimal linearity, the tangent line at this point can be used). Their work resulted in the following simple but very useful relationship . . .

$$I_{Cor} = \frac{B}{R_{Cor}} \tag{7}$$

where B is a proportionality parameter based on the Tafel constants in units of volts.

Historically, the SG equation has been utilized and experimentally validated many times since its introduction in the early 1900's. Validation of this approach can also be demonstrated mathematically through its relationship with the BV equation, and then the constant B can be determined. Utilizing the series expansion identity, $e^x = 1 + x + x^2/2! + x^3/3! + ...$, and neglecting the higher terms for low overpotentials, the BV Eq(5) can be written and rearranged . . .

$$I = I_{Cor}\left(\frac{2.303\eta}{\beta_a} - \frac{2.303\eta}{\beta_c}\right)$$

$$\frac{dI}{dE} = 2.303\left(\beta_a^{-1} - \beta_c^{-1}\right) I_{Cor} \qquad \text{where we let } \eta = dE \text{ and } I = dI$$

from which . . .

$$I_{Cor} = \frac{1}{2.303}\left(\frac{\beta_a\beta_c}{\beta_a + \beta_c}\right)\frac{dI}{dE} = \frac{B}{R_{Cor}}$$

and . . .

$$B = \frac{1}{2.303}\left(\frac{\beta_a\beta_c}{\beta_a + \beta_c}\right)$$

The SG method is the so-called low-field approximation. The approach is based on the assumptions that (a) all the reactions are reversible, (b) they are activation-controlled, (c) the energy barriers for the forward and reverse reactions are symmetrical, and (d) the results pertain only to general corrosion/oxidation events, providing no information regarding activity associated with localized pitting or crevice corrosion. In addition, the scan range is so small that the test is essentially nondestructive and results are obtained very quickly. This method is useful for long-term continuous corrosion monitoring. An example of the SG technique applied to one of the Hastelloy samples is given in Figure 17.

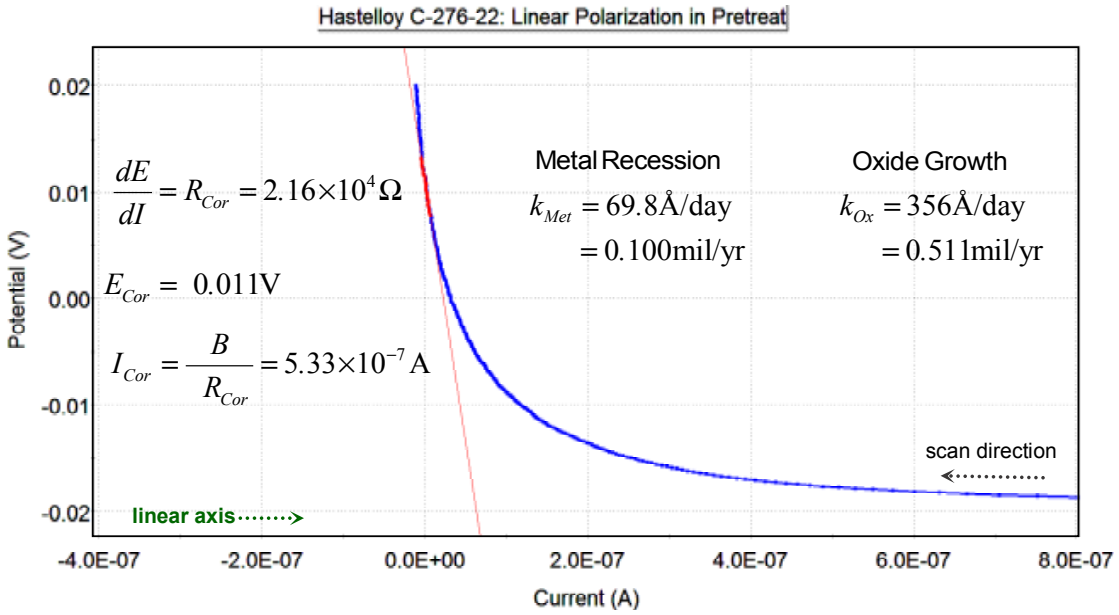

Figure 17: Linear polarization and analysis applied to one of the Hastelloy samples in pretreat solution.

The total oxide thickness includes recession depth plus outward growth. The Tafel constants used for these estimates were taken from subsequent Tafel testing. Note that the plot in Figure 17 utilizes normal ordinate or linear axes for both dimensions. If this same data is re-plotted in semi-log form, converting the *x* axis (the current density) into the corresponding $\log_{10}$ values, a low-field Tafel plot is obtained displaying a portion of the classic cathodic and anodic branches as shown in Figure 18.

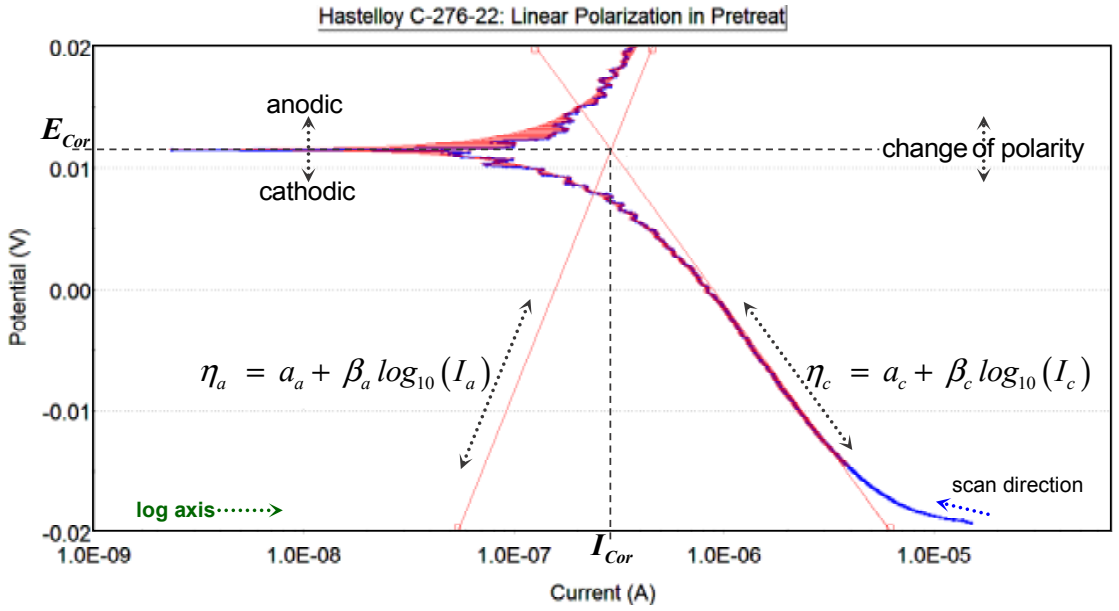

Figure 18: Semi-log plot of the linear polarization data shown in Figure 16.

In practice, a typical Tafel test run is scanned over a wider potential range in order to capture a greater portion of the anodic and cathodic branches. In essence, both of these approaches can be considered linear polarization techniques with information obtained from both the linear and log versions, and they both provide essentially the same results. However, when the semi-log version is utilized, the Tafel method utilizes a different analytical approach by applying linear fits along the straight portions of each branch whose intersection analytically identifies both E_{Cor} and I_{Cor}, and then the desired recession-oxidation rates can be computed from I_{Cor}. Figure 19 shows one of the Titanium 6Al-4V Tafel test runs over a scan range from −200mV to +350mV.

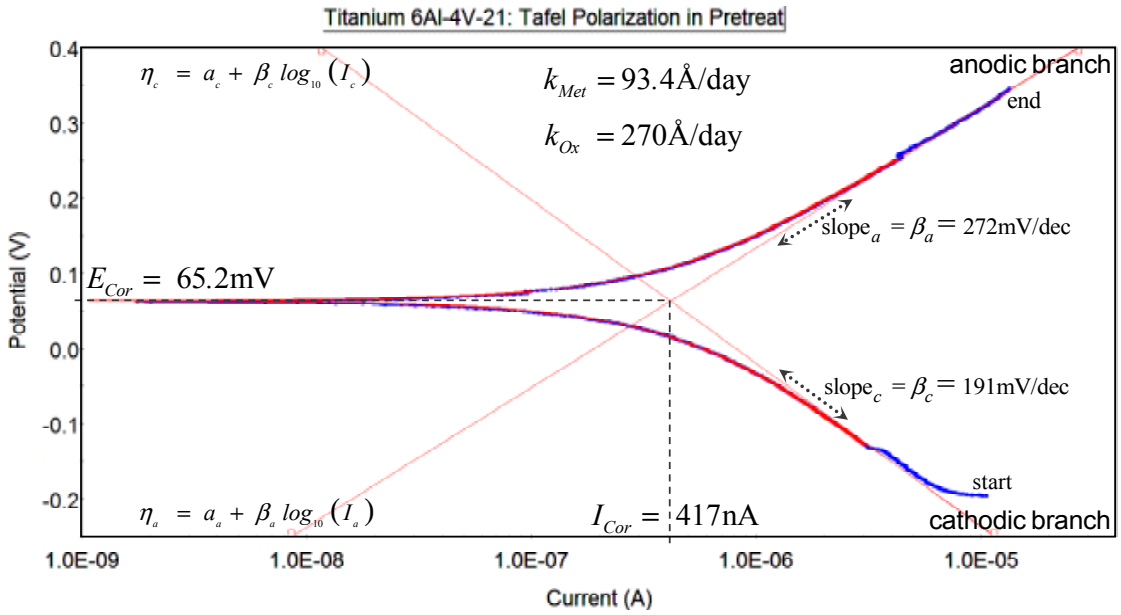

Figure 19: Semi-log Tafel fit of one of the Titanium 6Al-4V samples in pretreat solution.

In this format, $I_{Cor} = 0$ becomes the log inflection point and provides the key to determining all the other critical parameters in the Tafel plot. For this particular metal, while a number of reactions are possible with the alloying components, the fate of Ti itself will involve oxidation of the metal, reduction of hydrogen ion and molecular oxygen, and precipitation of the metal oxide which is hydrolytically dissolved in the acidic test solution. These processes are illustrated in Figure 20.

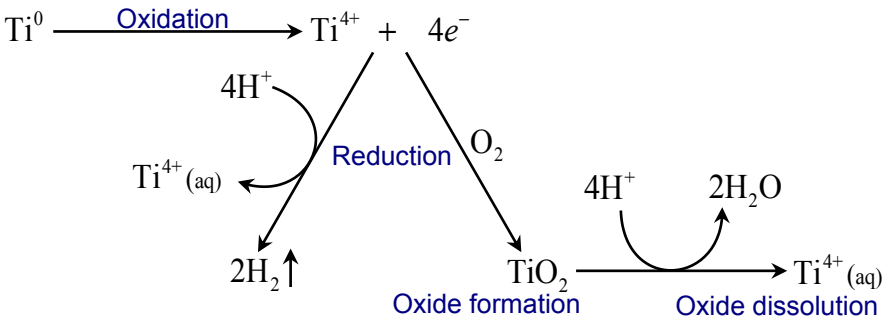

Figure 20: Possible pathways of titanium in acidic solution.

In the distant past, linear and Tafel data plots were printed out on paper while the slope, line fits and calculations were all performed manually by pencil and straight edge. The polarization software suites available today greatly facilitate the completion of these operations usually by default. For the PAR Powersuite application, the user can select specific regions for analysis while the program statistically fits the linear and Tafel data to the Stern-Geary model. In the process, the red beta lines are overlaid on the data plot, and then a summary is presented of the calculated results which typically include E_{Cor}, I_{Cor}, R_{Cor} and k_{Cor} in mil/year. One can also perform the curve fits, associated statistics and calculations by hand if so desired. Due to the developmental approach taken during this project as well as for verification purposes, the majority of software-generated results for this study were supplemented with manual curve fits, special analysis and modified calculations in order to maintain data uniformity and to accommodate the determination of unique parameters not covered in the software.

4.3.6 Summary of Data Averages and Analysis for Linear Polarization

A combined summary of data averages for all the linear and Tafel polarization testing conducted during this project is provided in Table 9. Since the results obtained for the linear and Tafel analysis were very similar, it was decided to combine their averages and analytical results for expediency.

Table 9: Combined summary of Linear and Tafel data averages for both test solutions.

	Relative Nobility		Linear and Tafel Parameters					Steady State Oxidation Rates at E_{Cor}			
								Metal Recession		Oxide Growth	
PreTreat	E_{Cor} (mV_{AgCl})	S_{Cor} (%)	R_{Cor} ($M\Omega/cm^2$)	I_{Cor} (nA/cm^2)	β_A (mV/dec)	β_C (mV/dec)	PreTreat	(Å/day)	(mil/year)	(Å/day)	(mil/year)
Titanium CP	69.1	0.31%	0.27	467	257	187	Cronidur 30	63.2	0.091	320	0.459
Titanium 6-4 LI	64.8	0.34%	0.15	413	205	143	Hastelloy C-276	67.8	0.097	345	0.496
Titanium 6Al-4V	63.9	0.34%	0.10	444	280	187	Inconel 625	74.9	0.108	395	0.567
Cronidur 30	17.3	4.56%	0.09	579	461	81	Titanium 6-4 LI	94.0	0.135	271	0.389
Inconel 625	15.7	2.93%	0.11	517	225	43	Titanium 6Al-4V	100.7	0.145	290	0.417
Hastelloy C-276	14.0	3.64%	0.08	498	456	96	Titanium CP	116.7	0.168	304	0.437
Brine							**Brine**				
Titanium CP	80.2	0.30%	0.70	388	1044	207	Cronidur 30	40.0	0.058	203	0.291
Titanium 6-4 LI	77.5	0.34%	0.29	345	254	192	Inconel 625	41.1	0.059	216	0.311
Titanium 6Al-4V	68.4	0.34%	0.60	419	241	185	Hastelloy C-276	48.6	0.070	248	0.356
Hastelloy C-276	23.1	3.62%	0.17	317	1459	229	Titanium 6Al-4V	69.3	0.100	200	0.287
Inconel 625	22.7	2.92%	0.18	446	830	216	Titanium 6-4 LI	78.5	0.113	226	0.325
Cronidur 30	20.9	4.56%	0.34	315	746	178	Titanium CP	89.2	0.128	232	0.334

The E_{Cor} rate values in Table 9 are reflective of the OCP values at steady state. At E_{Cor}, the rate of metal recession for these metals in these solutions is on the order 40-120 Å/day (0.6-0.17 mil/year) while the rate of oxide growth and oxide dissolution is on the order of 200-400 Å/day (0.3-0.5 mil/year). General recession and oxidation rates for the titanium candidates were apparently higher than those for the other metals. This may be indicative of the fact that exposed titanium is more active than the heavier chromium or nickel-rich alloys. Special methods for estimating susceptibilities (signified by S_{Cor} in Table 9) were derived by utilizing thermodynamic concepts from the Nernst equation and are covered in Section 5.4. Apparent nobilities and susceptibilities for the six metals obtained during Linear/Tafel analysis were also reflective of the results obtained during the OCP test runs.

Undoubtedly, these rates are higher than those that would be obtained under the same conditions in seawater. In any event, for the test solutions of interest here, none of the subject test metals showed any signs of corrosion, anomalous surface growth or surface degradation after linear/Tafel polarization. Tafel polarization of more active metals such as the aluminum alloys and low alloy steels can sometimes impart visible damage to the surface. Penetration/recession into such active metals can proceed unabated since the corrosive oxide products provide little protection. Recession rates and depths for these susceptible metals are expected to be much greater than the noble metals under study. In seawater, destructive recession rates for low alloy steels and many of the aluminum alloys can be 5-10 mpy and higher (1 mpy ≈ 695 Å/day). For iron, these rates would exponentially rise as pH levels drop below about 4 and then completely take off around 3 as the metal rapidly dissolves, and rates would double as the temperature is increased from ambient to about 50-60°F. Comparatively, recession rates for the subject metals in this study are many times lower (even in a more active environment), and their passive oxides provide a phenomenal level of protection against sustained recession.

When these six noble passivating metals are at E_{Cor}, the rates of oxidation k_1 and reduction k_2 are conversely equal and constant but nonzero, and the rates of oxide growth and dissolution are also constant and equal. For example, in analogy to Figures 12 and 20, reactions involving the nickel component in Inconel and Hastelloy could be represented as . . .

$$Ni^0 \underset{}{\overset{k_1}{\rightleftharpoons}} Ni^{2+} + 2e^- \underset{}{\overset{2H^+ \; k_2}{\rightleftharpoons}} Ni^{2+}(aq) + H_2\uparrow$$

$$Ni^0 \underset{}{\overset{k_{Met}}{\rightleftharpoons}} Ni^{2+} + 2e^- \underset{}{\overset{\frac{1}{2}O_2 \; k_{Ox}}{\rightleftharpoons}} NiO \underset{}{\overset{2H^+ \; k_{Dis}}{\rightleftharpoons}} Ni^{2+} + H_2O$$

where at E_{Cor}, $k_1 = k_2$ = constant, $k_{Ox} = k_{Dis} = ck_{Met}$ = constant, and $c = \rho_{Met} W_{Eq,Ox} / \rho_{Ox} / W_{Eq,Met}$

Below E_{Cor}, the cathodic reaction rate is greater than the anodic rate, $k_2 > k_1$ where the dissolution rate dominates over any tendencies for metal recession and oxide generation, $k_{Dis} > k_{Met}, k_{Ox}$. As iterated earlier, the oxide dissolves under highly cathodic conditions. Above E_{Cor}, the anodic reaction rate is greater than the cathodic rate, $k_1 > k_2$, while the mutual rates for metal recession and oxide growth preside over the dissolution rate, $k_{Met}, k_{Ox} > k_{Dis}$. Under higher anodic conditions, active metal recession and passive oxide growth will overwhelm the process of dissolution.

4.4 Cyclic Polarization

4.4.1 Analysis of Cyclic Polarization Curves

Information pertaining to general corrosion and oxidation is obtained during the linear methods previously covered. While general corrosion/oxidation aspects can be acquired or substantiated during subsequent cyclic test runs, the most valuable information obtained is related to the tendency for corrosive pitting (and possibly crevicing under certain test configurations). In general, cyclic polarization is a destructive test as the surface of the sample is disturbed, sometimes with visible results. Most cyclic polarization test runs start out by applying a linearly increasing voltage ramp, beginning in the negative cathodic area, increasing through the Tafel region and then up into the anodic region, beyond the passivation zone and oxide breakdown point to a pre-selected potential where the voltage scan reverses and ramps back down toward the cathodic region. A hysteresis loop is usually generated. Several key points and regions are realized in the cyclic scans conducted on the subject metals.

(a) E_{Cor1} – As covered earlier. This is the primary polarity switching point from cathode to anode when passivation just begins during the up-scan. Pertains to general corrosion/passivation.

(b) The Tafel region – As covered earlier, E_{Cor1} and I_{Cor} are represented by the intersection of the Tafel beta line slopes pertaining to possible general corrosion/oxidation events.

(c) E_{Pas} – The primary passivation potential taken at the apex (the tangent) of this curve section also provides I_{Pas} which represents the maximum passivation potential and passivation rate attained before oxide growth begins to end or level off.

(d) The passive region or plateau – The passive oxide may strengthen a little after passing through E_{Pas} but then begins to weaken with possible metastable pitting occurring as the breakdown point is approached.

(e) E_{Brk} – The oxide breakdown potential is analogous to the dielectric strength of the oxide where the oxide structure may be breached followed by possible pitting initiation. With the exception of a few samples that were intentionally tested under extreme test conditions, most of the metals in this study showed no signs of pitting into the base metal during these tests. Behavior of the plot just after E_{Brk} may be indicative of the metal's susceptibility to pitting initiation.

(f) E_{Ver} – The scan reversal potential or so-called vertex is the user-selected point where the increasing voltage ramp reverses and begins to decrease back down the same scan ramp (1-2mV/s). Behavior of the plot just after E_{Ver} can provide unique insight regarding the metal's repassivation capability to provide protection against sustained pitting.

(g) The repassivation region provides further information regarding the repassivation process and the degree of protection attainable. Even though the same linear potential ramp was applied for the upward and downward scans, hysteresis was considerable for these metals after E_{Ver}. The direction and area of the hysteresis loop is indicative of the strength or robustness of the metal's self-protection mechanism against sustained pitting. With the exception of Cronidur, the instant E_{Ver} is passed, any signs of possible pit initiation immediately vanish as the metal fervently begins repassivation and oxide regeneration at the maximum repassivation rate.

(h) E_{ReP} – The repassivation potential is marked at the apex of the return curve where repassivation is winding down as the recovery process is near completion. Usually visible only in a normal plot of the data. Techniques to surmise maximum rates for pitting penetration and repassivation growth will be discussed shortly.

(i) E_{Cor2} – This is the polarity switching point from anode back to cathode during the down-scan after repassivation is complete. Pertains to general corrosion/oxidation and general repassivation.

Cyclic plots and graphical analysis for one of the Hastelloy and Cronidur samples are given in Figures 21 and 22 as examples to help illustrate some of these parameters and concepts.

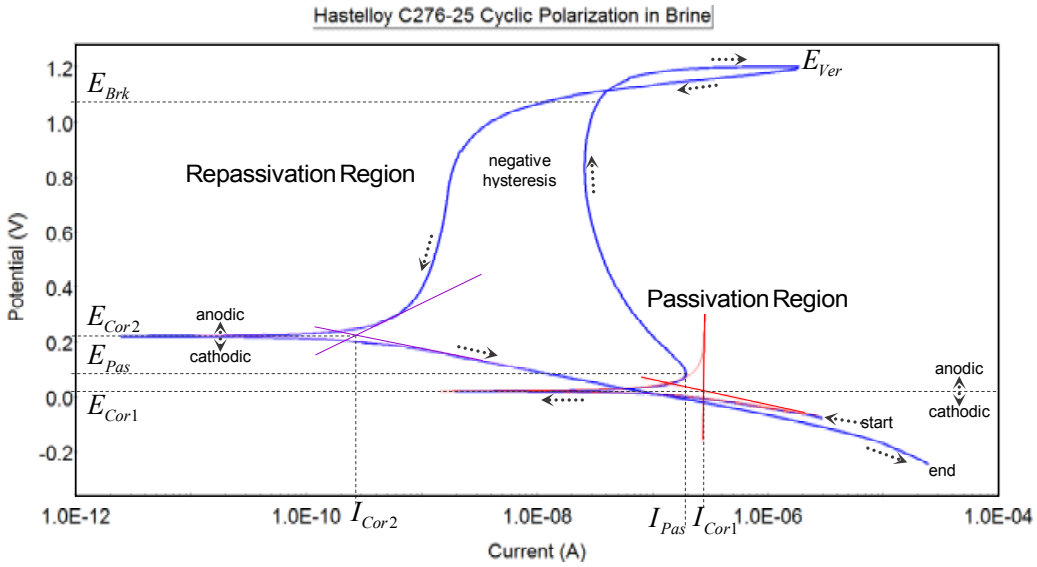

Figure 21: Cyclic polarization test results and analysis for Hastelloy in brine.

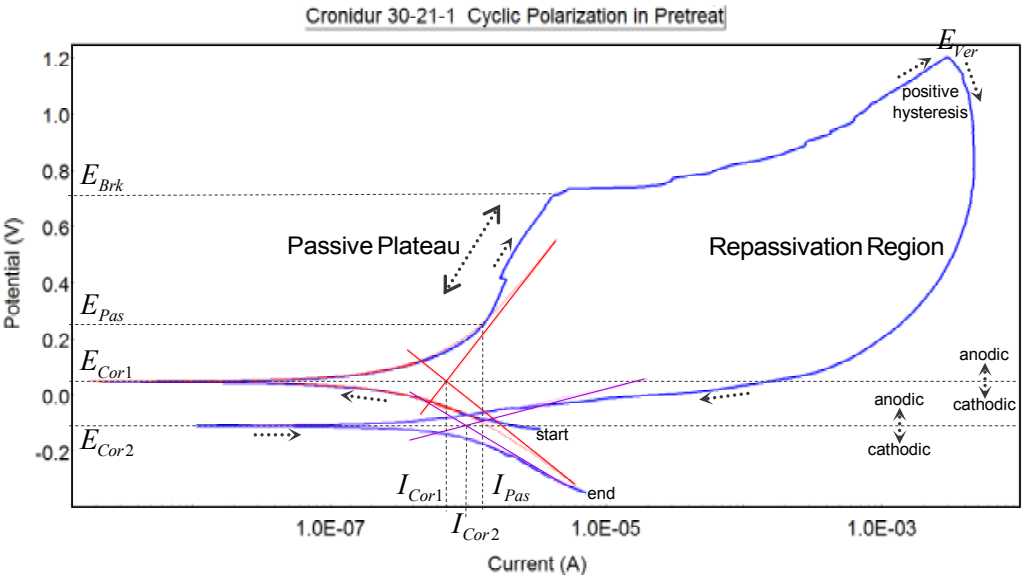

Figure 22: Cyclic polarization test results and analysis for Cronidur in pretreat

The cyclic curve form displayed for Hastelloy in Figure 21 is reflective of most of the plots for the other Hastelloy samples a well as most the Inconel samples in both solutions. It also bears significant similarity to most of the Titanium plots. While the Cronidur plots contain the same parameters, regions and points, the curve shapes and ranges were notably different than the other metals. Approaching E_{Brk}, metastable pitting becomes possible. Between E_{Brk} and E_{Ver}, the oxide might be compromised and active pitting could be taking place. After passing E_{Ver}, the oxide either (a) repairs itself very rapidly and all vestiges of pitting completely vanish or (b) the oxide repairs itself slowly while sustained (or metastable) pitting attempts to survive. Case (a) describes all the Inconel, Hastelloy and Titanium samples where the slope of the curve following E_{Ver} immediately rebounds as the current decreases sharply and the repassivation forces completely overwhelm any possible traces of pitting that may have existed. This also results in negative hysteresis (since the down-ramp data is now tracking behind the up ramp).

On the other hand with case (b), there is a forward component observed in the Cronidur plot just after E_{Ver} is passed which implies that pitting may still be occurring after the voltage reversal point. This is depicted in Figure 22. In general, E_{Ver} is likened to a relief point in the voltage-driven breakdown process where a robust self-repairing mechanism has the opportunity to swiftly rebuild broken structural links in the oxide lattice, but Cronidur shows weaknesses in this aspect with a very high positive hysteresis area. Thus, negative hysteresis implies strong repassivation protection forces while positive hysteresis is indicative of poor pitting protection. This is one of the primary differences between Cronidur and the other metals. There are other disparities.

Note: Many of the techniques and concepts introduced in this section and the following sections were developed independently as extensions to ASTM G102 specifically for this study and may be considered as special approaches for evaluating and characterizing corrosion, pitting and oxidation phenomena. While these techniques appeared to work well for this study, no guarantee is given regarding their validity or accuracy in other applications.

The higher the potential required to locally damage or breakdown the passive oxide E_{Brk}, the higher the resistance to pitting. Consider the potential height of E_{Brk}, or rather the potential difference between E_{Brk} and the primary passivation potential E_{Pas} in Figures 21 and 22. For the Hastelloy sample, the difference $E_{Brk} - E_{Pas}$ is over one volt, while this same distance on the Cronidur plot is about a half a volt. In the pretreat test solution, this potential ranged from about 800-900mV for the Inconel, Hastelloy and Cronidur samples. In the Brine test solution, a similar range was obtained for the Inconel and Hastelloy samples but the Cronidur samples were lower, ranging from about 400-700mV. The Titanium materials ranged from about 1300-1500mV in both solutions. These results tend to support the evidence that Cronidur is relatively more susceptible to pitting in the brine solution than the other metals and that all the Titanium metals are superior in both solutions. The potential difference $E_{Brk} - E_{Pas}$ provides insight regarding the tendency of pits to form that is, the susceptibility of pitting initiation which is a unique characteristic for each of these metals. Special methods for estimating initiation and sustainment susceptibilities are covered in Section 5.4.

Now, examine the relative locations of E_{Cor1} and E_{Cor2} with respect to the potential axis in Figures 21 and 22. Note that E_{Cor1} (same as E_{Cor} in previous discussions) and E_{Cor2} are both dominated by general corrosion effects, but E_{Cor2} may also be influenced by events associated with pitting which can lead to a general repassivation regeneration process terminating at E_{Cor2}. Also, recall that E_{Cor1} marks the beginning of the primary passivation process when the sample switches from cathode to anode and oxide growth commences in order to protect it from the solution, while E_{Cor2} marks the end of

the repassivation growth process after the oxide has completed all the rebuilding and repair steps, switching from anode back to cathode. The higher that E_{Cor2} is on the potential axis (and the closer it is to E_{Brk}), the sooner the oxide regeneration process is completed and the more resistant the base metal becomes to general and pitting corrosion, even though it is adequately protected well before reaching E_{Cor2}. Nevertheless, note that for the Hastelloy plot, E_{Cor2} is higher than E_{Cor1} while on the Cronidur scan, E_{Cor2} is lower than E_{Cor1}. Indeed, for all the Inconel, Hastelloy and Titanium samples, E_{Cor2} is above E_{Cor1}, but for all the Cronidur scans, E_{Cor2} is below E_{Cor1} in both solutions. For most of the Titanium samples in this study, E_{Cor2} was very high and very close to E_{Brk}, further supporting the premise that Titanium and its alloys are extremely resistance to both pitting and general corrosion.

4.4.2 The General Recovery Ratio (GRR)

A relative and simple indicator of general corrosion recovery could be suggested by comparing the rates of metal recession or oxide generation corresponding to the two general corrosion inflection points at E_{Cor1} and E_{Cor2}. During a cyclic polarization test, the General Recovery Ratio, *GRR* can be defined as the ratio of the corrosion rate at E_{Cor1} (the primary corrosion inflection point) to the corrosion rate at E_{Cor2} (the secondary or recovery inflection point after repassivation is complete). That is . . .

$$GRR = \frac{I_{Cor1}}{I_{Cor2}} = \frac{k_{Met,Cor1}}{k_{Met,Cor2}} = \frac{k_{Ox,Cor1}}{k_{Ox,Cor2}}$$

The *GRR* reflects how well the metal might 'recover' to protect itself via general repassivation, repair or regeneration after the oxide has been compromised and general corrosion has initiated. All the metals in this study indicated reduced corrosion rates after repassivation (lower I_{Cor2} values), inferring that the newly formed oxide layer is actually better than the original passivation layer (this is somewhat analogous to anodizing). Of the Titanium candidates, the CP grade indicated the best *GRR* protection with values in the double digits while averages for the other grades were in the single digits. Values for Cronidur were comparable to the Titanium samples (even though Cronidur shows pitting weaknesses, its general protective properties are excellent). Interestingly, *GRR* averages for the Inconel and Hastelloy samples were all over 500 indicating very robust repassivation recovery forces for these metals. It could be inferred that other metals with a $GRR < 1$ would exhibit poor recovery protection in the event general corrosion activities were initiated in a given environment. However, for all six of the metals in this study, the results clearly reflect very strong general corrosion self-protection mechanisms.

The potential difference $E_{Brk} - E_{ReP}$ provides insight regarding the tendency of pits to continue growing once they have formed, that is, the susceptibility of pitting sustainment which is a unique characteristic for each of these metals (Section 5.4). The primary repassivation potential E_{ReP} as well as the maximum values for the pitting current and the repassivation current cannot be obtained objectively using log plots. While the log plots are effective in providing values for E_{Cor1}, I_{Cor1}, E_{Cor2} and I_{Cor2}, the normal or linear plots often reveal more precise values of E_{Brk}, E_{ReP} and the associated currents. Since the data in a log plot is skewed, correct identification of these parameters is virtually impossible, while evaluation of the normal plot leads to precision estimates. Interpretation of E_{Brk} may also be improved using the normal plot. Utilizing a special approach employed for this study, unique parameters were extracted from the normal plots of cyclic polarization scans reflecting the maximum attainable pitting (metal recession) rate $I_{Pit,Max}$ (written simply as I_{Pit} for brevity) and the maximum possible repassivation (oxide regeneration) rate $I_{ReP,Max}$ (written simply as I_{ReP}).

Behavior of the curve in the E_{Brk}-E_{Ver}-E_{ReP} region is critical. If the experimental scan is tailored appropriately so that the E_{Brk} region is captured well below E_{Ver}, the net current along the slopes preceding and following E_{Ver} can be evaluated. Along the slope preceding E_{Ver}, the current is dominated by pitting (metal recession) with a resistance R_{Pit}, while along the slope following E_{Ver}, the current is dominated by repassivation (oxide regeneration) with a resistance R_{ReP}. Since E_{Brk} is associated with R_{Pit} and E_{ReP} is associated with R_{ReP}, the following rudimentary expressions can be suggested . . .

$$\left|\frac{dE}{dI}\right|_{Pit} \sim R_{Pit} \sim \frac{E_{Brk}}{I_{Pit}} \qquad \text{and} \qquad \left|\frac{dE}{dI}\right|_{ReP} \sim R_{ReP} \sim \frac{E_{ReP}}{I_{ReP}}$$

These ideas are illustrated in Figure 23 for one of the Inconel samples showing how pinpoint values for E_{Pit}, and E_{ReP} can be acquired along with quantitative representations for the maximum pitting rate and the maximum repassivation rate via slope and tangent analysis of the normal plot.

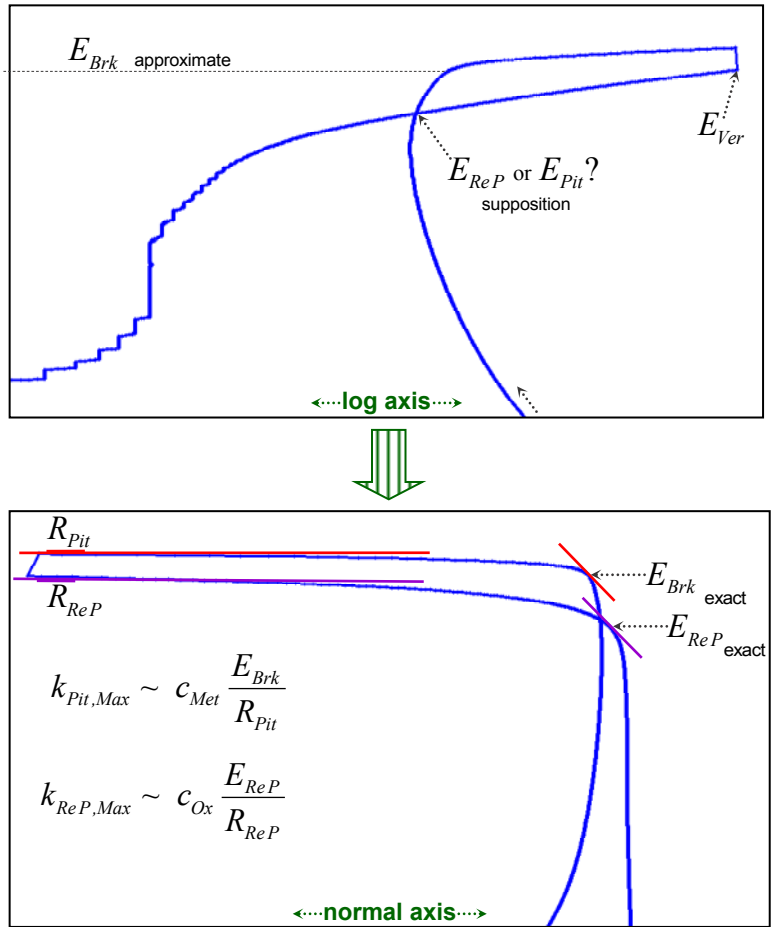

Figure 23: Method for evaluation of critical pitting and repassivation parameters using semi-log and normal plots.

Note that the tangent point for E_{ReP} is not visibly apparent on the log plot. Also, the intersection of the scan lines on a log plot are often mistaken to represent the pitting or repassivation current. For most of the Cronidur samples, the maximum pitting rate exceeded the maximum repassivation rate, but for all the other metals, any possible traces of pitting were completely subdued by the oxide regeneration process. This implies that pitting into the base metal of Cronidur could conceivably be the net result under extreme environmental conditions. As revealed in Section 3.2,2, pitting was visibly evident in most of the Cronidur samples after cyclic polarization. The extent and depth of pits in Cronidur samples tested in brine solution were well pronounce. Such results may be related to the repassivation-pitting rate ratio which is a direct result of the extremely low repassivation potential E_{ReP} that was characteristic of Cronidur scans in both solutions. This calls for introduction of another concept . . . the Pitting Recovery Ratio.

4.4.3 The Pitting Recovery Ratio (PRR)

After acquiring 'apples-to-apples' values for the rates of pitting vs. repassivation, a different perspective is achieved regarding a passive metal's protection mechanism against pitting via self-repair and oxide regeneration. For instance, elucidation of the maximum obtainable rates corresponding to these two opposing processes permits development of techniques for projecting long term pitting rates and the definition of special factors for gauging the effectiveness of the recovery process. On that note, consider another ratio of great importance that can aid in the evaluation of pitting protection properties specific to any metal . . . the Pitting Recovery Ratio (*PRR*). Generally, 'recovery' ratios pertain to situations where pitting has already initiated and imply how well the re-passivation process protects the metal against continued pitting effects during the recovery process. While the *GRR* relates primarily to general corrosion and general repassivation protection, the *PRR* indicates how well the metal might protect itself via localized repassivation/repair after the oxide has been compromised and pit growth has already initiated. It is defined simply as the ratio of the maximum rate of repassivation k_{ReP} (oxide regeneration) following E_{Ver} to the maximum rate of pitting recession into the surface k_{Pit} prior to E_{Ver}, that is . . .

$$PRR = \frac{k_{ReP}}{k_{Pit}} = \frac{I_{ReP}}{I_{Pit}}\left(\frac{\rho_{Met} W_{Eq,Ox}}{\rho_{Ox} W_{Eq,Met}}\right)$$

. . . where I_{Pit} is the minimum slope (maximum value) indicated after passing E_{Brk} or prior to E_{Ver} on the cyclic polarization curve while I_{ReP} is the minimum slope (maximum value) indicated after passing E_{Ver}.

In both solutions, *PPR* values for the Titanium samples ranged from 10-20 while those for the Inconel and Hastelloy samples ranged from 2-3, and *PRR* values for the Cronidur samples were all less than one. The higher the *PRR* value, the greater the protection against pitting while the lower the *PRR* value, the lower the pitting protection. Thus when $PPR > 1$, pitting is unlikely as the oxide repassivation rate overrides the surface pitting recession rate, and when $PRR < 1$, the possibility of sustained pitting is inferred. In the event that $PPR = 1$, a condition of metastable pitting would be implied. The visible results (Figures 6 and 7) appear to match the theory quite well as indicated in Table 10.

4.4.4 Summary of Data Averages and Analysis for Cyclic Polarization

Table 10 provides a summary of the test averages, analysis and estimation results as described in the foregoing discussion regarding the cyclic polarization test runs conducted and pitting information developed for the six metal candidates in this study in the two subject test solutions.

Table 10: Summary of results and averages for cyclic polarization and related pitting phenomena.

	Potentials & Rates Associated With Pitting Corrosion & Pitting Protection					Indications & Probabilities Associated With Pitting Corrosion & Pitting Protection				
PreTreat	**Max Passivate Potential** (mV_{AgCl})	**Oxide Breakdwn Potential** (mV_{AgCl})	**Max Repass Potential** (mV_{AgCl})	**Max Pitting Rate** (mil/yr)	**Max Repass Rate** (mil/yr)	**Area of Hysteresis Loop** (mV-A)	**Pitting Recovery Ratio** (k_{ReP}/k_{Pit})	**General Recovery Ratio** (I_{Cor1}/I_{Cor2})	**Susceptibility for Pitting Initiation** $f(E_{Brk}-E_{Pas})$	**Susceptibility for Pitting Sustainment** $f(E_{Brk}-E_{ReP})$
Titanium CP	839	2315	1904	0.18	1.35	-0.75	7.27	33.6	0.62%	0.37%
Titanium 6-4 LI	798	2287	1749	0.20	1.42	-1.01	6.98	6.29	0.75%	0.38%
Titanium 6Al-4V	785	2157	1733	0.27	1.78	-2.48	6.61	8.42	0.79%	0.38%
Inconel 625	129	996	911	2.47	5.67	-0.33	2.36	693	9.02%	1.58%
Hastelloy C-276	146	950	809	2.08	4.39	-0.23	2.78	758	10.4%	0.76%
Cronidur 30	150	653	196	5.99	2.22	+22.6	0.47	1.33	15.9%	11.3%
Brine										
Titanium CP	960	2303	1729	0.33	1.80	-0.48	5.43	19.5	0.74%	0.40%
Titanium 6Al-4V	982	2302	1671	0.33	2.37	-3.26	6.73	5.43	0.74%	0.70%
Titanium 6-4 LI	865	2179	1242	0.30	1.56	-2.95	7.26	4.15	0.84%	1.03%
Inconel 625	153	1046	858	3.19	8.22	-0.22	2.56	510	8.94%	0.43%
Hastelloy C-276	117	903	836	3.67	9.49	-0.17	2.62	697	10.5%	0.58%
Cronidur 30	141	766	261	13.7	2.77	+17.6	0.19	20.4	19.8%	8.53%
	E_{Pas}	E_{Brk}	E_{ReP}	k_{Pit}	k_{ReP}		*PRR*	*GRR*	S_{PiI}	S_{PiS}

Special methods for estimating susceptibilities are covered in Section 5.4 but it can be indicated here that the tendency for pitting initiation is dependent on the potential difference between E_{Brk} and E_{Pas} while sustained pitting is reflected by the difference between E_{Brk} and E_{ReP}. As Table 10 reveals, relative to the other metals, the Titanium metals exhibit very high breakdown potentials and high passivation potentials (which leads to low susceptibilities for pitting initiation), and very high repassivation potentials (which leads to low susceptibilities for sustained pitting), as well as negative hysteresis areas and high pitting recovery ratios. In contrast, Cronidur exhibits high pitting susceptibilities, very high positive hysteresis areas and pitting recovery ratios that are less than one. According to these test results, the use of Cronidur could conceivably pose a risk for pitting initiation and sustainment under extreme field conditions. However, it should be reiterated that no pitting was visually observed on any of the metal candidates under evaluation in this study after wedge/sandwich crevice storage nor on any of the samples that underwent galvanic coupling evaluations.

It should be noted that the current corresponding directly with E_{Brk} can be identified as the 'metastable pitting current' where pitting (metal recession) and repassivation (oxide regeneration) may be occurring simultaneously at the same opposing rates. Unfortunately, a correct interpretation of pitting rates cannot be obtained from some exquisite point where the scan lines happen to intersect on a cyclic polarization plot. More importantly, there is no 'average' or 'stable' pitting rate and there is no single value that represents the pitting rate . . . pitting rates are always changing! A pitting rate life cycle goes from zero up a long ramp over time, through a momentary maximum, and then back down an even longer ramp to an asymptotic zero. In a cyclic run, pitting rates vary from a low metastable condition around E_{Brk} to a maximum rate somewhere from 0.05-0.5V beyond E_{Brk}. In real world situations, after pits have initiated and the conditions are favorable for continued (sustained) pitting, rates increase exponentially, reach a peak (that is, a maximum pitting rate $I_{Pit,Max}$) and then gradually diminish to zero as corrosion products fill the pit volume and diffusional blockage into the active pit area prevents further penetration. Section 5.3 describes a special approach for estimating or projecting variable long-term pitting rates and penetration depths based on actual field test results in correlation with cyclic polarization data.

For Cronidur, some pitting may be occurring after E_{Ver} is passed, before repassivation finally takes over. For all the other metals, repassivation appears to dominate the process almost the instant the voltage reversal takes place at E_{Ver}. The potential identified as E_{Brk} is sometimes referred to as the 'pitting' potential since the implication is that sustained pitting just begins to take effect beyond E_{Brk}. However, for the metals under study, pitting (irreversible penetration into the base metal) does not necessarily occur at or beyond E_{Brk} and the 'point or region of oxide breakdown' is deemed a more appropriate description. At the least, E_{Brk} represents the voltage where the oxide properties change substantially, such as *n-p* conductivity, bond rupture, lattice weakening, permeability/porosity expansion and/or mass flow deviations. The current corresponding directly with E_{ReP} represents a minimum repassivation rate just before repassivation is complete (prior to E_{Cor2}). Its significance in the evaluation of the corrosion and oxidation rates of interest to this discussion appears to be minimal at this time.

4.5 Galvanic Coupling Analysis

Galvanic interactions between dissimilar metals can cause voltage differences and current fluxuations that alter the anodic and cathodic behavior of the metals involved. One metal may become cathodic while the other becomes anodic or vice versa. When a passivating metal is placed in electrolytic contact to form a galvanic couple with another metal that is cathodic to it (that is, more noble), it becomes an anode and will tend to develop more oxide to protect itself (or enhance and strengthen the existing oxide layer). When a passive metal is galvanically connected with another metal that is anodic to it (less noble), it becomes a cathode and the oxide will begin dissolving, thinning out or stripping away because it is no longer needed for protection. If metal ions are available in the local solution whose reduction potentials are greater (less negative or more positive) than that of the couple, plating or metallization onto the cathode surface can occur. Again, examination of the exposed sample surfaces on all six metals evaluated in both test solutions revealed no signs pitting, recession, plating, surface growth, degradation, patterns, major discoloration or any other anomalies. Other than some minor staining from the brine solution, exposed surfaces for all six metals looked identical to the surfaces before testing.

When a passive metal with an air-formed oxide layer (the test metal) is placed into solution and allowed to interact galvanically with a second metal (the counter metal), two electrochemical processes occur simultaneously. The test metal attempts to attain its original or initial solution-driven open circuit potential E_{OCI} (covered earlier) and then it interacts with the other metal to reach a net galvanic couple open circuit potential E_{OCG}. If the two processes overlap sequentially, then the test metal first begins to attain its E_{OCI} followed by specific electrochemical reactions leading to attainment of the couple E_{OCG}. During both processes, chemical and physical changes take place to the inner barrier sublayer (the primary oxide protection layer) and the outer porous hydrated layer. The thicknesses of these two sublayers will increase or decrease in response to the E_{OCI} and E_{OCG} forces. Throughout the entire process, a measureable intrinsic current I_g above the original E_{OCI} exchange current is generated and can be monitored during the run.

In cases where the test metal is forced into a less noble (more anodic) state under the influence of the counter metal, current is directed into the sample while electrons are flowing outward (indicated by positive current values). In these situations, the test metal is regenerating new oxide to 'keep up' with the cathodic influence of the counter metal in addition to the constant dissolution process due to acid hydrolysis from the test solution. This is analogous to the condition characterizing individual (uncoupled) metal samples during the original open circuit potential (OCP) test runs discussed earlier. In cases where the test metal becomes more noble (more cathodic), current is directed out of the sample while electrons flow inward (indicated by negative current values). In these situations, the test metal needs less oxide for protection, so solution-driven oxide dissolution dominates as the oxide layer diminishes. This is analogous to cathodic stripping. Due to the very close nobilities for the six test metals at the onset, all these changes are expected to be relatively small with larger changes occurring between less compatible metals and smaller changes between more compatible metals.

Recall from Section 4.2 that when the current increases, more electrons flow, implying that the nonconductive/semiconductive barrier sublayer is decreasing in thickness and vice versa. Also, when the potential increases, the capacitance decreases, indicating that the bulk electrical double layer (EDL) is spreading out as the conductive porous layer increases in thickness, and vice versa. When a net galvanic steady state is attained at E_{OCG}, I_g indicates either the steady state oxide regeneration rate corresponding to increases in barrier oxide thickness due to new growth or steady state decreases in barrier thickness due to stripping. The degree of change in nobility or the nobility shift can be indicated simply by $(E_{OCI} - E_{OCG})/E_{OCI}$. Figures 24 and 25 depict early portions of the scans evaluated respectively for an Inconel/Hastelloy couple (similar metals with minor differences) and a Titanium/Hastelloy couple (slightly dissimilar metals with more significant differences).

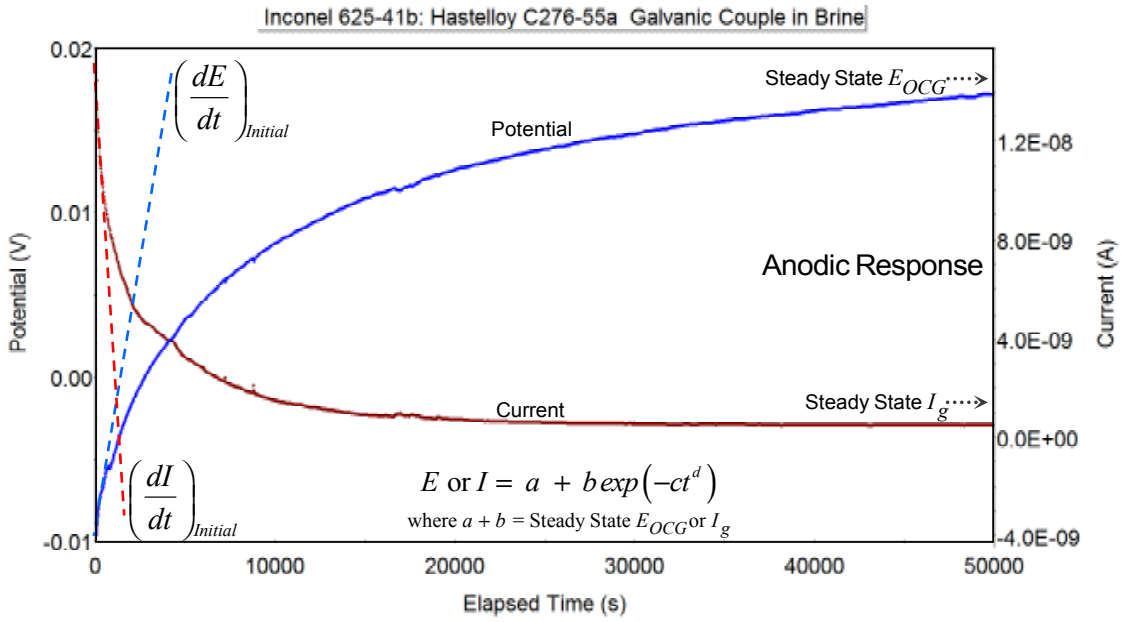

Figure 24: Galvanic open circuit scan for one of the Inconel <–> Hastelloy couples in brine solution.

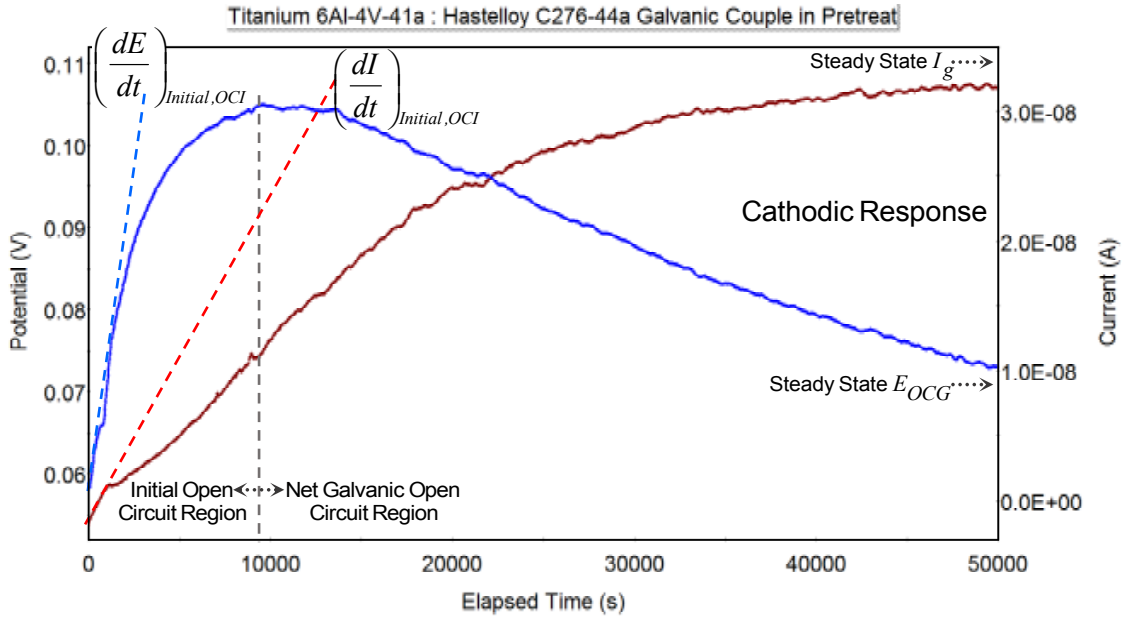

Figure 25: Galvanic open circuit scan for one of the Titanium <–> Hastelloy couples in pretreat solution.

Examine first, the curves in Figure 24 in which two closely matched metals interact. For this particular test run, the counter metal (Hastelloy) causes the Inconel sample to shift slightly in the anodic direction while overall, movement toward the original OCP or E_{OCI} and the net galvanic OCP E_{OCG} appear to coincide as the two processes take place simultaneously throughout. The porous layer increases in thickness (as reflected by the increasing potential) while the barrier layer also increases (indicated by the decreasing current) and then both reach their own plateau at a stable steady state (the final steady state E_{OCG} and I_g asymptotes are not visible at this magnification). The scan is very similar to the single metal OCP test runs covered earlier (Section 4.2). There are minimal galvanic interactions and the entire process is dominated by reactions associated with the Inconel sample while it moves toward its independent solution OCP almost as if the other metal were not present. At the onset and throughout the run, thickness rates increase for both the barrier and porous layers until the rates become constant when a net steady state OCP condition is attained. In this case, the net galvanic steady state attained is essentially equivalent to Inconel's independent, solution-driven open circuit steady state condition determined earlier.

In contrast, Figure 25 depicts a situation in which the nobility and the electrochemical differences between the interacting metals is slightly greater and where the Hastelloy is compelling (or allowing) the Titanium sample to become more cathodic. At the onset of the run, the process is influenced by the test metal's independent, solution-driven E_{OCI} field with a corresponding increase in the porous layer thickness. At some point, the process becomes dominated by E_{OCG} forces which encourages dissolution of the porous layer until the net E_{OCG} steady state is attained. Galvanic interactions play a role throughout the entire process as the barrier layer thickness continually decreases until a steady state I_g is achieved. Both sublayers begin to thin-out at a constant rate as the net steady state is attained.

In either case, only changes in barrier oxide growth rate can actually be estimated (from the current) since quantitative correlations between rate values and E are not fully understood at this time. Furthermore, appropriate values for the densities and equivalent weights of the respective porous oxide/hydroxide phases would be difficult to ascertain. Recall that the precipitated porous layer is a highly conductive and porous hydrated form of the barrier layer with a compositional make-up similar to that of the barrier except for the high water content. In addition, while the barrier layer is a hard, relatively dense ceramic, the porous layer is relatively soft, almost gelatinous with a much lower bulk density. Due to the hydrated complexes comprising the microstructure of the porous layer, its skeletal density is also expected to be lower than that of the oxide barrier layer.

Note that only a portion of the early scan runs are depicted in Figures 24 and 25 covering the first 14 hours. Most scans took over 36 hours to reach a plateau of one or both of the variables while some scans would have taken up to 7-10 days to attain a true steady state. As it was with the original OCP single metal test runs, curve-fitting techniques were employed to ascertain the most probable steady state values. Also, not all coupling curve forms for the six metals were as ordered as those shown in Figures 24 and 25 and most of the TiX/TiY scans were noisy and erratic, providing only long term steady state values for tabulation. While all these same features were charted with all the scans, the neatness of these two test runs helps to exemplify the key points of importance here. In all, there were several hundred coupling tests conducted and obviously, not all of the data can be presented here. Tables 11 and 12 provide the averages, summaries and associated estimates covering all the galvanic coupling tests conducted on the six metals in both test solutions under study.

Table 11: Summary of results and averages for galvanic coupling test runs in pretreat solution.

Pretreat	Potential Changes and Susceptibility Increases Relative to OCP Steady State (SS)			Oxidation Rate Changes at Couple SS Relative to OCP SS		Stabilization Period
	Steady State Potential (mV_{AgCl})	Susceptibility Increase (%)	Nobility Change in Test Metal	Recession Rate Increase (Å/day)	Oxide Growth Rate Change (Å/day)	~90% of Couple SS (hours)
Inconel 625 Couples	Original (Independent) OCP for Inconel 625 in Brine = 23.4 mV					
Hastelloy C276	21.7	------	8% Cathodic	------	-3.75	19
Titanium CP	67.0	0.349%	186% Anodic	3.08	16.2	11
Titanium 6-4	72.0	0.389%	207% Anodic	5.92	31.2	14
Titanium LI	84.7	0.490%	261% Anodic	7.14	37.6	14
Cronidur 30	28.0	0.037%	19% Anodic	1.42	7.49	8
Hastelloy C276 Couples	Original (Independent) OCP for Hastelloy C276 in Brine = 18.7 mV					
Inconel 625	19.7	0.009%	5% Anodic	0.50	2.46	8
Titanium CP	61.3	0.372%	228% Anodic	3.87	19.0	5
Titanium 6-4	55.8	0.324%	198% Anodic	6.46	31.8	9
Titanium LI	67.1	0.422%	259% Anodic	6.68	32.9	8
Cronidur 30	16.2	------	14% Cathodic	------	-3.92	5
Titanium CP Couples	Original (Independent) OCP for Titanium CP in Brine = 93.9 mV					
Inconel 625	70.3	------	25% Cathodic	------	-7.25	7
Hastelloy C276	33.3	------	65% Cathodic	------	-9.45	8
Titanium 6-4	98.7	0.004%	5% Anodic	0.87	2.26	15
Titanium LI	83.0	------	12% Cathodic	------	-3.32	15
Cronidur 30	60.7	------	35% Cathodic	------	-5.68	8
Titanium 6-4 Couples	Original (Independent) OCP for Titanium 64 in Brine = 77.4 mV					
Inconel 625	61.0	------	21% Cathodic	------	-6.73	10
Hastelloy C276	59.7	------	23% Cathodic	------	-7.60	10
Titanium CP	72.5	------	6% Cathodic	------	-2.10	17
Titanium LI	83.0	0.006%	7% Anodic	0.81	2.32	18
Cronidur 30	55.3	------	28% Cathodic	------	-6.24	6
Titanium LI Couples	Original (Independent) OCP for Titanium LI in Brine = 80.8 mV					
Inconel 625	63.8	------	21% Cathodic	------	-11.7	15
Hastelloy C276	65.7	------	19% Cathodic	------	-13.3	10
Titanium CP	77.0	------	5% Cathodic	------	-1.29	10
Titanium 6-4	73.4	------	9% Cathodic	------	-2.07	14
Cronidur 30	42.5	------	47% Cathodic	------	-5.91	5
Cronidur 30 Couples	Original (Independent) OCP for Cronuidur 30 in Brine = 39.0 mV					
Inconel 625	35.1	------	10% Cathodic	------	-4.78	6
Hastelloy C276	35.8	------	8% Cathodic	------	-3.17	6
Titanium CP	73.3	0.464%	88% Anodic	3.27	16.6	4
Titanium 6-4	67.7	0.388%	74% Anodic	2.63	10.4	4
Titanium LI	75.0	0.487%	92% Anodic	5.26	26.6	3

Table 12: Summary of results and averages for galvanic coupling test runs in brine solution.

Brine	Potential Changes and Susceptibility Increases Relative to OCP Steady State (SS)			Oxidation Rate Changes at Couple SS Relative to OCP SS		Stabilization Period
	Steady State Potential (mV_{AgCl})	Susceptibility Increase (%)	Nobility Change in Test Metal	Recession Rate Increase (Å/day)	Oxide Growth Rate Change (Å/day)	~90% of Couple SS (hours)
Inconel 625 Couples	Original (Independent) OCP for Inconel 625 in Brine = 38.2 mV					
Hastelloy C276	38.4	0.002%	1% Anodic	0.12	0.65	15
Titanium CP	96.7	0.468%	153% Anodic	3.63	19.1	15
Titanium 6-4	92.3	0.433%	142% Anodic	5.22	27.5	17
Titanium LI	95.0	0.455%	149% Anodic	6.22	32.8	20
Cronidur 30	44.0	0.047%	15% Anodic	2.15	11.4	11
Hastelloy C276 Couples	Original (Independent) OCP for Hastelloy C276 in Brine = 32.3 mV					
Inconel 625	30.2	------	7% Cathodic	------	-3.09	10
Titanium CP	78.3	0.402%	142% Anodic	2.35	11.6	15
Titanium 6-4	98.3	0.576%	204% Anodic	5.82	28.7	16
Titanium LI	73.3	0.358%	127% Anodic	6.60	32.5	18
Cronidur 30	34.8	0.022%	8% Anodic	1.94	9.55	8
Titanium CP Couples	Original (Independent) OCP for Titanium CP in Brine = 104 mV					
Inconel 625	81.0	------	22% Cathodic	------	-6.68	16
Hastelloy C276	76.0	------	27% Cathodic	------	-7.21	10
Titanium 6-4	106.7	0.002%	2% Anodic	1.37	3.58	24
Titanium LI	112.0	0.007%	7% Anodic	1.47	3.83	27
Cronidur 30	72.9	------	30% Cathodic	------	-4.67	12
Titanium 6-4 Couples	Original (Independent) OCP for Titanium 64 in Brine = 95.2 mV					
Inconel 625	75.3	------	21% Cathodic	------	-6.28	15
Hastelloy C276	50.3	------	47% Cathodic	------	-8.04	17
Titanium CP	91.7	------	4% Cathodic	------	-4.40	22
Titanium LI	102.4	0.008%	8% Anodic	1.51	4.35	17
Cronidur 30	56.8	------	40% Cathodic	------	-9.93	13
Titanium LI Couples	Original (Independent) OCP for Titanium LI in Brine = 97.0 mV					
Inconel 625	59.3	------	39% Cathodic	------	-14.4	17
Hastelloy C276	73.7	------	24% Cathodic	------	-10.4	16
Titanium CP	92.0	------	5% Cathodic	------	-1.87	19
Titanium 6-4	85.7	------	12% Cathodic	------	-2.85	19
Cronidur 30	53.8	------	45% Cathodic	------	-9.85	7
Cronidur 30 Couples	Original (Independent) OCP for Cronuidur 30 in Brine = 46.5 mV					
Inconel 625	48.7	0.029%	5% Anodic	0.47	2.38	4
Hastelloy C276	44.9	------	3% Cathodic	------	-1.26	2
Titanium CP	85.7	0.529%	84% Anodic	2.44	12.4	9
Titanium 6-4	92.0	0.614%	98% Anodic	3.47	17.6	8
Titanium LI	94.3	0.646%	103% Anodic	4.21	21.3	16

While *dE*/*dt* and *dI*/*dt* are shown on the plots for illustrative purposes (following the treatment applied during the original OCP runs), all the values in these tables refer to the final or net galvanic steady state achieved and infer nothing about the path to that point (unfortunately, time constraints did not allow a more thorough analysis of the galvanic coupling data). In most cases, couples between metals which are similar, such as those involving Inconel, Hastelloy and Cronidur and particularly those between the Titanium metals themselves, exhibit minimal changes in nobility and susceptibility (relative to their independent OCP's). Couples between less similar metals, such as any of the Titanium grades with the other metals, lead to greater shifts in nobility. It is apparent that nobilities and susceptibilities for the Titanium metals are higher than the other metals as almost all couples involving a Titanium candidate result in the Titanium half becoming substantially more cathodic.

Cathodic shifts usually also result in less oxide needed for protection. As discussed earlier, cathodic rate changes (indicated in red) infer thinning or dissolution of some of the oxide layer as a result of the metal's enhanced state of stability. The values in Tables 11 and 12 reflect changes in oxide growth or dissolution in addition to or subtracted from the original steady values tabulated in Table 6, Section 3.2.3. An abbreviated form of Tables 11 and 12 was provided in Table 7, Section 3.2. Approximate time periods to reach the net steady state region were generally reduced from those associated with the original OCP test runs except for the Titanium metals in the brine solution. The specific factors associated with the longer stabilization times for Titanium are not understood at this time.

5. Supplemental Discussion and Special Topics

5.1 Atypical Results during Polarization Testing

Examples of Anomalies, Outliers and Extreme Test Conditions

In order to capture the breakdown region E_{Brk}, preselected cyclic polarization test parameters generally utilized reversal vertex points (E_{Ver}) of around 1.0-1.2 V for the Inconel, Hastelloy and Cronidur samples, and 2.0-2.5 V for all the Titanium metals. As noted earlier, during normal test conditions, there were a few irregularities or artifacts observed such as birefringent-like discolorations and powdery oxide/hydroxide precipitates which developed on the exposed surfaces while they were being rinsed with DI water. The effects usually became more pronounced as the samples continued to dry in air. Under abnormal test conditions, namely, high anodic vertex reversal points, low cathodic starting points and test repeats on the same area, a number of anomalies and degradative effects were observed on several of the Inconel, Hastelloy and Cronidur samples. Remarkably, all the Titanium materials appeared to be immune to the excessive test voltages. Similar to Titanium surfaces shown in Section 3.1 after long-term storage, several of the polarization test areas also exhibited the same type of superficial surface discolorations. However, no pitting, etching or metal degradation was observed in any of the Titanium samples from polarization testing as visually shown in Figure 26.

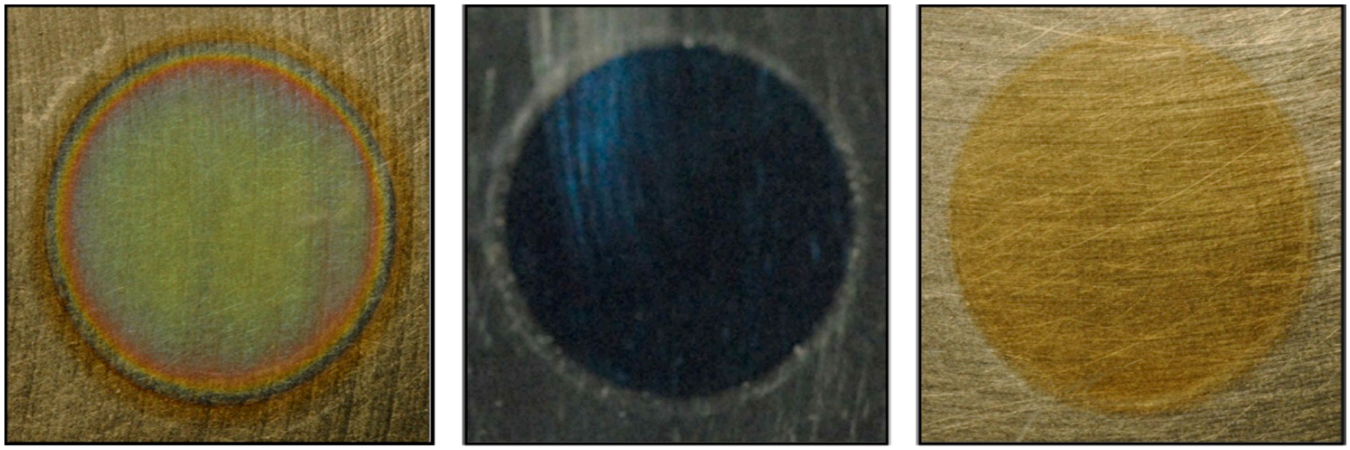

(a) (b) (c)

Figure 26: Photographic images of Titanium surfaces after application of normal and extreme test conditions.
(a) Titanium LI in Pretreat – No unusual test conditions or results were noted. The E_{Ver} was 2.2V. This result is believed to be atypical only in in appearance (colored oxide aberrations).
(b) Titanium 64 in Brine – No unusual test conditions or results were noted. The E_{Ver} was 2.4V. This result is believed to be atypical only in appearance (colored oxide aberrations).
(c) Titanium 64 in Brine – The E_{Ver} was 4.1V. The appearance (a slight tint) is typical of most Titanium test surfaces in spite of the high vertex potential applied during this particular sample.

Analysis of these surfaces via ESCA did not indicate any unusual contaminates or compositional irregularities associated with the discolorations. While there is no supporting evidence, it could be surmised that interactions with the test solution induced slight changes in certain lattice plane orientations within the oxide phase leading to reflection/diffraction effects that are purely optical in nature as the protective properties of the oxide are considered to be unaltered and completely intact.

When samples of Inconel, Hastelloy and Cronidur were subjected to excessive vertex potentials, destructive results were often obtained. Extreme voltages often led to pitting and general etching of the base metal except for the Titanium alloys. Some of these visual results are shown in Figure 27.

(a) (b) (c)

Figure 27: Photographic images of Cronidur, Inconel and Titanium when polarized under extreme voltages.

(a) Cronidur 30 in Pretreat – The E_{Ver} was 10V. This was an accidental test over-run. Extreme pitting and crevice damage is obvious. The test is probably not practical for serious evaluation due to the excessive E_{Ver} reached.
(b) Inconel 625 in Brine – The E_{Ver} was 4.5V. It can be seen that general etching into the base metal occurred with loss of oxide and loss of base metal. This effect is explored further in the next topic).
(c) Titanium CP in Pretreat – The E_{Ver} was 4.2V. Again, this appearance was typical of most Titanium samples. No base metal damage, pitting, abnormal surface growth or any other signs of degradation were noted on any of the Titanium samples, even when subjected to higher voltages.

When polarization test runs were conducted at extremely low cathodic starting points in the pretreat solution, several of the Inconel and Hastelloy sample areas appeared to experience excessive general recession into the base metal (not pitting). One of the Cronidur samples exhibited crevicing while very negative starting voltages did not seem to faze any of the Titanium metals. These types of effects were not noted in the brine, which indicates that they may have been heavily influenced by activation-controlled reaction sequences. Some of the pretreat results are portrayed in Figure 28.

(a) (b) (c)

Figure 28: Images of Hastelloy, Cronidur and Titanium when first subjected to low cathodic starting points.
(a) Hastelloy C276 in Pretreat – The starting potential was -0.75 V. There was significant general etching (recession). No actual pit cavities were observed. Green nickel oxide/hydroxide precipitate was apparent (after rinsing) with possible metallization (back-plating).
(b) Cronidur 30 in Pretreat – The starting potential was -0.75 V. Other than some apparent crevicing around the 1cm^2 O-ring boundary, no etching, recession or general damage was observed.
(c) Titanium 64 in Pretreat – The starting potential was -0.75 V. No signs of any damage to the oxide or base metal were observed. In addition, no discolorations were apparent on this sample.

The condition depicted in Figure 28(a) is believed be associated with the negative cathodic starting point where stripping of the air-formed oxide occurred followed by anodic regeneration of a new layer in the test solution which exacerbated separation of the nickel oxide (NiO) fraction toward the periphery of the layer. Acting as a barrier to electron flow and oxygen penetration, the NiO layer inhibited further passivation growth at the metal surface and eventually broke down at E_{Brk} allowing rapid general dissolution of the base metal before repassivation finally took over. The anomaly is explored in greater detail later on in Section 5.6.

5.2 Special Method for Determination of Electron Exchange Equivalents

Calculation of equivalent weights (W_{Eq}) for metals and alloys subjected to polarization measurements is required in order to determine corrosion/oxidation rates. Estimation of W_{Eq} values derived purely from base metal compositions is common practice. However, this may not be the best approach due to selective oxidation of the various alloy components. The concept of selective oxidation is mentioned in ASTM G102 but not elaborated on. In fact, there has been ample data published utilizing depth profiling via XPS (ESCA), SIMS and Auger analysis confirming that selective oxidation does indeed occur. Clearly, differences in oxidation susceptibilities between the alloying elements in a metal mixture are substantial, and the relative fractions of metals comprising cation sites within the oxide lattice are rarely the same as those in the base metal itself. In most cases, the ratio of metals in the substrate and the oxide phase is quite different. Composition of the oxide phase actually reveals more information regarding transfer equivalents than the base metal. Depth profiling results of the oxide layers for a couple of relevant alloys are given in Figure 29[11,12]. There are many more such analyses throughout the literature.

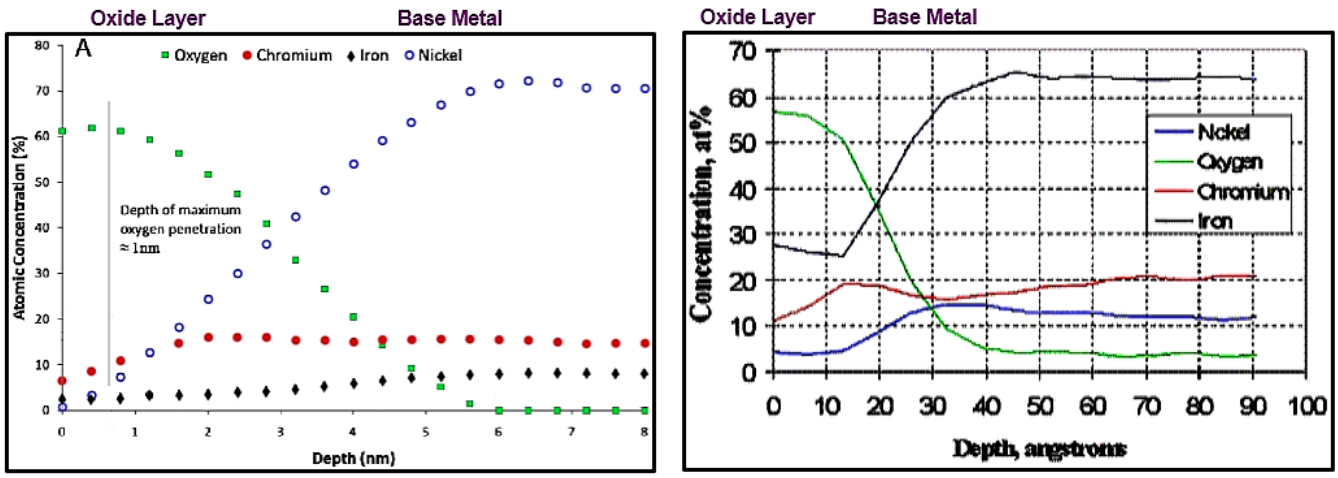

(a)
Inconel 700 passive oxide composition
Major base metal components:
Ni 46%, Cr 15%

(b)
SS 316 passive oxide composition
Major base metal components:
Fe 67%, Cr 17%, Ni 12%

Figure 29: (a) Depth profile of the passive layer on Inconel 700 contrasting the relative metallic concentrations in the base metal and the passive oxide[11]. (b) Depth profile of the passive layer on 316 stainless steel contrasting the relative metallic concentrations in the base metal and the passive oxide[12].

The intersection points between oxygen and the primary base metal constituent roughly indicate the center of the metal-to-oxide transition zone discussed earlier (Section 4.1). When comparing the percentages of metal components in the oxide (particularly the outer layers of the oxide) and deep within the base metal, it becomes obvious that, at least for passivating metals, estimations involving the transfer of electron equivalents during the oxidation process cannot be precisely represented by assuming that the base metal constituents adequately represent the metallic constituents in the oxide layer. Indeed, in

order to be specific, the net number of electrons extracted from the metal during the oxidation process must equal the net number of electrons consumed to form the oxide.

The following approach is proposed as an extension to ASTM G102. Reiterating, *the number of electrons extracted from the base metal during corrosive oxidation must equal (exactly) the number of electrons transferred to produce the alloy oxide* (in accordance with the conservation laws). Recognition of certain factors associated with the formation and composition of the oxidation product are key to estimating how many exchange electrons are actually generated. It is well known that the various metals in an alloy will oxidize at different rates according to their Gibbs free energy of formation. For example, Cr_2O_3, with a known formation energy of $\Delta G_f = -1053$ kJ/mol is five times more likely to form than NiO whose formation energy is documented to be $\Delta G_f = -212$ kJ/mol. The ΔG_f values clearly reflect this. Thus, we can propose that the Relative Ease of Oxide Formation according to the respective free energies of formation can be tabulated and ordered. For example . . .

$$Nb_2O_5 > Al_2O_3 > V_2O_3 > Cr_2O_3 > TiO_2 > Fe_2O_3 > MoO_3 > NiO$$

$$-1866 \quad -1582 \quad -1139 \quad -1053 \quad -890 \quad -742 \quad -668 \quad -212$$

The more negative the value, the more likely the oxide will form from its elements. A rather extensive database was compiled for this study by manually tabulating, averaging and evaluating established Handbook values and a multitude of historically documented experimental values obtained throughout the research industry to obtain average representative values for the formation energies, bulk densities, skeletal densities, dielectric constants, and various other required material properties for the composite oxides of interest in this study. There would be perhaps too many citations to note here and each input available was taken under consideration only as part of the surmised average, not utilized directly. While bulk compositions and electrochemical properties of the solution-formed oxides are different than the simpler passive layers that form in the air, metal contents are not all that different. Much research, supplementary estimations and educated guesswork were put into this effort in order to better understand, semi-quantify and ascertain the most likely composite oxide compositions and associated net property estimates expected for each of the six metals under evaluation in the subject test solutions. An example of one of the metals processed in this manner is illustrated in Figure 30

Hastelloy C276 Base Metal Wrought Composition, As-Received – In Air

	Raw Wt%	Est Wt%	Mol. Wt.	Atomic %	# Eq. e^-	$N_A e^-/g$
Ni	58.9%	59.3%	58.69	63.1%	0.67	1.14E-02
Cr	16.1%	16.2%	52.00	19.5%	2.72	5.24E-02
Mo	15.3%	15.4%	95.94	10.0%	0.55	5.75E-03
Fe	5.6%	5.6%	55.85	6.3%	0.39	6.92E-03
W	3.4%	3.4%	183.84	1.2%	0.10	5.18E-04

Base Metal Net Equivalents

99.3% 100.0% 100.0% 4.42 **13.0** g/mol

Net Equivalent Weight

Density 8.89 g/cc measured 8.77 g/cc estimated

Hastelloy C276 Composite Oxide Composition – In Acidic Test Solution

	Mole %		Atomic %	Less H_2O	# Eq. e^-	$N_A e^-/g$
Cr_2O_3	32%	Cr	21%	23%	2.031	1.34E-02
CrO_3	8.9%				0.558	5.58E-03
CrOOH	0.48%				0.015	1.79E-04
$CrOOH_2^+$	3.7%				0.118	1.37E-03
NiO	10.5%	Ni	6.8%	7.2%	0.221	2.96E-03
Ni_2O_3	4.1%				0.259	1.57E-03
NiOOH	0.60%				0.019	2.06E-04
$NiOOH_2^+$	5.3%				0.168	1.82E-03
MoO_3	6.6%	Mo	2.5%	2.6%	0.416	2.89E-03
MoO_2	0.53%	Protonated Oxide Surface			0.022	1.73E-04
$MoO_2(OH)_2$	0.20%				0.012	7.70E-05
$MoO(OH)_3^+$	1.6%				0.102	6.24E-04
Fe_2O_3	4.6%	Fe	3.5%	3.7%	0.289	1.81E-03
FeO	0.08%				0.002	2.28E-05
Fe_3O_4	0.94%				0.074	3.20E-04
FeOOH	0.08%				0.002	2.68E-05
$FeOOH_2^+$	0.60%				0.019	2.11E-04
WO_2	0.61%	W	0.47%	0.50%	0.026	1.18E-04
WO_3	0.87%				0.055	2.37E-04
$WO_2(OH)_2$	0.03%				0.002	6.59E-06
$WO(OH)_3^+$	0.21%				0.013	5.25E-05
					4.42	Total Metal Equivalents
H_2O	17%	O	65%	63%		
					4.42	Total Oxygen Equivalents
	100.00%		100.00%	100.00%	**29.8**	g/mol

Net Equivalent Weight

4.00 g/cc

estimated density

Figure 30: Average modelled composition and equivalents for the Hastelloy-oxide system in acidic solution.

Note in Figure 30 that the total number of electrons transferred from the base metal to the proposed metal oxide mixture are identical, as they should be. Identifying this value effectively permits estimation of the corresponding equivalent weights involved for both the base metal and its unique composite oxide. Also note that atomic concentrations of the metals comprising the oxide mixture are compliant with expectations via XPS, SIMS. Auger, etc… If the calculations were conducted utilizing strictly base metal compositions and the typical number of valence electrons one normally assumes, estimated equivalents weights for this metal would be on the order 23-25g/mol. However, the proposed approach provides equivalent weights which are unique to both the base metal and the composite oxide and which are connected by the net number of electron equivalents transferred between the two phases. This opens the door to more elaborate endeavors regarding oxide growth phenomena and passivation mechanics that are specific and exclusive to a given alloy under study. At present, estimation of electron and weight equivalents via oxide formation is complex, tedious and time-consuming. Even with the aid of Pourbaix and Ellingham diagrams, certain assumptions must be made and errors are likely without due diligence, but it is the correct way to determine the number of electrons transferred during the oxidation process.

Finally, note that most of the oxides of interest here are amphoteric in nature with pendant hydroxyl groups protruding along the surfaces prior to immersion into the acidic solution. Immediately upon immersion, these hydroxyl groups become protonated (positively charged) during formation of the electrical double layer (EDL). Then, as the EDL evolves, positive sites along the surfaces of the porous and barrier layers begin to attract anions that are present in the solution such as chlorides, sulfates, phosphates, carboxylates, urates, hydrolases, etc... These associations may comprise the outer Helmholtz plane or slip layer as steric hindrance increases diffusivity factors while disrupting access of reactants and products into the oxide/hydroxide macrostructures and ultimately, to the base metal. This activity plays a role in the actual levels of specific secondary and tertiary oxides and oxyhydroxides that initially develop from each metallic component as it interacts with the solution.

5.3 Model Development for Pitting Rates and Penetration Depths Over Time

The variety of shapes, depths and surface openings characterizing pits are essentially infinite, and attempting to account for the density of pits across a given surface at any given time can make the measurement of pitting events even more complex. There is an abundance of resources available that cover pitting phenomena as well as several standards providing instruction pertaining to pit measurement and characterization (ASTM G46 provides an excellent description of pitting morphologies). Those concepts will not be explored here at this time. It is not the intent here to delve into all the intricacies of pitting science, but rather to explore a simplistic approach to envision how pitting rates and penetration/recession depths that might vary under certain circumstances, should pitting corrosion occur.

While general recession/oxidation rates sometimes appeared to be higher in the pretreat environment, pitting susceptibilities seemed to be more prominent in the brine solution (again, likely due to the concentrated chloride content). It should be emphasized that under normal operating conditions, it is believed that pitting is highly improbable in either solution with any of these metal candidates, including Cronidur. The observed pitting on Cronidur samples during polarization testing occurred under aggressive and accelerated test conditions where damaging voltages were applied. While small voltages may simulate accelerated life conditions to a degree, higher voltages tend to promote side reactions, degradation effects and anomalies not associated with actual corrosion events and would not generally occur under average field conditions.

Caution must be applied when interpreting pitting and repassivation information from the upper anodic regions of cyclic polarization curves. As presented earlier (Section 4.4.2), the maximum achievable pitting recession rates can be extrapolated from the lowest possible slopes in the region following the breakdown point E_{Brk} prior the vertex (assuming the vertex is tailored into the test run appropriately). Additionally, relative time periods from E_{Brk} to the maximum pitting slope can be surmised from the scan data and are unique for each metal. In short, these extrapolated values become critical factors in simulating how pitting rates and recession depths might change or evolve over time. If pitting happens to initiate and sustained growth follows, what would the growth profile look like?

Early on, it was envisioned that pitting recession rates rise rapidly after initiation, reach a peak rate (that is, a maximum pitting rate) and then decline slowly to zero as oxide product increasingly blocks the pit entrances, while penetration/recession depths increase pseudo-parabolically over time and then level off at some maximum plateau. Hard field data has confirmed that this perception is indeed what happens. There are a number of published works over the last 40-50 years in which sample weight losses and penetration depths were physically measured at regular time intervals over several years in various environments. In particular, field data presented in a couple of interesting studies examining low alloy steels, stainless steels and an Inconel alloy were utilized for the work efforts in the current project[13,14]. These results have revealed some very compelling curve forms or profiles describing the evolution of recession depths and rates over longer time periods which are believed to be characteristic of essentially all metals.

It is now established that changes in penetration depths p over time t closely follow a modified exponential or Weibull-type function which starts out at zero and increases to an asymptotic plateau as the maximum penetration depth is achieved and pitting ceases . . .

$$p_{Pit} = p_{\infty} - a_1 \exp\left(-b_1 t^{c_1}\right)$$

where p_{∞} becomes the theoretical maximum pit depth attainable and a_1, b_1 and c_1 are constants that control the shape of the profile. The time derivative of this function gives the penetration rate over time k_{Pit} which ascends to a maximum rate under activation control and then decreases to zero under diffusion control. It has been found to closely correspond to a Hoerl power function . . .

$$\frac{dp}{dt} = k_{Pit} \cong a_2 b_2^t t^{c_2}$$

where a_2, b_2 and c_2 are profile shaping constants.

Model profiles describing penetration depths and rates were established for each of the six metals in both test solutions utilizing the maximum pitting rate estimates and E_{Brk} times obtained from the polarization scans. In addition, average pitting shapes were based on conic-type volumes (for simplicity) which penetrate about 5 times deeper than general recession. These results are considered only to represent possible depths and rates in an unlikely worst-case scenario in which the repassivation protection mechanism for each metal is overcome, inhibited or otherwise ignored. Graphical results for two of the subject metals are given in Figure 31 as examples of the technique applied to all candidates.

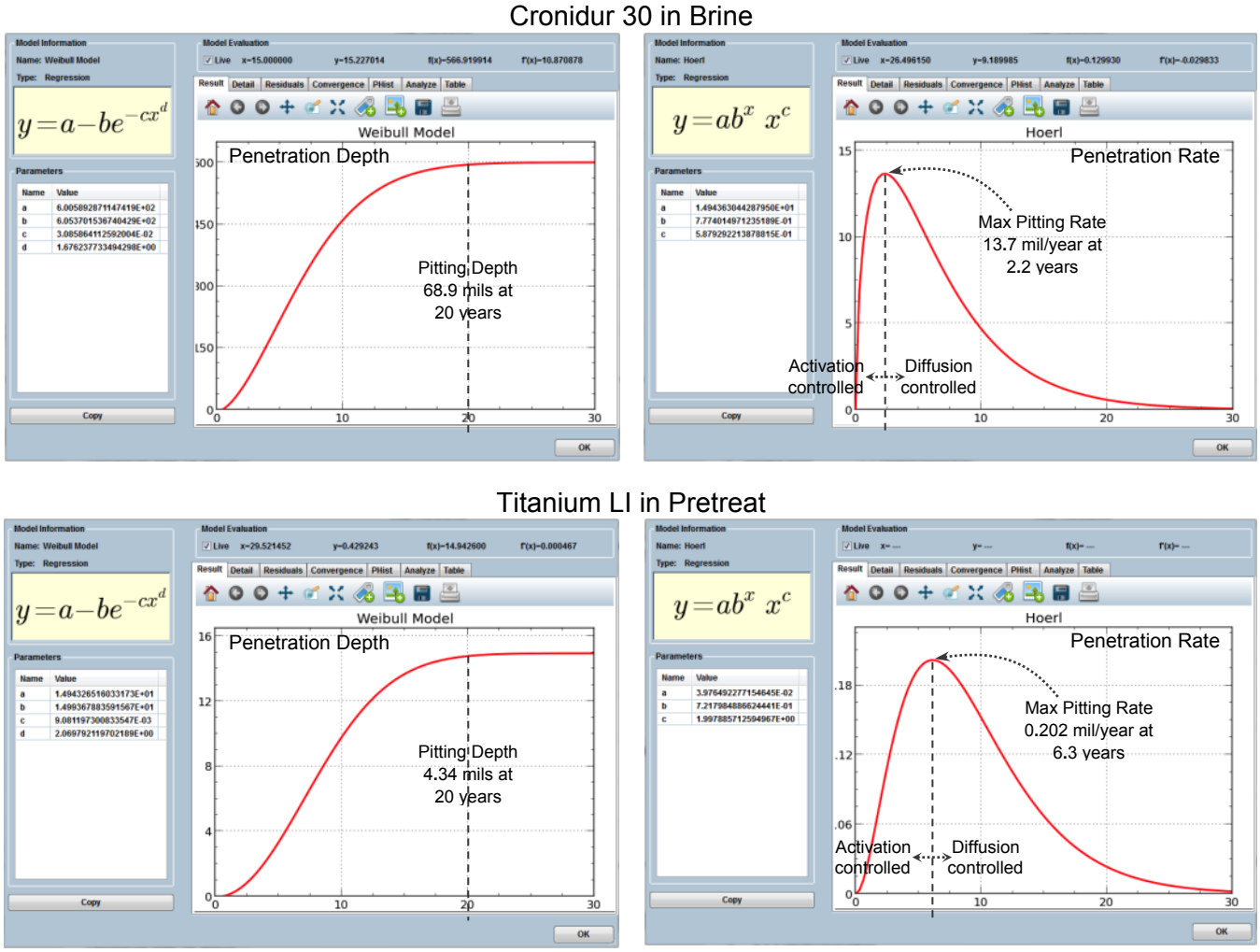

Figure 31: Example of modelled pitting penetration depths and rates for Cronidur 30 and Titanium LI.

Maximum penetration rates and the corresponding time periods estimated for the six test metals in Pretreat media were (1) Titanium CP: 0.181 mpy at 5.4 years, (2) Titanium LI: 0.202 mpy at 6.3 years, (3) Titanium 6-4: 0.268 mpy at 7.2 yrs, (4) Inconel 625: 2.47 mpy at 3.2 yrs, (5) Hastelloy C276: 2.08 mpy at 3,2 yrs, (6) Cronidur 30: 6.0 mpy at 2,5 yrs, and in Brine media, (1) Titanium CP: 0.326 mpy at 6.0 yrs, (2) Titanium LI: 0.296 mpy at 6.7 yrs, (3) Titanium 6-4: 0.332 mpy at 6.8 yrs, (4) Inconel 625: 3.19 mpy at 3.2 yrs, (5) Hastelloy C276: 3.67 mpy at 3.1 yrs, and (6) Cronidur 30: 13.7 mpy at 2.2 yrs (where mpy = mil/year). As expected, the Titanium metals exhibit the lowest maximum rates and the longest time periods to reach that rate than any of the other metals.

It has already been demonstrated that neither general corrosion nor pitting corrosion takes place on any of the subject test metals in either solution after continuous exposure under normal/ambient conditions after at least one year of storage. For several of the Cronidur samples, cyclic polarization indicated that, under overly-aggressive testing conditions, pitting could potentially initiate and sustain (at least for a while) but these results are not necessarily realistic. Nevertheless, tabulated results for the

six metals in both solutions in a notional worst-case situation where the effects of repassivation recovery are ignored are given in Table 13 primarily for the purpose of academic inquisitiveness.

Table 13: Modelled pitting recession depths and rates under hypothetical worst-case scenarios.

	Cummulative Pitting Penetration Depths (mil)							Incremental Pitting Penetration Rates (mil/year)						
Pretreat	1 yr	3 yrs	6 yrs	9 yrs	12 yrs	16 yrs	20 yrs	1 yr	3 yrs	6 yrs	9 yrs	12 yrs	16 yrs	20 yrs
Titanium CP	0.03	0.58	3.80	7.52	9.7	11.1	11.7	0.03	0.13	0.18	0.14	0.08	0.04	0.01
Titanium 6-4 LI	0.03	0.60	3.06	8.75	11.6	13.6	14.8	0.03	0.13	0.20	0.17	0.11	0.05	0.02
Titanium 6Al-4V	0.06	0.90	4.16	12.30	16.9	21.0	23.9	0.06	0.19	0.27	0.25	0.19	0.12	0.07
Inconel 625	1.70	13.8	43.2	73.2	87.6	95.1	98.5	1.70	2.48	1.82	1.02	0.52	0.19	0.07
Hastelloy C-276	1.35	11.5	38.3	64.1	76.5	82.8	85.6	1.35	2.08	1.56	0.88	0.44	0.16	0.06
Cronidur 30	4.48	34.0	110	190	233	260	274	4.48	5.99	4.58	2.84	1.62	0.71	0.30
Brine														
Titanium CP	0.08	1.17	5.91	15.52	20.9	25.5	28.8	0.08	0.25	0.33	0.29	0.22	0.13	0.07
Titanium 6-4 LI	0.12	1.29	5.76	14.24	18.9	23.0	26.1	0.12	0.26	0.30	0.26	0.19	0.12	0.07
Titanium 6Al-4V	0.05	0.89	5.37	15.34	21.4	26.8	30.8	0.05	0.20	0.32	0.32	0.25	0.16	0.09
Inconel 625	2.01	17.5	68.3	108	127	136	140	2.01	3.19	2.40	1.35	0.67	0.24	0.08
Hastelloy C-276	2.17	19.8	79.2	127	151	163	168	2.17	3.67	2.88	1.65	0.84	0.31	0.10
Cronidur 30	11.6	109	270	431	515	566	594	11.6	13.4	9.46	5.64	3.14	1.36	0.57

Hypothetical worst-case scenario in which normal repassivation protection is inhibited

As the results indicate, there is a stark contrast between the hypothetical penetration depths and pitting rates of the Titanium metals and the two nickel alloys, and the potential weaknesses of Cronidur are apparent. Factors that could theoretically contribute to inhibition of the strong repassivation forces present on these metals or perhaps alter the repassivation process might include special chemical agents that were somehow introduced into the media, particularly those high in fluoride content and/or very strong erosion currents which were aggressive enough to dislodge the growth of oxide lattice planes as they formed. In the rare event that sustained pitting growth continued to progress into one of the subject metals, tools such as this could possibly provide some insight regarding long term corrosive effects under extreme or abnormal conditions. More importantly, this model can be modified to include varying levels of repassivation contributions to counter the raw pitting rates and possibly tailored for specific situations of interest. At present however, such an approach is still in its infancy.

5.4 Special Method for Estimating Corrosion Susceptibilities

The concepts of susceptibility defined for this study are rudimentary and should be considered as extensions to the topics covered in ASTM G102. They are purely creations of the author which seemed to work well for the current study. No guarantee is given regarding their validity, correctness or accuracy in any other application. Since these are evolving concepts at this point, it is perhaps best to consider all susceptibility definitions as 'relative' to the group of metals under evaluation for this study.

Before the porous layer precipitates, the electrical double layer (EDL), which forms along the solution-oxide surface, contributes the majority of the capacitance exhibited by the combined surface layers. As the porous layer develops and widens, contributions from the EDL capacitance decrease, but when positive voltage is applied, the EDL charges up as the capacitance increases. Now the barrier oxide layer itself also produces a small capacitance due to the separation of charges at the barrier-porous interface and charges along the metal surface (or within the conversion zone) with the barrier oxide acting as the dielectric. Generally, the oxides studied here are all ceramic dielectric insulators, but most of them exhibit point defects characteristic of *n*-type semiconductivity where cation interstitials (Cr_i^{3+}, Ti_i^{4+} and Fe_i^{3+}) and oxygen vacancies ($V_O^{\bullet\bullet}$) become the primary charge carriers leading to metal ion ejection into the solution as hydrolytic dissolution takes place. When the applied voltage exceeds a threshold voltage, which is generally prior to the breakdown potential E_{Brk}, the behavior transitions over to *p*-type conductivity. Beyond E_{Brk}, conduction may occur by tunneling or avalanche effects (nickel oxide NiO itself is a *p*-type conductor throughout and will be addressed later).

During open circuit exposures and external polarization fields, the dielectric barrier layer evolves in thickness along with corresponding changes in barrier layer capacitance $C = q/E_{App} = \varepsilon_0\varepsilon_r A/t$, surface charge density, $\sigma = q/A = \varepsilon_0\varepsilon_r E_{App}/t$ and electric field strength, $\mathcal{E}_{Pol} = \sigma/\varepsilon$ (in accordance with Gauss' law). Here, q is the charge transferred from the base metal to the oxide to the solution, E_{App} is the applied test voltage (the potential difference across the oxide), A is the sample test area (fixed at 1 cm^2 throughout), t is the barrier layer thickness, ε_0 is the vacuum permittivity constant and ε_r is the relative permittivity of the oxide (that is, ε_r is the dielectric constant of the oxide while $\varepsilon_0\varepsilon_r = \varepsilon$ is the absolute permittivity).

Now recognize that $\mathcal{E}_{Pol} = \sigma/\varepsilon = CE_{App}/A\varepsilon$, or $E_{Pol}\varepsilon = CE_{App}t/A$, from which a representative breakdown indicator specific to that oxide layer can be envisioned. The product $E_{Brk} \bullet \varepsilon_r$ carries a special significance indicating the tendency of the oxide to resist the breakdown forces and protect itself by virtue of its inherent properties. The value of the breakdown potential E_{Brk} provides information regarding the propensity of the oxide to fail with subsequent pitting into the base metal, while ε is a relative indicator of the oxide's dielectric capability. If both of these factors are high, there is a very low probability that the oxide will succumb to the breakdown forces. One factor can compensate for the other. If one is high and the other low, the oxide can still be protected. But if both factors are low, the susceptibility is high and breakdown is imminent. To be more proper, consider the height of E_{Brk} above another potential of interest, say the primary passivation potential, that is . . . $(E_{Brk} - E_{Pas})\varepsilon_r$. This is reasonable since the greater the voltage difference between E_{Brk} and E_{Pas}, the lower the propensity that breakdown will occur. Conversely, an argument can be made regarding the repassivation potential, since the higher and closer it is to E_{Brk}, or rather the smaller the difference between E_{Brk} and E_{ReP}, the higher the chance that repassivation will protect the recovering metal surface, that is . . . $(E_{Brk} - E_{ReP})/\varepsilon_r$. These insights are consistent with real world perceptions and are in accordance with recognized interpretations of cyclic polarization curves.

In a more comprehensive and decorous approach it is proposed that the relative susceptibilities for the initiation (nucleation) and sustainment (unabated growth) of pitting can be represented respectively by the following arguments . . .

$$\left(E_{Brk}-E_{Pas}\right)\varepsilon_r \qquad \text{and} \qquad \left(E_{Brk}-E_{ReP}\right)\varepsilon_r^{-1}$$

Formal definitions can then be proposed for the relative susceptibilities to Pitting Initiation S_{PiI} and Pitting Sustainment S_{PiS} in exponential form, respectively . . .

$$S_{PiI}=1-exp\left[\left(\left(E_{Brk}-E_{Pas}\right)\varepsilon_r\right)^{-1}\right] \qquad \text{and} \qquad S_{PiS}=1-exp\left[\left(\left(E_{Brk}-E_{ReP}\right)\varepsilon_r^{-1}\right)^{1}\right]$$

Thus, when S_{PiI} is low, E_{Brk} and E_{Pas} are far apart, and when S_{PiS} is low, E_{Brk} and E_{ReP} are close together. Likewise, the higher the relative permittivity constant for a given oxide ε_r, the lower the susceptibility. Figure 32 shows example susceptibility plots for three of the subject test metals which indicates the stark differences between these metals in terms of pitting initiation. Delta potentials for Cronidur in pretreat solution ranged from about 0.5 to 1V while those of Inconel ranged from about 0.7 to 1.1V and for Titanium CP, 1.4 – 1.7V. These potential ranges are numerically descriptive of the estimated susceptibilities for each of the metals and are emphasized in Figure 32. As one might expect, the Titanium metals possess strong protection mechanisms across the board, especially in the measured test range, while Cronidur appears to exhibit an elevated level of susceptibility towards pitting, and the Inconel samples indicate susceptibilities that are in between but closer to Cronidur. These results were also reflected in Table 10 (Section 4.4.4).

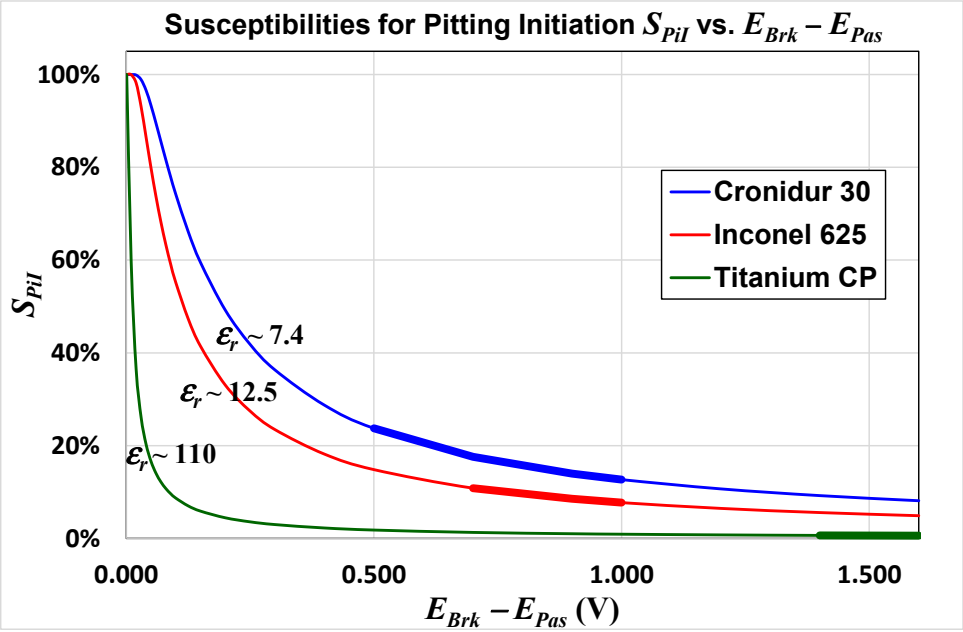

Figure 32: Pitting initiation plots for three of the test metals in pretreat showing the respective active areas.

For further analysis, consider two contrasting cases taken from typical Titanium and Cronidur cyclic runs depicted in Figures 33 and 34 which illustrate how passivation, breakdown and repassivation events might be associated with the concept of susceptibility.

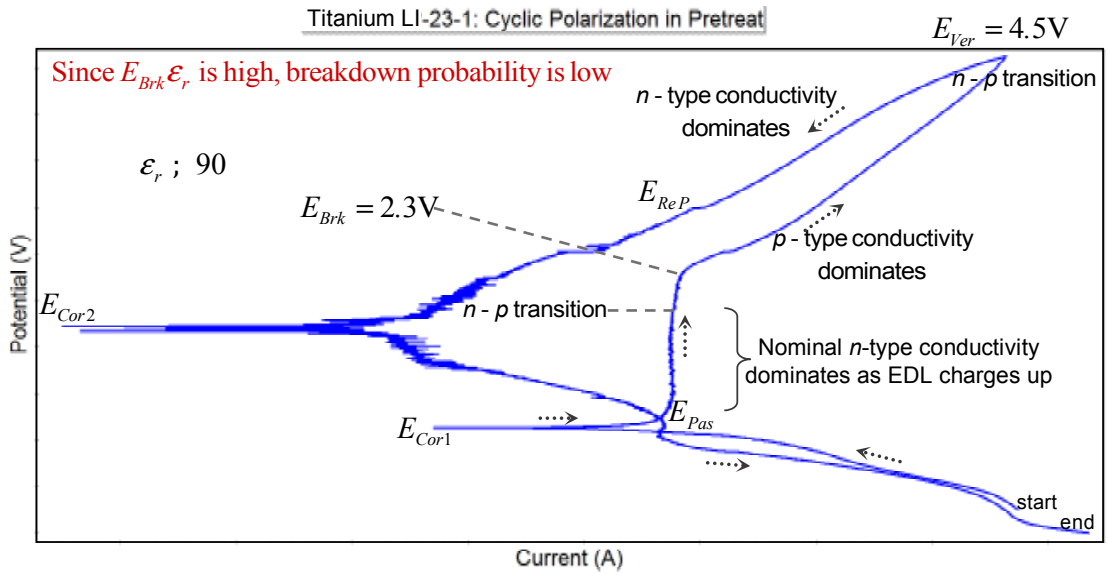

Figure 33: Cyclic plot for Titanium LI showing possible relationships between conductivity and susceptibility.

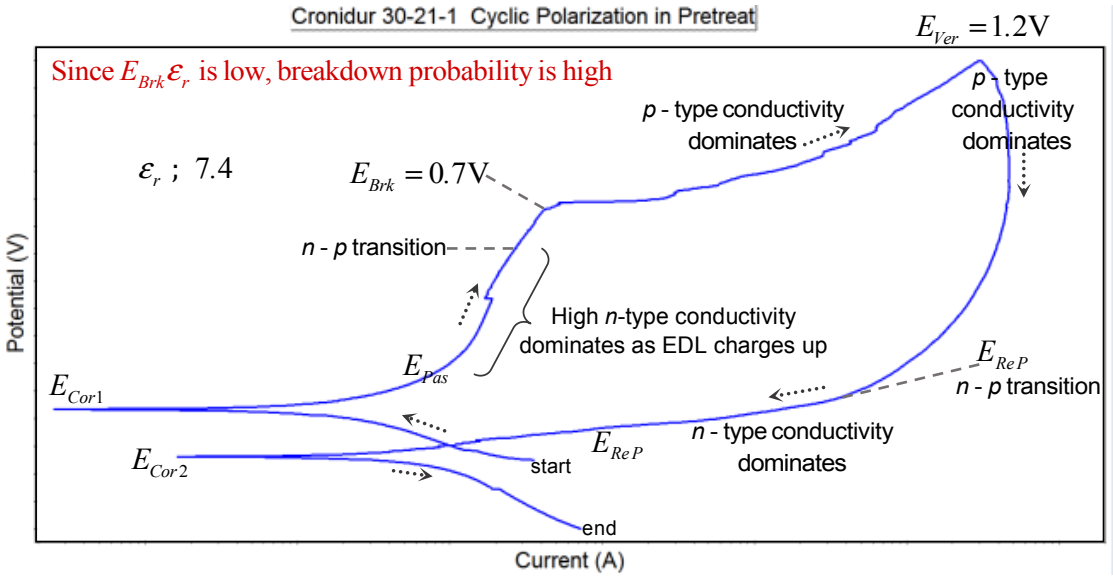

Figure 34: Cyclic plot for Cronidur 30 showing possible relationships between conductivity and susceptibility.

After the potential switches polarity (from cathodic to anodic) at E_{Cor1}, the oxide layer rapidly develops. When most of the growth is complete at E_{Pas}, the curve passes into the passive plateau where *n*-type conductivity accommodates the charge accumulation along the EDL. At the threshold voltage, conductivity switches from *n*-type to *p*-type as metal cations are ejected into the solution and cation vacancies become the major charge carriers. After E_{Ver}, oxide regeneration is accompanied by restoration of *n*-type conduction. The greater the regions of *n*-type behavior during anodic charging, the lower the corresponding S_{PiI} value, and the smaller the *n*-type range during anodic discharging following E_{ver} but prior to E_{Cor2}, the lower the S_{PiS} value.

The method outlined at the beginning of this section for estimating S_{PiI} and S_{PiS} can be extended to provide similar representations for general corrosion susceptibility pertaining to E_{Cor} by making use of certain thermodynamic equivalences. Utilizing the standard Gibbs free energy change of formation ΔG_f^0 for each component, complex averages were developed for each of the composite oxides comprising the special materials property database formulated for this study (Section 5.2). With this approach, the relative susceptibility for general corrosion during open circuit potential (OCP) measurements and Linear polarization analysis can be estimated . . .

$$S_{Cor} = 1 - exp\left[\left(\left(E_{Cor} - E_f^0\right)\varepsilon_r\right)^{-1}\right]$$

where E_f^0 is the corresponding potential change associated with the free energy change of formation ΔG_f^0 which follows from the Nernst equation, that is . . . $G_f^0 = -nFE_f^0$.

Values for S_{Cor} were provided in Tables 8 and 9 when the data for OCP and Linear/Tafel analysis was presented. During analysis of the galvanic couple configurations (Table 11), differences between the couple potential E_{OCG} and original open circuit potential E_{OCI} were computed utilizing the factor $(E_{OCG} - E_{OCI})\varepsilon_r$. Overall, while these susceptibility concepts may seem simplistic, they appear to have work quite well for this study, providing good representations of the relative corrosive tendencies for each test metal as they combine inherent material properties with actual test data. For informational purposes, average developmental values for the dielectric constants and formation potentials associated with each of the composite oxides examined in this study are given in Table 14.

Table 14: Average representative values utilized for ε_r and ΔE_f^0 during estimation of relative susceptibilities.

	Inconel 625	Hastelloy C276	Titanium CP	Titanium 64	Titanium LI	Cronidur 30
ε_r	12.46	11.43	110.0	90.22	90.40	7.38
ΔE_f^0	-2.68 V	-2.35 V	-2.91 V	-3.17 V	-3.18 V	-2.89 V

5.5 Passive Films as Pseudo-Capacitors and Semiconductors

Several models have been developed to describe the oxide growth process on passive metals including the High Field Model[15], the Place Exchange Model[16] and the Point Defect Model[17,18]. Of these, the Point Defect Model (PDM) developed by D.D Macdonald has been reported to account for all the experimental observations regarding the structure and behavior of passive films. The methodologies and calculations involved in the PDM are intensive, and it is beyond the scope of this paper to present all the associated concepts here. However, for qualitative purposes, it would be interesting to explore some of the possible reactions responsible for conduction across the oxide layer as well as growth and dissolution of the layer itself. A representative scenario is illustrated in Figure 35 utilizing chromium as an example and making use of Kröger-Vink notation.

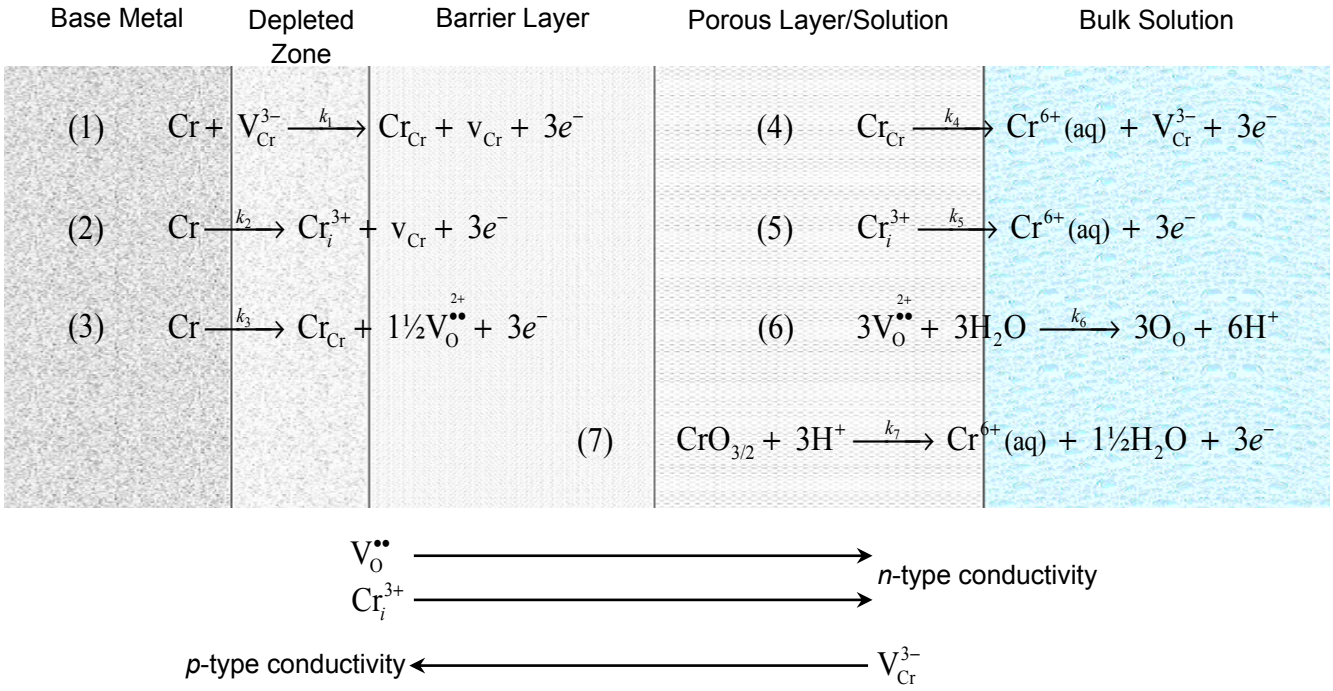

Figure 35: Possible reactions for a chromium substrate leading to conduction, oxide production and dissolution. Cr = metal atom in base metal, V_{Cr}^{3-} = cation vacancy in oxide lattice, Cr_{Cr} = metal cation at cation site in oxide lattice, v_{Cr} = vacancy in base metal, Cr_i^{3+} = interstitial cation in oxide lattice, $V_O^{\bullet\bullet}$ = oxygen vacancy in oxide lattice, Cr^{6+} (aq) = fully oxidized metal cation in solution, O_O = oxygen anion in oxygen lattice, and $CrO_{3/2}$ = ½ Cr_2O_3 = Cr_{Cr} + 1½ $V_O^{\bullet\bullet}$.

The theory is based on the activity of Schottky point defects associated with *n*-type conductivity as described by reactions (2) and (5), and reactions (3) and (6), and Frenkel point defects associated with *p*-type conductivity as described by reactions (1) and (4). Furthermore, transmission of ions through the barrier layer are proposed to occur exclusively by the motions or fluxes of vacancies and interstitials which are created at one interface (the metal-oxide interface or the oxide solution interface) and are annihilated or depleted at the opposite interface. The nonconservative reactions (3) and (5) lead to growth and dissolution of oxide respectively and are responsible for movement of the oxide boundaries. At steady state, certain reactions are in equilibrium, that is, $k_1 = k_4$, $k_2 = k_5$ and $k_3 = k_6 = k_7$.

The barrier layers on Cronidur, Titanium and its alloys are known to exhibit *n*-type conductivity at lower potentials and then transition to *p*-type at some point just prior to E_{Brk}. This implies that conduction across these oxides is accomplished by the movement of oxygen vacancies $V_O^{\bullet\bullet}$ (or holes) and cation interstitials Cr_i^{3+}, both of which become electron donors that are annihilated (or depleted) at the solution interface. However, in the nickel-based alloys Inconel 625 and Hastelloy C276, the nickel oxide (NiO) component behaves as a *p*-type conductor throughout and is characterized by the movement of cation vacancies V_{Ni}^{2-} which become electron acceptors that would be depleted at the metal interface. If phase separation happens to occur between the Cr_2O_3 and NiO fractions, a *p*-*n* heterojunction is established along their common interface. This phenomena is explored further in the next section.

5.6 Anomalies on Nickel Alloys under Extreme Test Conditions

As mentioned earlier, some of the Inconel and Hastelloy samples exhibited unusual effects during abnormal cyclic polarization in pretreat media when starting voltages were significantly cathodic. Some of the test samples were pre-conditioned at negative potentials during the beginning of the cyclic scan in order to test the extremes and to explore the possible ramifications. Figure 36 reproduces the condition portrayed in Figure 28(a) for one of the Hastelloy samples which was conditioned at –0.75V for five minutes at the beginning of the cyclic polarization scan. Observational notations are also given.

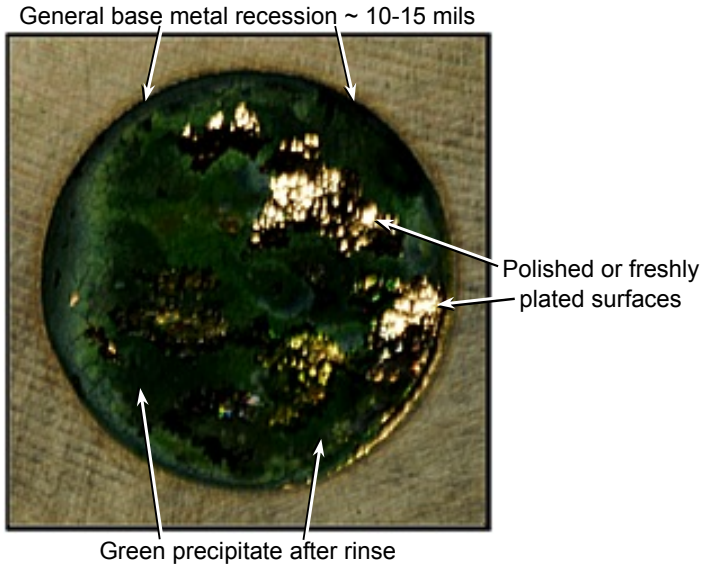

Figure 36: Hastelloy sample surface after cyclic polarization scan in pretreat with –0.75V cathodic conditioning.

It should be realized that these types of results were obtained only during exposures in the pretreat solution and not in the brine concentrate. This could be related to the lower level of associated ion pairs in the fresh acid solution along with a condition of high activation-controlled access to the metal surface as compared to the viscous brine media in which chemical reactivity may be limited by concentration diffusional effects. Testing showed that cathodic stripping can begin at potentials as high as –0.2V. Likely causes for the green precipitate will be addressed first.

At the end of the polarization scan, the concentration of dissolved nickel ions near the sample surface is very high. The reason for this will be explained later. When the sample was quickly removed from the solution and gently rinsed in pH 7 water, regions of green precipitate remained. It was shown that continued rinsing and/or more aggressive rinsing would wash away these precipitated remnants. It is believed that the green precipitates are comprised of nickel hydroxide $Ni(OH)_2$, nickel oxyhydroxide NiOOH and complexed nickel hydroxide/hydrates derived from the semi-organic test solution. While $Ni(OH)_2$ crystals are generally light-to-pale green in form, the organic complexes in this precipitate are believed to be responsible for the rich green appearance. Factors leading to recession of the base metal and the polished or metallization effect require a more intensive analysis.

In short, it is surmised that following cathodic stripping of the air-formed passive layer, anodic regeneration of the new passive layer facilitated migration, concentration and/or separation of the nickel oxide (NiO) phase toward the periphery of the layer, placing it in direct contact with the solution. The NiO outer layer acted as a barrier to inward oxygen flow and begin to trap electrons within the Cr_2O_3 core which underwent reduction (cathodic weakening of the crystal structure) until the outer NiO barrier layer failed at or after E_{Brk}. This condition exposed the unprotected base metal to the acid solution at high anodic voltage inducing rapid etching into the metal. Metallization effects could have been facilitated by the high concentration of Ni^{2+} ions local to the surface following the voltage reversal at E_{Ver}, and/or electrolytic polishing effects could have taken place during the repassivation process following E_{ReP}.

There are standard industry practices for stripping the passive layers from metal surfaces which can be performed under cathodic voltages or in acid solutions or both. Mixtures of phosphoric and chromic acid have been used for this purpose (same acids in the pretreat solution). Thus, it is reasonable to understand how cathodic conditioning at the beginning of a polarization scan can result in stripping of the passive layer. If left under cathodic control in an acid solution for too long, etching of the base metal will commence. In weak chromic/phosphoric etching solutions at ~ −0.75 to −1V, the oxide layer may be completely stripped away in a matter of seconds or minutes. After the passive layer anodically re-forms and throughout the passive plateau, electrolytic polishing of the oxide surface takes place. Again, such concepts are common practice in the metal finishing industry.

Unfortunately, chemical analysis of the samples and Electrochemical Impedance Spectroscopy (EIS) were not conducted during these studies due to scheduling and cost constraints. Surface compositional analysis may have provided information regarding the nature and possible factors leading to formation of the observed products, while Mott-Schottky capacitance-potential plots obtained via EIS would have facilitated estimations of the respective charge carrier concentrations during the voltage sweep. Thus, the mechanisms proposed in the descriptions and explanations given in the following paragraphs are primarily hypothetical at this time.

A number of researchers have confirmed the formation of *p*-*n* type barrier bilayers under anodic conditions on nickel-rich alloys consisting of chromium oxide Cr_2O_3 cores underneath nickel oxide NiO outer layers[19,20,21]. Furthermore, it has been historically recognized that NiO films act as diffusion barriers, effectively preventing the inflow of reactive species. More recently, it has been demonstrated that that NiO layers completely block the electrochemical reactions and the transmission of charge carriers in the depletion region[22]. These findings help to corroborate the proposed theory.

In general, the subject metals with their passive layers are analogous to pseudo-*n*-type Schottky diodes or barriers in which the oxides act as lightly doped *n*-type semiconductors due to the intrinsic impurities present from natural contaminates when the layer initially develops. Under steady state conditions, no current is drawn (the diffusion current and drift current are equal and opposite) but a small voltage drop is established across the metal-oxide junction, the so-called 'built-in' voltage V_{bi}. This is analogous to the larger galvanic potential difference exhibited between dissimilar metals which are in contact and is proportional to the difference between their work functions. The built-in voltage that electron energies must surpass in order to flow corresponds to the Schottky energy barrier height qV_{bi}. For a metal-*n*-type interface or junction, the depletion region occurs only in the oxide phase which creates a space charge electric field where charges q can be stored and hence, a small level of pseudo-capacitance exists. When the passivated metal is placed in an electrolyte, an electrical double layer (EDL) forms and the capacitive space charge widens along with the depletion region (see Section 4.2).

In a typical potentiodynamic scan, current is always flowing into the sample while electrons are always flowing outward. When the immersed sample is first subjected to a negative cathodic voltage, an excess of electrons flows outward weakening and disintegrating the initial passive oxide layer in the process as it dissolves in the acidic solution. Again, if held too long in this region, general etching of the base metal will occur. As the potential is increased toward E_{Cor}, the number of excess electrons diminishes and finally goes to zero at E_{Cor}. When the applied potential begins to increase above E_{Cor} into the anodic region, valence electrons are then extracted from the metal while the oxide starts to re-form on the surface. As the anodic (positive) voltage continues to increase, the new oxide layer grows under a 'reverse bias' condition through E_{Pas} and into the passive region.

A reverse bias is imposed on the metal-*n*-type junction since the energy barrier for current flow through the oxide layer is increased and the potential across the junction increases. Under this condition, the depletion region expands and the diffusion of electrons attempting to cross the junction is greatly reduced. As long as the applied reverse voltage is in effect and continuing to increase, the total potential across the junction continues to increase above the built-in voltage while the electric field also increases. A small reverse saturation current is maintained during this segment of the process (for a while). The almost constant reverse current is sustained across the passive plateau as a nominal diffusion of charge carriers continues until the E_{Brk} region is approached. This is representative of the Titanium example given in Figure 37 which depicts four possible responses during anodic polarization. With the Cronidur example in Figure 37, the diffusion current overwhelms the reverse current. For nonpassivating metals, there is no resistance to electron flow and the process is activation-controlled with ideal Tafel behavior. The nickel fraction in the passive layer of alloys such as Inconel and Hastelloy can produce some interesting effects not seen with the other metals.

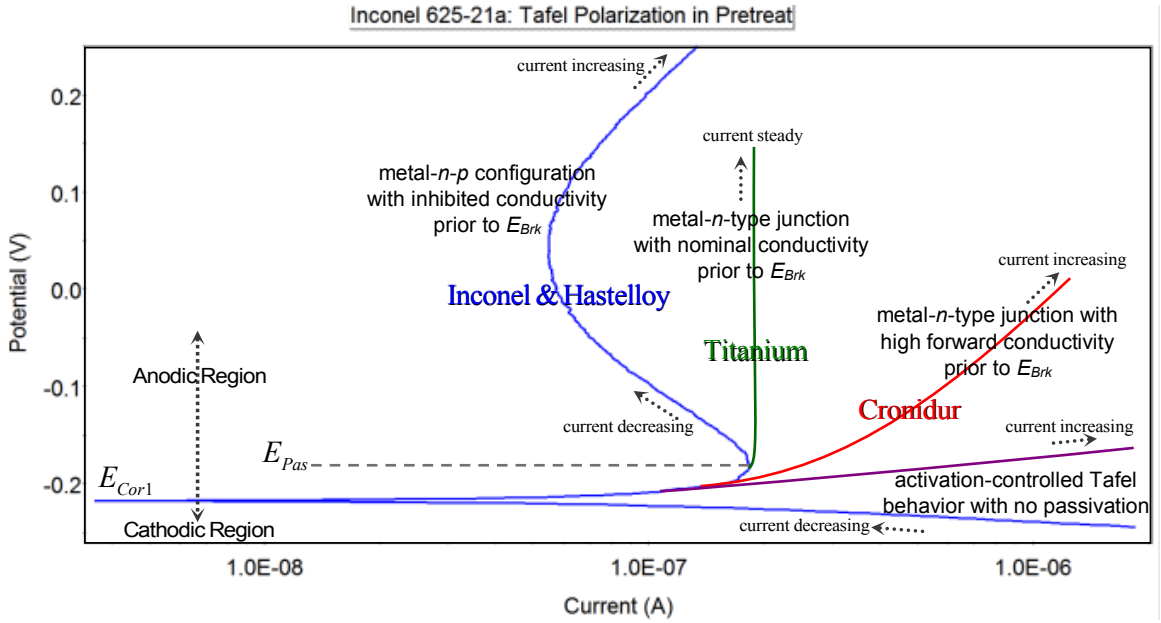

Figure 37: Illustration of possible polarization paths during and after primary passivation.

A couple of points should be emphasized here. The arrows indicate the direction of the scan. However, changes in the value of the current at any given time are not reflective of the direction that the current is flowing. As stated earlier, throughout all these polarization scans, current is always flowing into the sample while electrons are always flowing outward. This is due to the fact that the applied voltage drop across the cell is always forcing electrons to flow out of the sample. In cathodic regions (prior to E_{Cor1} and after E_{Cor2}), excess conduction electrons are flowing outward while during the anodic segments (after E_{Cor1} and prior to E_{Cor2}), valence electrons flow outward. For corroding metals, the current is generally increasing throughout the passive zone (however, forward current does not necessarily mean that corrosion is taking place). A steady current after E_{Pas} implies that the oxide layer is a tenacious semiconductor with a high E_{Brk} while an increasing current could infer a lower E_{Brk}. In single metal scans, particularly for rate estimation purposes, current values are always treated as positive quantities. Outside of the ±50mV linear range, the slope of the scan may be an indicator of whether the current is increasing or decreasing. On log plots, whenever the current is directed away from E_{Cor1}, it is increasing and whenever the current is directed toward E_{Cor1}, it is decreasing.

The polarization behaviors depicted in Figure 37 for Titanium and Cronidur are well substantiated and are classical curve forms for these types of metals. However, due to the high nickel content in Inconel and Hastelloy, electrochemical activity throughout the passivation region is quite different. The 'bowing' feature shown in this plot seems to be characteristic of high nickel alloys as it reflects the opposite changes in current that occur after E_{Pas}. The degree of curvature has been seen to vary during different test runs with the largest exaggerations resulting with samples which were cathodically conditioned. While the other metals are known to exhibit single metal-*n*-type Schottky junctions, the nickel alloys are believed to possess a multi-layer or multi-junction film which possesses the characteristics of a bipolar metal-*n*-*p*-type barrier configuration. This feature is believed to be directly associated with the extent of phase separation that occurs within the Cr_2O_3-NiO bilayer.

While Cr_2O_3-NiO bilayers likely form to some degree in almost all electrochemical situations, the effects of cathodic conditioning appear to exacerbate the phase separation process as indicated throughout this work. Under ambient conditions, undoped NiO is more of an insulator than it is a semiconductor with a resistivity on the order of 10^{-13} Ω-cm and very few charge carriers. These properties are key in determining the extent that NiO will behave as a diffusion barrier. Consider the activities illustrated in Figure 38 as a high content Ni-Cr metal undergoes anodic passivation under reverse bias conditions.

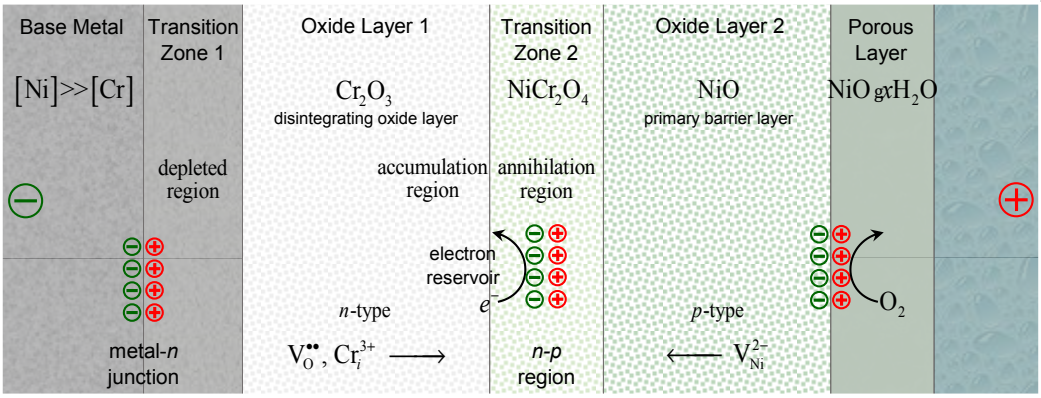

Figure 38: Illustration of possible processes during anodic passivation of Ni-Cr alloys under reverse bias.

The Ni-Cr substrate is a highly conductive metal that provides a Schottky-type ohmic contact to the *n*-type Cr_2O_3 oxide region (which includes Transition Zone 1 for the most part). However, the applied negative potential to metal side causes an increase in the energy barrier against electron flow through the metal-*n*-type junction into the Cr_2O_3 layer. This leads to the accumulation of electrons on the other side of the Cr_2O_3 layer. Transition Zone 1 is the gradient transition region between metal and oxide (see Section 4.1). Electrons are also depleted in this zone so, creation of the primary charge carriers is restricted. As iterated in Section 5.5, the majority carriers in the *n*-region are electron donors which have been identified as oxygen vacancies $V_O^{\bullet\bullet}$ and interstitial chromium cations Cr_i^{3+} that flow toward Transition Zone 2. This zone is first created by reactions between Cr_2O_3 and NiO during the initial passivation process and is shrinking as the NiO outer layer increases in thickness.

In the *p*-type NiO phase, the majority carriers are nickel cation vacancies which flow toward Transition Zone 2 from the other direction. Collisions between opposing charger carriers creates an annihilation region which prevents the flow of electrons into the NiO phase. Thus, inbound current and outbound electron flow are essentially cut off, similar to a *p*-*n*-*p* bipolar transistor in 'cut-off' mode where very little current flows. Since the number of donors and acceptors in both regions is severely limited, annihilation activity is minimal while an excess of electrons become trapped within the Cr_2O_3 layer. In essence, the external NiO layer acts as a barrier, limiting the diffusion of oxygen from the outside and trapping the outflow of electrons from the inside. This condition creates an electron-rich reduction environment within the Cr_2O_3 region that cathodically destabilizes the oxide structure with increasing detrimental effects as the applied voltage continues to increase (analogous to cathodic disintegration). To provide section-to-section clarity, Figure 39 gives the cyclic polarization semi-log scan for the sample depicted in Figure 36.

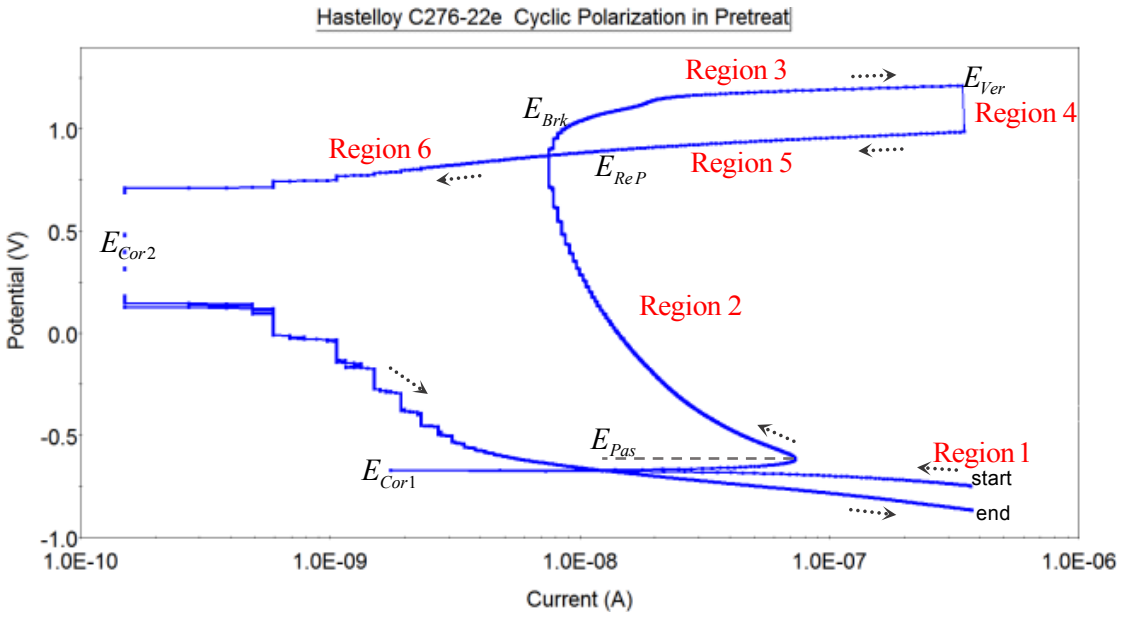

Figure 39: Cyclic polarization scan for the anomalous Hastelloy sample shown in Figure 36.

As iterated earlier, current is always flowing inward while electrons are always flowing outward. The arrows map the scan direction but they may also indicate the relative increases and decreases in electron flow. When polarization starts in the cathodic region, the sample is a positively charged cathode that is becoming less cathodic as the potential increases and approaches E_{Cor1}. At E_{Cor1}, the sample reverses polarity and becomes a negatively charged anode. For metals containing semiconductive passive layers, this corresponds to an applied reverse bias on the sample throughout the anodic branch. Forward bias occurs during the cathodic branches (prior to E_{Cor1} and after E_{Cor2}) where reductive cathodic dissolution of the oxide layer is possible.

Region 1 in Figure 39 marks the beginning of this test at −0.75V just after constant cathodic conditioning was applied for five minutes. The applied potential (vs. Ag/AgCl) is negative in this region. It is suspected that most, if not all, of the original air-formed oxide layer was removed before the forward scan begin. At the start, there was an abundance of free electrons (excess conduction electrons) supplied by the power source. As the potential is increased, these electrons are ejected while E_{Cor1} is approached (current is decreasing as indicated). At E_{Cor1}, the sample polarity reverses and becomes positive while all the excess electrons are depleted. As E_{Cor1} is surpassed, the current begins to increase while anodic oxidation (passivation) of the metal surface commences and valence electrons begin to flow outward. The specific value of E_{Cor} attained is unique to the metal and its interaction with the particular solution. Between E_{Cor1} and E_{Pas} (E_{Pas} represents the maximum passivation current), the Cr_2O_3 layer begins to form almost immediately followed by formation of the $NiCr_2O_4$ and NiO layers. Under increasing reverse bias conditions, the actual time lapse between development of the Cr-rich sublayer and the Ni-rich outer layer is greatly reduced. By the time E_{Pas} is reached, a heavy Ni-rich layer has developed in the outer regions of the passive layer.

In Region 2, just beyond E_{Brk}, the current decreases as the applied voltage continues to increase up to the threshold potential just prior to E_{Brk}. This indicates that the outflow of electrons has become blocked by the outer NiO barrier. Additionally, the NiO layer inhibits the inflow of oxygen from the outside which reduces the passivation reactions at the metal substrate and essentially 'cuts off' the growth of protective Cr_2O_3. This imposes strong reduction forces on the existing Cr_2O_3 layer as the outer NiO layer then becomes the primary protection barrier. The NiO layer is essentially acting as a MOS capacitor. Accumulation of electrons in the Cr_2O_3 layer leads to a condition where the Cr_2O_3 structure becomes cathodically weakened. Mobile chromium particles and oxygen may be produced in this space prior to E_{Brk} . . . $Cr_2O_3 \longrightarrow Cr^0 + 1½O_2\uparrow$, and outgassing may increase the pressure inside the volume beneath the NiO layer. For this particular run, the intersecting scan lines happen to correspond roughly to both the threshold potential and the repassivation potential E_{ReP}.

The indicated breakdown potential probably pertains to or is dominated by the NiO phase. At E_{Brk} , an abrupt increase in the current occurs as electrons begin tunneling through the layer followed by avalanche outflow. At the beginning of Region 3 (i.e… at E_{Brk}), anodic disintegration of NiO commences and nickel cations are ejected into the solution, $Ni_{Ni} \longrightarrow Ni^{2+}(aq) + V_{Ni}^{2+} + 2e^-$, as the NiO layer begins to break apart and dissolve in the acid, $NiO + 2H^+ \longrightarrow Ni^{2+}(aq) + H_2O$. Since the Cr_2O_3 layer is depleted when the NiO layer ruptures and dissolves, the base metal is instantly exposed to the highly anodic acid solution. Throughout Region 3 (E_{Brk} to E_{Ver}), rapid and aggressive etching of the base metal takes place which temporarily overwhelms the metal's repassivation protection mechanism, $Ni^0 + 2H^+ \longrightarrow Ni^{2+}(aq) + H_2\uparrow$ and $Cr^0 + 6H^+ \longrightarrow Cr^{6+}(aq) + 3H_2\uparrow$. Etching ceases at E_{Ver} (the relief point) where the increasing voltage ramp reverses and begins to decrease.

The short vertical segment depicted by Region 4 reflects a small time period, just before repassivation begins, when the current change is almost nil. Due to the heavy concentration of Ni^{2+} ions in close proximity to the surface, it is possible a small degree of metallization or back-plating occurred. Once repassivation initiates, this very thin, shiny Ni deposit would be stabilized. Regions 5 and 6 represent the reactions associated with repassivation and oxide regeneration on the Ni-Cr surface. Recall that E_{ReP} is the point where the repassivation rate rapidly starts tapering off. It is usually not visible on the log plot but is quite pronounce on the normal plot. It has been observed with these metals that after the voltage ramp reverses, repassivation is usually swift and powerful. Along Region 5, new oxide is rapidly being deposited, and following E_{ReP}, electrolytic polishing of the oxide surface may take place which could also impart a shiny appearance as seen in the photo. Positively charged Nickel complexes and hydrates saturate the adjacent solution within the Nernst layer. They are attracted to and neutralized along the negative oxide surface. At E_{Cor2}, these products become loosely bound. Beyond E_{Cor2}, the damaged sample area is completely covered with new oxide and green Nickel precipitates as it becomes increasingly cathodic until the scan reaches the endpoint and the polarity starts drifting back toward OCP. While there is no solid corroborating evidence to support this scenario at this time, it does explain the observed phenomena to a reasonable degree.

References

1. ASTM G78-01(2012), Standard Guide for Crevice Corrosion Testing of Iron-Base and Nickel-Base Stainless Alloys in Seawater and Other Chloride-Containing Aqueous Environments, ASTM International, West Conshohocken, PA, 2012, www.astm.org.

2. Lawrence J. Foreman, EM Materials Lab - ECLSS Pretreat Testing Cost & Schedule Estimate, Version 2-0, 30 January 2013, EM60 Project Engineering Branch.

3. ASTM G59-97(2014), Standard Test Method for Conducting Potentiodynamic Polarization Resistance Measurements, ASTM International, West Conshohocken, PA, 2014, www.astm.org.

4. ASTM G71-81(2014), Standard Guide for Conducting and Evaluating Galvanic Corrosion Tests in Electrolytes, ASTM International, West Conshohocken, PA, 2014, www.astm.org.

5. ASTM G100-89(2010)e1, Standard Test Method for Conducting Cyclic Galvanostaircase Polarization, ASTM International, West Conshohocken, PA, 2010, www.astm.org.

6. ASTM G102-89(2010), Standard Practice for Calculation of Corrosion Rates and Related Information from Electrochemical Measurements, ASTM International, West Conshohocken, PA, 2010, www.astm.org.

7. W. Stephen Tait, An Introduction to Electrochemical Corrosion Testing for Practicing Engineers and Scientists, Pair O Docs Publications, Racine WI, ISBN 0-9660207-0-7, 1994.

8. M. Stern and A.L. Geary, Electrochemical Polarization, I. A Theoretical Analysis of the Shape of Polarization Curves, Journal of the Electrochemical Society, pp. 56-63, January 1957.

9. Milton Stern, A Method for Determining Corrosion Rates from Linear Polarization Data, National Association of Corrosion Engineers, Vol. 14, pp. 59-64, 1958.

10. A. J. Bard and L. R. Faulkner, Electrochemical Methods, p. 103, John Wiley & Sons, NY, 1980.

11. Passivation Oxide Controlled Selective Carbon Nanotube Growth on Metal Substrates, J B Bult, W G Sawyer, P M Ajayan and L S Schadler, Nanotechnology 20 (2009) 085302.

12. XPS Analysis of the Passivation Layer on Stainless Steel, Innovatech Labs, Plymouth, MN.

13. James F. Jenkins, Corrosion Behavior of BY-80 Steel, Type 304 Stainless Steel and Inconel 600 Alloy at 213-E-12B Burial Ground, Hanford, WA, Naval Facilities Engineering Service Canter, Port Hueneme, CA, August thru October 1993.
14. J.S. Lee, R.I. Ray and B.J. Little, Lifetime Predictions for Carbon Steel in Natural Fresh Water, Naval Research Laboratory, Oceanography Division, Stennis Space Center, MS, 3/8/2011.

15. L. Young, Anodic Oxide Films, Academic Press, New York, 1961.

16. B. E. Conway, H. Angerstein-Kozlowska, and W. B. A. Sharp, J. Electroanal. Chem., 43, 9, 1973.

17. Digby. D. Macdonald, The Point Defect Model for the Passive State, J. Electrochem. Soc., 139, 12, 1992.

18. JianEr Bao and Digby D. Macdonald, Growth Kinetics of the Anodic Oxide Film on Platinum under Potentiodynamic Polarization Conditions, Z. Phys. Chem., 227, 541-559, 2013.

19. P. Combrade et al, Oxidation of Ni-Based Alloys in PWR Water: Oxide Layers and Associated Damage to the Base Metal, Proceedings of the 12th International Conference on Environmental Degradation of Materials in Nuclear Power System Water Reactors, The Minerals, Metals & Materials Society, 2005.

20. Diego E. Pissinis et al, Utilization of Special Potential Scan Programs for Cyclic Voltammetric Development of Different Nickel Oxide-Hydroxide Species on Ni-Based Electrodes, Open Journal of Physical Chemistry, 2, 23-33, 2012.

21. Dangguo LI et al, Chemical Composition and Mott-Schottky Analysis of Passive Film Formed on G3 Ally in Bicarbonate/Carbonate Buffer Solution, Acta. Metall. Sin. (Engl. Lett.), Vol. 23, No. 6, pp 461-472, December 2010.

22. Xuan-Hao Chana, James Robert Jennings et al, Characteristics of p-NiO Thin Films Prepared by Spray Pyrolysis and Their Application in CdS-sensitized Photocathodes, J. Electrochem. Soc., Vol. 158, Issue 7, H733-H740, 2011.

REPORT DOCUMENTATION PAGE

Form Approved
OMB No. 0704-0188

1. REPORT DATE *(DD-MM-YYYY)*	2. REPORT TYPE	3. DATES COVERED *(From - To)*
01–04–2015	Contractor Report	

4. TITLE AND SUBTITLE

ECLSS Sustaining Metal Materials Compatibility Final Report, Electrochemical and Crevice Corrosion Test Results

5a. CONTRACT NUMBER
NNM12AA41C

5b. GRANT NUMBER

5c. PROGRAM ELEMENT NUMBER

6. AUTHOR(S)

R.E. Lee

5d. PROJECT NUMBER

5e. TASK NUMBER

5f. WORK UNIT NUMBER

7. PERFORMING ORGANIZATION NAME(S) AND ADDRESS(ES)

Jacobs ESSSA Group
Huntsville, AL 35806

8. PERFORMING ORGANIZATION REPORT NUMBER
M–1397

9. SPONSORING/MONITORING AGENCY NAME(S) AND ADDRESS(ES)

George C. Marshall Space Flight Center
Huntsville, AL 35812

10. SPONSORING/MONITOR'S ACRONYM(S)

11. SPONSORING/MONITORING REPORT NUMBER
NASA/CR—2015–218208

12. DISTRIBUTION/AVAILABILITY STATEMENT

Unclassified-Unlimited
Subject Category 25
Availability: NASA STI Information Desk (757–864–9658)

13. SUPPLEMENTARY NOTES

Prepared for the Materials and Processes Laboratory, Engineering Directorate
Technical Monitor: C.K. Russell

14. ABSTRACT

Electrochemical test results are presented for six noble metals evaluated in two acidic test solutions which are representative of waste liquids processed in the Environmental Control and Life Support System (ECLSS) aboard the International Space Station (ISS). The two test solutions consisted of fresh waste liquid which had been modified with a proposed or alternate pretreatment formulation and its associated brine concentrate. The six test metals included three titanium grades, (Commercially Pure, 6Al-4V alloy and 6Al-4V Low Interstitial alloy), two nickel-chromium alloys (Inconel® 625 and Hastelloy® C276), and one high tier stainless steel (Cronidur® 30).

15. SUBJECT TERMS

corrosion, pitting, passivation, polarization, passive oxide, oxide growth rate, corrosion rates, corrosion susceptibility, repassivation, open circuit potential, linear polarization, Tafel polarization

16. SECURITY CLASSIFICATION OF:			17. LIMITATION OF ABSTRACT	18. NUMBER OF PAGES	19a. NAME OF RESPONSIBLE PERSON
a. REPORT	b. ABSTRACT	c. THIS PAGE			STI Help Desk at email: help@sti.nasa.gov
U	U	U	UU	94	19b. TELEPHONE NUMBER *(Include area code)* STI Help Desk at: 757–864–9658

National Aeronautics and
Space Administration
IS20
George C. Marshall Space Flight Center
Huntsville, Alabama 35812